Thermal Protection System Analysis and Sizing for Spaceplane Configurations

Preliminary design of the TPS and optimization of the insulation layer

Evelyne Roorda

TU Delft

1

[1] Cover image from http://www.cbsnews.com/pictures/space-plane-of-tomorrow/8/, visited on 20/06/2017

Thermal Protection System

Analysis and Sizing for Spaceplane Configurations

Preliminary design of the TPS and optimization of the insulation layer

by

Evelyne Roorda

to obtain the degree of Master of Science
at the Delft University of Technology,
to be defended publicly on Monday July 17, 2017 at 14:00 AM.

Student number:	4044398	
Project duration:	June 1, 2016 – July 17, 2017	
Thesis committee:	Dr. ir. E. Mooij,	TU Delft, supervisor
	Ir. A. Kopp,	DLR, supervisor
	Prof. Dr. P. Visser,	TU Delft
	Dr. Ir. D.I. Gransden,	TU Delft
	Ir. K.J. Sudmeijer,	TU Delft

TU Delft

Preface

I would like to take this opportunity to thank my two supervisors, Erwin Mooij and Alexander Kopp. Erwin thank you for your understanding and patience during my thesis, and your useful (though sometimes frustrating) input and comments. Alexander, I would also like to thank you for your patience, as well as your willingness to always help me think about the problems I encountered and your useful suggestions.

Furthermore I would like to sincerely thank all who have taken the time to given me their expert opinions and help during my thesis, especially Dominic Dirkx, Kees Sudmeijer, Javad Fatemi and Martin Lemmen.

My friends and fellow students have helped keep me sane throughout my study and the thesis process. Thanks for giving me the confidence and courage to keep going. I would specifically like to thank the students of the 9^{th} floor student room for their company and support. Especially Tim, you let me ramble on about my problems and gave me advice that let me in the right direction. And of course Hanneke, for being my friend throughout my entire studies and always helping me out. My friends of JC Babylon have been one of the great things I have gained from my student life in Delft. Kirsten and Nina, I look forward to concurring parts of South-America with you.

Lastly I would like to thank my parents and sister. Thank you for your encouragements and understanding. Vati, you have been an inspiration for me throughout my studies. Without your support, financially but mostly mentally, I would not be where I am today. Mutti thank you for always being there for me, to talk to or if I just wanted to come home and be taken care of for a few days.

After almost eight years I have come to the end of my studies. It has not been an easy journey for me, and I am proud to have pulled through and make it to the end. The result of my hard work, sweat, and tears is this report. I can only hope that the effort that has gone into it shines through.

Evelyne Roorda
Delft, July 2017

Abstract

During its lifetime a space launcher is subjected to extreme heat loads. These can dramatically influence the design of the launcher, when parts of the vehicle heat up to very high temperatures. Every part of the vehicle has a temperature range in which it is functional, thus it is important that these limits are respected. Therefore, space vehicles are equipped with a Thermal Protection System (TPS). A properly designed TPS is vital to every reusable launcher vehicle, as an under-designed system will lead to mission failure, and an over-designed system to an increase in mass, resulting in an increase in cost. Heat loads are typically the largest during the ascent or decent phase, where the spacecraft flies through the atmosphere. The large velocities combined with the atmosphere causes atmospheric drag, which results in aerodynamic heating. In this thesis the design of a TPS is considered, focused on spaceplane vehicles. The accompanying research question is: how robust is a thermal protection system design for a spaceplane wing-body configuration to variations with respect to the design parameters or trajectory taking into account heat transfer through radiation and conduction in three dimensions?

To answer the research question a tool was developed which is capable of designing a TPS and optimizing the insulation layer thickness. Furthermore, a trajectory simulation was made for the reentry phase. For rocket powered launchers the largest heat loads typically occur during reentry, as in this mission phase the longest time is spent in the atmosphere. From the trajectory specifics the heat flux over the vehicle over time could be generated, which is the source of the temperature increase. In the TPS design tool the first major task is to divide the vehicle into different TPS areas, based on the temperatures that are experienced at each of these areas of the skin surface. Five different TPS areas will be defined, all assigned a passive TPS type. The TPS types are FRSI, AFRSI, TABI, AETB TUFI and CMC. A thermal analysis is performed, taking into account both conduction in three dimensions and radiation to outer space as well as to the inner subsystems of the vehicle. From this analysis the maximum experienced temperature can be deduced for each area. When the TPS design is found, it is aimed to optimize the insulation layer thicknesses in all TPS areas. The goal is to find a design that is as light as possible, thus with a minimum insulation layer thickness, while still meeting the given constraints. These constraints are the maximum reusable temperatures of the TPS types, and the limit functional temperature of the underlying structure. The structure is made of aluminum, and has a maximum functional temperature of 450 K. The maximum temperatures of the TPS types are 644 K, 922 K, 1400 K, 1600 K, and 1850 K respectively. The TPS design tool was applied to a reference vehicle. A sensitivity study was performed to investigate the robustness of the TPS design resulting from the tool. The performance of the TPS design was tested when small changes were made to it, for the nominal reentry trajectory of the reference vehicle. Furthermore the TPS designs performance was analyzed for small changes in the trajectory.

From the analysis of the results of the developed tool it was found that a TPS design can be developed for a simple wing-body configuration, under the specified conditions. However, the functionality of the TPS design is limited. Improvements must be made to the developed tool to increase its performance, so that it can come to an acceptable TPS design. It is suspected that with suggested improvements the tool will work properly, and a well functioning TPS design can be made. However, further research is required to ensure this.

Abbreviations

1D	one dimensional
2D	two dimensional
3D	three dimensional
AETB	Alumina Enhanced Thermal Barrier
AFRSI	Advanced Flexible Reusable Surface Insulation
c.o.g.	center of gravity
c.o.m.	center of mass
C/SiC	Carbon Fibre reinforced Silicon Carbide
CFRP	Carbon Fiber Reinforced Polymer
CMC	Ceramic Matrix Composite
DLR	German Aerospace Center
ECEF	Earth-Centered, Earth-Fixed
ECI	Earth-Centered Inertial
EoM	Equations of Motion
ESA	European Space Agency
FEI	Flexible External Insulation
FEM	Finite Element Model
FESTIP	Future European Space Transportation Investigations Program
FRSI	Flexible Reusable Surface Insulation
HOTOL	HOrizontal TakeOff and Landing
HOTSOSE	Hot Second Order Shock Expansion
LEO	Low Earth Orbit
MLI	Multilayer Insulation
NASP	National AeroSpace Plane
ODE	ordinary differential equation
RK4	fourth-order Runge-Kutta
RKF45	Runge-Kutta-Fehlberg
RLV	Reusable Launch Vehicle
SART	Space Launcher Systems Analysis
SOH	Suborbital Hopper
SPFI	Surface Protected Flexible Insulation

SSTO	Single-Stage-To-Orbit
TABI	Tailorable Advanced Blanket Insulation
TBD	To Be Determined
TOP2	Thermal protection system Optimization Program Version 2
TPS	Thermal Protection System
TSTO	Two-Stage-To-Orbit
TUDAT	TU Delft Astodynamics Toolbox
TUFI	Toughened Uni-Piece Fibrous Insulation
US	United States
US76	US Standard Atmosphere 1976
USSR	Soviet Union
VD	Voronoi Diagram

Nomenclature

Greek Symbols

Symbol	Description		Units
α	angle of attack		rad
α_T	thermal expansion		K^{-1}
χ	heading angle		rad
δ	latitude		rad
ϵ	emissivity		-
ϵ	error		-
ϵ^*	desired accuracy		-
ϵ_T	strain		-
γ	Flight path angle		rad
γ	ratio of specific heats		-
μ	gravitational Parameter		m^3/s
ϕ	Euler angle		rad
ϕ	golden ratio		-
ρ	density		kg/m^3
ρ_0	density at sea level		kg/m^3
σ	stress		N/m^2
σ_B	Boltzmann's constant	$5.667 \cdot 10^{-8}$	W/m^2K^4
τ	longitude		rad

Roman Symbols

Symbol	Description	Units
A	transfer area	m^2
a	speed of sound	m/s
A_e	exit area	m^2
C_D	aerodynamic drag coefficient	-
C_L	aerodynamic lift coefficient	-
C_m	aerodynamic pitch moment coefficient	-
C_p	specific heat at constant pressure	J/K
C_S	aerodynamic side coefficient	-

C_v	specific heat at constant volume		J/K
C_{m_b}	aerodynamic pitch moment coefficient body flap		-
D	aerodynamic drag force		N
E	modulus of elasticity		N/m^2
F	geometric form factor		-
$\mathbf{F}$	force vector		N
F_A	aerodynamic reference frame		
F_B	body-fixed reference frame		
F_I	inertial planetocentric reference frame		
F_R	rotating planetocentric reference frame		
F_V	vertical reference frame		
G	universal gravity constant		$m^3kg^{-1}s^{-2}$
g	gravitational acceleration		m/s^2
g_0	gravitational acceleration at sea level		m/s^2
h	(geopotential) altitude		m
h_c	convective heat transer coefficient		-
$\mathbf{K}$	conductance matrix		
k_c	thermal conductivity		W/mK
L	aerodynamic lift force		N
L_0	original length		m
M	Mach number		-
M	molecular mass		kg/mole
m	mass		kg
$\dot{m}_0$	free stream mass flow rate		kg/s
$\dot{m}_e$	exhaust mass flow rate		kg/s
M_0	mean molecular mass at sea level		kg/mole
N	total number density		m^{-3}
N_A	Avogadro's constant	$6.0225 \cdot 10^{26}$	$kmol^-1$
p	pressure		N/m^2
p_0	free stream pressure		N/m^2
p_e	exhaust pressure		N/m^2
$\tilde{q}$	dynamic pressure		N/m^2
q_c	heat flux rate		$W/m^2/s$
R	gas constant for air		$Jmole^{-1}K^{-1}$

R^*	universal gas constant	$\mathrm{Jmole^{-1}K^{-1}}$
R_E	Earth equatorial radius	m
R_N	nose radius	m
S_{ref}	aerodynamic reference area	$\mathrm{m^2}$
T	temperature	K
t	time	s
$\mathbb{T}$	transformation matrix	
t_2	second value thickness range	m
t_3	third value thickness range	m
T_M	molecular temperature	K
$T_{lim_{struc}}$	limit reusable temperature of the structure	K
$T_{lim_{Tm}}$	safety margin	K
$T_{lim_{TPS}}$	limit reusable temperature of the TPS	K
$T_{max_{struc}}$	maximum experienced temperature by the structure	K
$T_{max_{TPS}}$	maximum experienced temperature by the TPS	K
t_{max}	upper boundary thickness range	m
t_{min}	lower boundary thickness range	m
t_{opt}	optimal thickness	m
U	gravitational potential	$\mathrm{m^2/s^{-2}}$
V	Volume	$\mathrm{m^3}$
v	Velocity	m/s
V_0	exhaust velocity	m/s
V_0	free stream velocity	m/s
V_c	circular velocity	m/s

Superscripts

Symbol	Description	Units
$\ddot{\square}$	Second derivative w.r.t. time	
$\dot{\square}$	First derivative w.r.t. time	

Subscripts

Symbol	Description	Units
0	Initial value	
x, y, z	Component along direction	

Contents

1 Introduction

An introduction to the thesis work and the report will be given in this Chapter. Starting with the background of the thesis subject in Section 1.1. Section 1.2 continues with a description of the thesis aims. The outline of the report is described in Section 1.3.

1.1. Background

Since living history outer space has been a fascination to the human race. In the last centuries dreams of visiting this unknown territory came into play, initially just as fiction, but in the second half of the 20^{th} century developments in space launch technologies began occuring swiftly. Especially the 'Space Race' between the United States (US) and Soviet Union (USSR) facilitated the amount of resources being put into space missions[1]. In the Space Race the two nations competed, among other things, to launch the first artificial satellites and to put the first human being on the Moon. The USSR won the first competition in 1957, by launching the Sputnik in a Low Earth Orbit (LEO), making it the first artificial Earth satellite. After the USSR also was the first to perform human spaceflight in 1961, the US won the final round in 1969 by placing the first man on the Moon with the Apollo 11 mission. From here on the trend was set to raise the bar on the possibilities of space missions.

A major constraint on space missions is the large heat load that the vehicle must endure, which are typically largest during the descent or ascent phase of the flight. The large velocities that are reached result in high drag values when there is an atmosphere present, such as in flights to and from Earth. The longer the vehicle is subjected to atmospheric drag, the larger the heat loads become. For rocket propelled launchers the descent trajectory typically results in the largest temperatures over the vehicle, as a relatively long time is spent in the atmosphere [31]. To ensure the spacecraft's functionality it must be protected from the heat loads it is subjected to by a so-called Thermal Protection System (TPS). A properly designed TPS is vital to any Reusable Launch Vehicle (RLV), as an under-designed system will lead to mission failure, and an over-designed system to an increase in mass, which will increase the cost and question the feasibility of the mission. Mass is always a critical factor in space missions, because every extra gram that has to be accelerated into orbit will lead to a significant increase in cost. Therefore, it is always desired to design a spacecraft as light as possible, within the predefined mission requirements and boundary conditions.

A good example of the importance of a well-designed and functioning TPS system can be found in the 28^{th} mission of the Columbia Space Shuttle on February 1, 2003 [15]. An accident occurred during launch when a piece of foam broke off from the Shuttle's external tank and damaged the TPS tiles of the vehicle wing. The minor damage to the vehicle was not fatal at that moment, and the crew was able to perform the experiments in space as they had planned. However, upon reentry the damage revealed to be catastrophic, as atmospheric gasses were entering the Shuttle, leading to loss of actuators and finally to the disintegration of the Columbia vehicle and loss of life of the entire crew.

Another important parameter in space-launchers are the amount of stages being used. Until the present

[1] http://history.nasa.gov/sputnik/, visited on 18/05/2016

day a minimum of two stages Two-Stage-To-Orbit (TSTO) is present on all successful launchers. However, for a long time the possibility of a Single-Stage-To-Orbit (SSTO) launcher has been researched. No such SSTO project has been successful yet, as the combination of the high mass of the vehicle that has to be accelerated into orbit and the available propulsion systems have proved to be a bottleneck. More and more light-weight materials are being developed, though, as are more powerful engines. Thus it seems feasible that in the near future the first SSTO vehicle could fly into space. However, for such an SSTO mission the design and especially mass of the TPS will be unrelentingly connected to its success.

1.2. Thesis Aims

In the design process of a new space mission and accompanying vehicle it is desired to get a preliminary TPS design, which forms a good estimate of a valid design. In the thesis work a reference vehicle is desired to be given a TPS, and to be studied how well this TPS performs under different circumstances. The research question of this thesis is as follows:

How robust is a thermal protection system design for a spaceplane wing-body configuration to variations with respect to the design parameters or trajectory taking into account heat transfer through radiation and conduction in three dimensions?

To answer this question it was desired to develop a tool that is able to make a TPS design with optimized insulation layer thicknesses, and submit the results of this tool to an investigation to research its sensitivity. For this process several sub-objectives were formulated:

1. Development of a trajectory simulation tool, based on a predefined angle of attack profile
2. Development of a Finite Element Model (FEM) for the reference vehicle
3. Perform a thermal analysis on the FEM based on an input heat flux, taking into account heat transfer by radiation and conduction in three directions
4. Development of a TPS design, based on a TPS database
5. Optimization of TPS insulation layer thicknesses
6. Perform a sensitivity study to research the robustness of a TPS design

In the development of the tool and throughout the work a reference vehicle was considered; the Aurora. Aurora is a concept currently in development at German Aerospace Center (DLR). Its mission is aiming to bring payload into LEO using a semi-reusable SSTO launcher vehicle. It plans to use drop tanks to carry propellant, which causes the term semi-reusable SSTO. Only one stage is used in the launcher, as no rockets are rejected. With every new launch however new drop tanks will have to be supplied for the propellant, thus it is not entirely reusable.

The heat load a space vehicle is subjected to is dependent on the trajectory that the vehicle will follow. The critical flight phase is defined in this thesis work as the flight phase during which the highest heat loads are generated. The reference vehicle that was used for the thesis work, Aurora-R, has a rocket powered propulsion system. The highest heat loads are therefore endured during the reentry phase. The reference trajectory was provided by the DLR[2]. A separate trajectory simulation was made of the reentry phase, for which the reference trajectory angle of attack over time profile was used as an input. The added value of the developed trajectory simulation lies in the possibility to analyze the trajectory and possible variations within the TU Delft, where the DLR trajectory tool used to compute the reference trajectory cannot be used. From the trajectory specifics the heat flux over the vehicles surface over time was computed using the DLR tool Hot Second Order Shock Expansion (HOTSOSE).

With the heat flux during the trajectory known a thermal analysis of the vehicle during its flight can be performed. This analysis was performed in the finite element program ANSYS. Thus it was required to generate a FEM of the reference vehicle. For both the generation of the FEM and the thermal analysis multiple options had to be considered and weighted. With this all in place the thermal analysis could be performed, in which only the heat flux from aerodynamic heating is considered as an input. Furthermore, only heat transfer by radiation and conduction in three dimensions is taken into account. The results of this thermal analysis

[2] Private communication, Alexander Kopp, DLR, 7/2/2017

include the temperature over the vehicle, over the flight time of the reentry trajectory. Based on this experienced temperature a preliminary TPS design was made for the vehicle. A database exists of multiple passive TPS types, which are applicable in a range of limit temperatures for which they are reusable. Each element of the FEM is given a TPS appropriate for the maximum experienced temperature. This TPS design is the basis of the optimization. In the optimization the thicknesses of the insulation layers are adapted until an optimum is found. It is desired to have the insulation layers as thin as possible to reduce the mass of the TPS, within their functional limits and boundary conditions. That is applied by optimizing the layers such that their TPS reusable limit temperature is not exceeded, and the temperature experienced by the structure underneath the TPS does not exceed its functional limit.

The TPS design with optimized insulation layer thicknesses is subjected to a number of tests, to research its performance when small changes are applied. These tests can grossly be divided into two sections; a first set of tests for which the nominal trajectory stays the same and changes are applied to the TPS design, and a second set of tests for which the performance of the optimized TPS design is investigated when changes in the input heat flux profile are applied. In the first set among others variations in the insulation layer thicknesses are investigated. In the second set an example is the TPS design performance when a reentry trajectory with a lower starting altitude is followed. The objective of the investigations is to find out if and where improvements can be made to the TPS design, and how sensitive the design is to small changes.

1.3. Outline Report

In this report all steps taken in the thesis process are described, with their background theory and results. In Chapter 2 general knowledge on TPSs is introduced, as well as the considerations to be made in their design. Furthermore heritage missions are described to get a feel for TPS design, and a more elaborate discussion of the reference vehicle is given. In Chapter 3 the flight dynamics that form the basis of the trajectory simulation is provided. The development of this trajectory simulation is described in Appendix C, along with the simulation outcome. The theory behind the aerothermodynamics that are responsible for the heating of the spacecraft is given in Chapter 4. In Chapter 5 the considerations made in the generation of the FEM and thermal analysis are described, as well as the results of the first performed thermal analysis in terms of the TPS area division over the vehicle. The various numerical methods that were used throughout the thesis work are discussed in Chapter 6. The optimization procedure for the insulation layer thicknesses are provided in Chapter 7, including a description of the optimized TPS design of Aurora. A sensitivity analysis for this design is performed in Chapter 8. Finally, the conclusions of the thesis work are presented in Chapter 9, and recommendations for further work are suggested.

2

Thermal Protection System Design

The TPS is an essential part of the spacecraft, as it protects the system from the extreme temperatures that it has to endure during its lifetime. Weight is a critical factor for every space mission. Therefore the TPS should be designed such that it is sufficient in protecting the vehicle from the heat loads, whiles not being over-designed and being as light as possible. To get more insight in the process of TPS design and the accompanying considerations, in this chapter first relevant heritage missions and their TPS will be discussed in Section 2.1. Second in Section 2.2 a more elaborate description of the various available TPSs is given. Third a description of the reference mission Aurora is given in Section 2.3. Here also the different requirements on the mission, and specifically on the TPS and its design process are given.

2.1. Heritage Missions

To select appropriate heritage missions a literary survey was performed for spaceplane missions with as many similarities to Aurora as possible. In that respect missions were selected that perform an SSTO flight with a horizontal take-off and landing, either rocket powered or a combination of air-breathing and rocket powered (corresponding to the Aurora-R and Aurora-AB configuration respectively). Figure 2.1 shows the difference in heating rates for both types of vehicles, for the ascent and reentry phase. The heating rate for a rocket powered mission is higher in the descent phase, whereas the ascent phase heating rate is largest for an air-breathing propulsion system. Comparing both types of propulsion, it can be seen that the air-breathing propulsion experiences a significantly larger heating rate; about 2.0 MW/m^2 for air-breathing in ascent. This can be compared to the maximum heating rate for the rocket engines in the descent phase, which is 0.82 MW/m^2. In this example a sphere with a one foot (30.48 cm) diameter is considered. Three heritage missions are selected as a reference to the Aurora mission; National AeroSpace Plane (NASP) and Skylon both use a combination propulsion, the Suborbital Hopper (SOH), resulting from the FESTIP system studies, relies solely on rocket propulsion. These vehicles are all SSTO spaceplanes like Aurora, that aim to transport to and from LEO. The transport differs from cargo to humans or both.

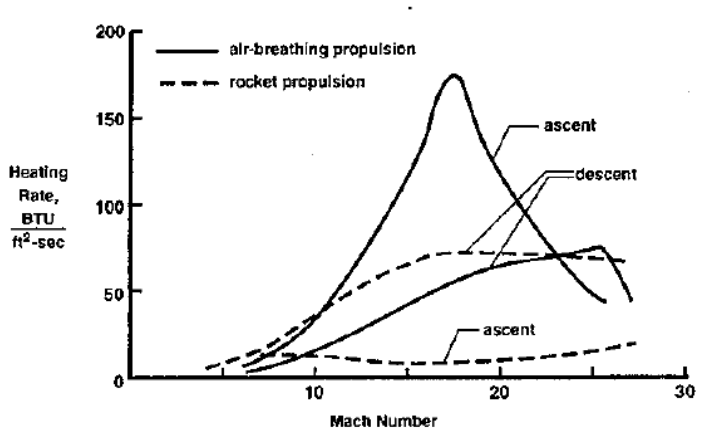

Figure 2.1: Aerothermal environment for a one-foot (30.48 cm) diameter sphere representative trajectories of space-launch vehicles [31]

National AeroSpace Plane (NASP) 1986-1994
The NASP program was intended to develop a single-stage-to-orbit (SSTO) vehicle and demonstrate its feasibility. On the long run such a reusable launcher vehicle (RLV) was meant to succeed the Space Shuttle as America's manned space launcher system. For this technology demonstration the Rockwell X-30 was developed, shown in Figure 2.2. The X-30 was planned to perform a horizontal take-off, like a regular airplane, with the use of air-breathing engines instead of rocket engines [31]. After an air-breathing acceleration of about twenty minutes the X-30 would pull up into a rocket-boosted ascent phase to orbit. An air-breathing ascent experiences larger aerothermodynamic loads compared to a rocket ascent, due to its longer presence in a high-density atmosphere with a high velocity. The program was canceled in 1994 because the challenges an SSTO manned launcher brought with it were deemed too high; the vehicle became larger and heavier as research developed, and expenses were rising far above expectations.

In the NASP studies new high-temperature, high-strength, lightweight materials were developed, such as beryllium-aluminum alloys and beta 21S titanium. Combined with the corrosion-resistant titanium-alloy-matrix composites, also developed during the NASP studies, the temperature capability of the material was increased to 1100 K. Furthermore protective coatings were developed to protect the TPS, which extended the temperature limits of the carbon/carbon TPS material to 1900 K. For the leading edges active cooling was planned, by using high-conductivity materials and heat pipe constructions [31].

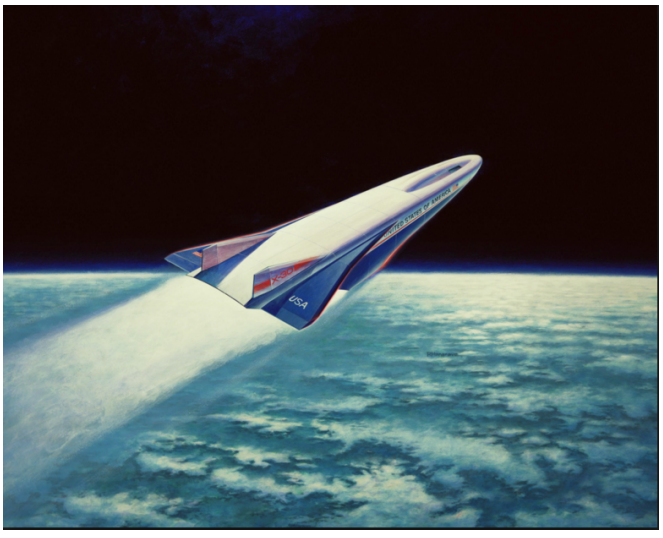

Figure 2.2: Artist impression of the NASP [1]

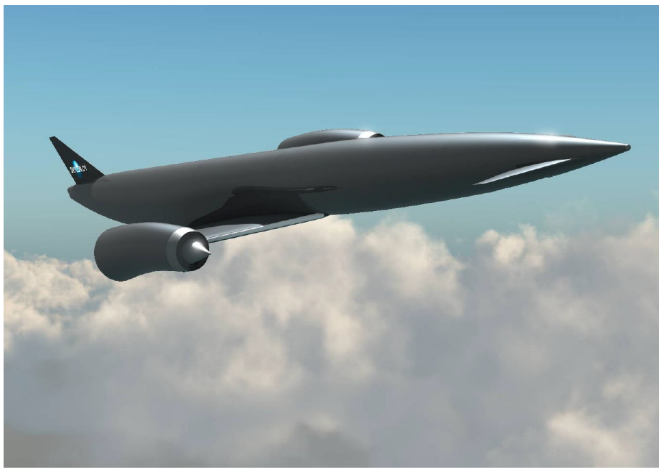

Figure 2.3: Skylon during flight, artist impression [46]

Skylon 2000-present
Skylon is an SSTO vehicle that is based on the HOrizontal TakeOff and Landing (HOTOL) concept. HOTOL is an older spaceplane concept, developed between 1982 and 1988 by Rolls-Royce and British Aerospace. Its propulsion system was to be an integrated air-breathing/rocket engine, to be developed by Rolls-Royce. The project was prematurely cancelled. Skylon is likewise a horizontal takeoff, horizontal landing spaceplane. Like HOTOL one of its most significant features is the engine, that operates in both air-breathing and rocket mode, and is being developed by Reaction Engines Limited [46]. An impression of Skylon is given in Figure 2.3. After takeoff from a runway the engine will perform as an air-breathing propulsion system up to a speed of about Mach 5.5 at an altitude of 25 km, after which it switches to rocket mode for the rest of the ascent. The vehicle consists of a slender fuselage with a delta wing, the fuselage is planned to house a payload of 12 – 15 tonnes [7]. The main objective is to lower the cost of space access routinely. Skylon is currently under development. Flight tests for the combined air-breathing/rocket engine are scheduled in 2020.

The mission profile of Skylon for the ascent phase is plotted in Figure 2.4, and for the reentry phase in Figure 2.5. In both the altitude and Mach profile over time are given. In the ascent phase the engines will first work in air-breathing mode, until a velocity of Mach 5 is reached at the altitude of 28 km. Hereafter the engines transitions to its rocket mode, and the vehicle is accelerated to orbital velocity up to an altitude of 90 km. The axial acceleration is aimed to be limited to 3g, by throttling of the engines. From the transfer orbit that is reached in the ascent phase the desired final orbit is reached by orbital maneuvering. The reentry trajectory begins at an altitude of 120 km. During reentry the endured heat loads and temperatures are aimed to be controlled by banking and angle of attack maneuvering. In the last part of the reentry a gliding approach and landing is performed.

The primary structure of the Skylon vehicle has a cover of reinforced glass ceramic sheets, which functions both as the aeroshell and main TPS, with support of a multilayer metallic heat shield (depicted in Figure 2.6). Radiative equilibrium is reached between the aeroshell and the external heat flux. During air-breathing ascent the vehicle accelerates to Mach 5 where the skin reaches temperatures up to 770 K. When the rocket ascent velocity crosses Mach 9 the flow around the vehicle becomes completely laminar, after which the temperature stays roughly constant as the density reduction is balanced by the Mach increase. The maximum skin temperature reached during ascent is 855 K. During reentry the temperature is actively kept below 1100 K by dynamic control of the trajectory. The aeroshell is designed to perform 200 missions, corresponding to a total exposure time of 100 h to high reentry temperatures. This estimation might be on the optimistic side, thus it should be expected that excessive maintenance will be required to reach the reusability of 200 missions.

[1] Image from http://nix.nasa.gov/info?id=EL-2001-00432 visited on 20/07/2016

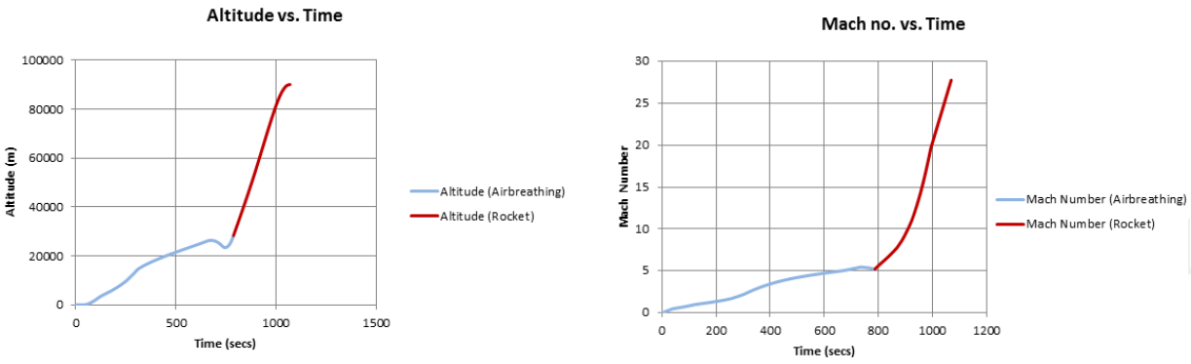

Figure 2.4: Skylon mission profile specifics for the ascent phase [23]

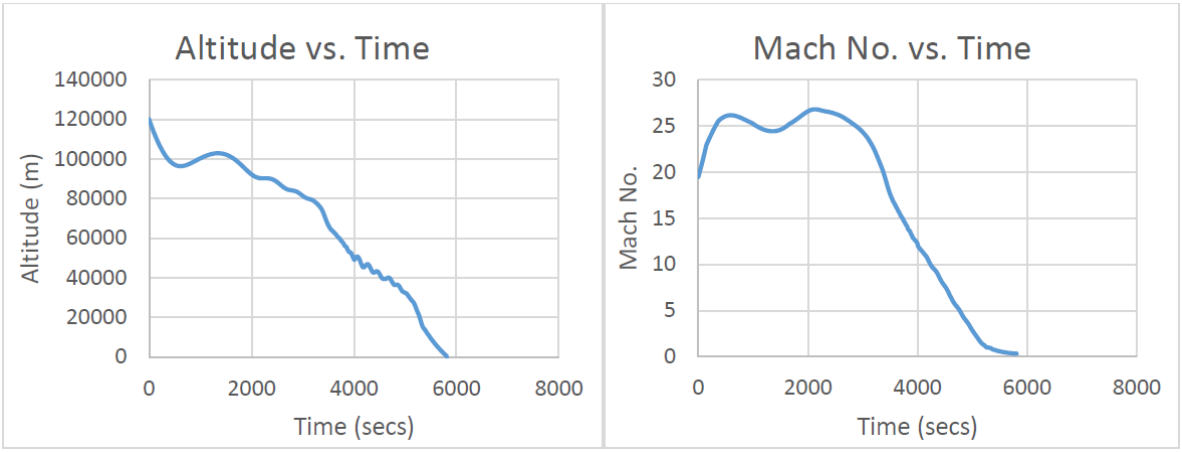

Figure 2.5: Skylon mission profile specifics for the descent phase [23]

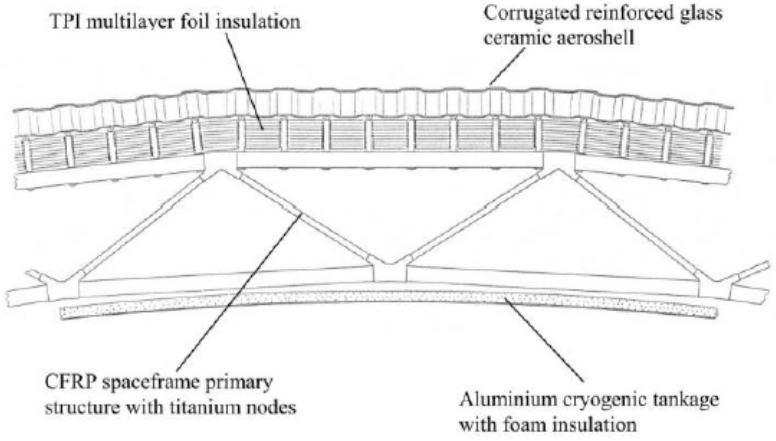

Figure 2.6: Skylon aeroshell TPS [17]

Sub Orbital Hopper (SOH) 1994-2004

The European Space Agency (ESA) started the Future European Space Transportation Investigations Program (FESTIP) system study in 1994 to investigate various concepts for reusable space transportation systems that may be feasible in the near future [26]. The study started out with many concepts, including both SSTO and TSTO systems, as well as a variety in propulsion systems including advanced rocket propulsion and combinations of rocket and air-breathing propulsion. The main criteria by which the concepts were evaluated were

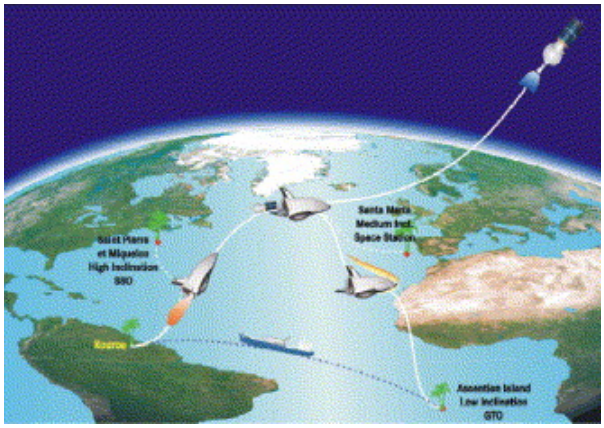

Figure 2.7: Mission profile of the SOH for three different target orbits [5]

if they would become technically feasible in the near future, if they are commercially attractive (when considering among others the costs) and which technologies are required. At the end of the study nine concepts were left, from which one was decided most preferable. This concept is the FSSC-15 SOH, a winged SSTO vehicle which performs a horizontal take-off and horizontal landing. The thrust is solely generated by rocket propulsion, and the launch is initiated by a sled. In figure 2.7 the mission profile of a mission to the geostationary transfer orbit is depicted. The flight starts with horizontal launch by a sled, from where the ascent initiates. At 100 km the engine cuts off, and the maximum altitude reached is 150 km. The cargo is ejected at 130 km. From there the SOH reenters Earth en performs a horizontal landing. The development of the SOH was canceled in 2004 after the first glide test, performed by the Phoenix one-seventh scale model of the SOH.

The SOH has different TPS areas consisting of different vehicle regions [21]. The nose, leading edges and foremost windward areas will experience the highest heat loads with temperatures up to 1500 K. Here, Carbon Fibre reinforced Silicon Carbide (C/SiC) is applied for thermal protection. On the windward areas with temperatures between 1125 and 1375 K a Surface Protected Flexible Insulation (SPFI) using a Flexible External Insulation (FEI) and Ceramic Matrix Composite (CMC) is applied. The windward areas with temperatures below 1125 K are equipped with a titanium-aluminum metallic TPS. Finally the leeward region makes use of FEI on the fuselage and wings. The estimated mass of the TPS is 11868 kg.

2.2. Thermal Protection Systems

The appropriate TPS is highly dependent on the mission at hand. The maximum heat loads endured influence the selection, as well as the maximum functional temperature of the vehicle. Other factors to be considered are the weight, costs, technology readiness, robustness, maintenance possibilities and re-usability. An overview of materials used in TPS, their application temperature and strength is displayed in Figure 2.8. It can be seen that the metallic alloys are located on the left of the graph, as they are functional for lower temperatures. The heavier alloys typically have a higher strength, such as titanium and the superalloys. Also, the materials on the left side are more oxidation stable, and thus have less need for protective coating. Oxidation is the process where a material loses electrons, leading to a change in its properties which for many metals can mean a loss in strength. Oxidation stable materials are less inclined to oxidize. Materials that perform under higher experienced temperatures are ceramics, graphites and refractory metals. It is clear that the strength of the refractory metals decays swiftly under higher temperatures. Graphite carbon-carbon can endure the highest temperatures while maintaining a relatively high strength.

One must keep in mind that the TPS of the launcher vehicle can contain a variety of materials, and possibly a combination of passive and active systems, as it can be optimized for each temperature region. To illustrate this Figure 2.9 shows the proposed TPS selection for the X-33 windward surface, consisting of a multitude of materials. The nose of the vehicle and its leading edges will typically endure the highest heat loads, thus they are composed from carbon/carbon. The elevons and bodyflaps can also be expected to heat up significantly

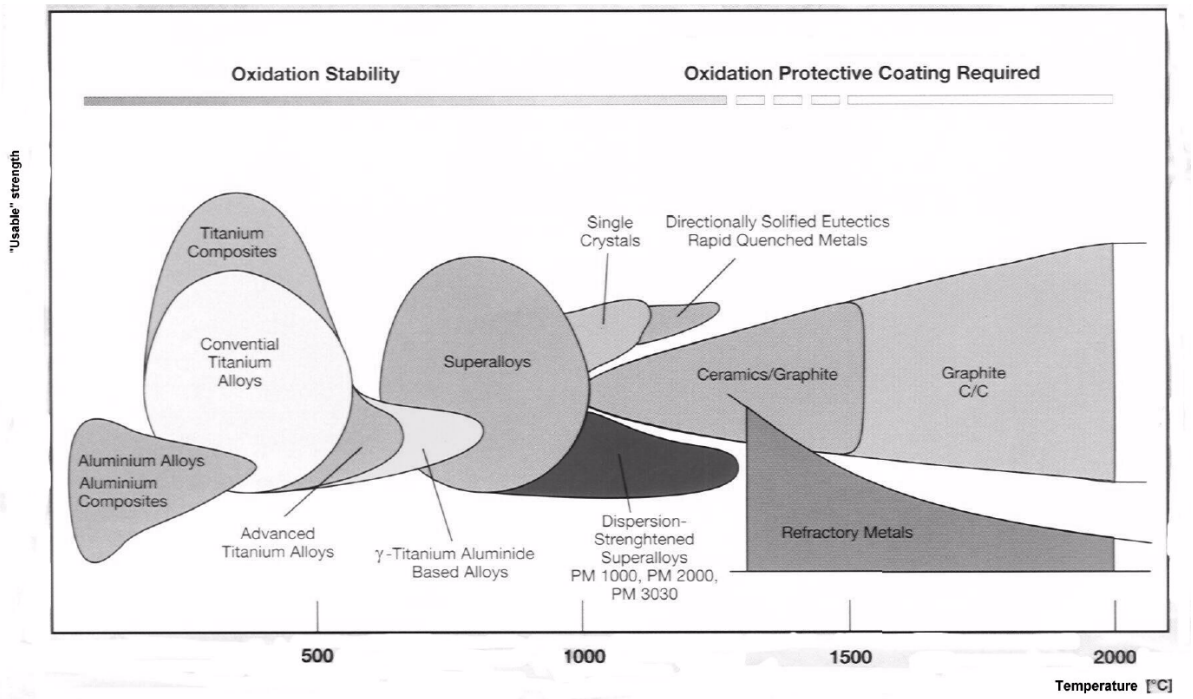

Figure 2.8: Operational use ranges of high temperature materials [39]

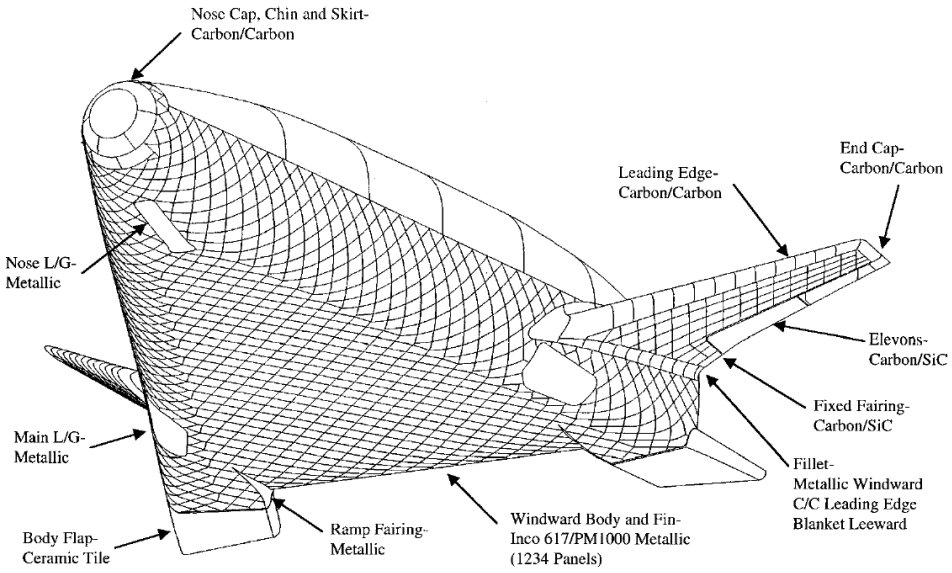

Figure 2.9: X-33 TPS of the windward side [37]

when deployed, and are made from ceramic and carbon/SiC. The rest of the main body will experience lower heat loads, and is composed of metallic materials.

For Aurora the most appropriate TPS options are discussed. First, possible passive TPS systems will be discussed, second different materials that are to be considered. Active systems will not be taken into account, as Aurora-R (the configuration which uses solely rocket propulsion) is selected as the nominal reference vehicle. Therefore the reentry phase is most likely the critical mission phase. The heat loads resulting from the reen-

try trajectory are thought to be managable by a passive TPS. Although an active TPS could also be functional and possibly weight saving, it is chosen to limit the TPS to be passive as there is more proven experience with passive systems in actual space missions. Moreover an active TPS is more complex and thus less reliable. The assumption that a passive TPS will suffice is confirmed in a preliminary study of the vehicle [25]. More elaboration on this subject is given in Section 2.3.

2.2.1. Passive TPS

Passive TPS methods work without active mechanisms present to protect the spacecraft from the extreme temperatures endured during spaceflight. An outer shell and/or special coatings are applied to the basic structure to protect the structure from the heat loads. In this subsection only an elaboration on insulation based TPS as form of passive TPS will be given. This is because an ablation-based TPS is not reusable, as an ablative coating has a chemical reaction under aerodynamic heat loads [41]. Therefore it is not suited for a RLV, such as Aurora. Insulation is used to cover the structure to protect it from aerodynamic heat loads. The insulation TPS experiences surface heating, and function by radiating (a large part of) this heat away, thus minimizing the resulting increase of temperature of the structure. No insulation has been produced as of yet that is able to radiate all the heat away, and so always a small part of the heat will be conducted to the structure. A schematic representation of the basic working of insulation is depicted in Figure 2.10 [20]. Insulation protects the structure beneath from the surface heating by storing part of the heat, while another part is transferred to the structure by conduction. Furthermore, heat is ejected from the vehicle by radiation to the environment.

Multilayer insulation

The most common passive TPS in space usage is Multilayer Insulation (MLI) [19]. MLI generally consists of three layers of insulation; an outer cover layer, an interior layer and an inner cover layer. Each layer has its own characteristics, as the insulation works both to prevent heating from and temperature losses to the environment. The outer layer must be able to endure the hostile environment and temperatures it is exposed to, and is required to be opaque to sunlight. The interior layer is generally desired to have a low thermal emittance. It is usually very thin compared to the outer layer to get a weight reduction and perforated to vent air that might be trapped during launch. The inner layer's main function is to protect the interior layer on one side and the spacecraft hardware on the other. Some typical MLI materials are listed in Table 2.1 per layer.

Ceramic tiles

Ceramic tiles are a type of insulation, which consists of fibrous silica with a low thermal conductivity. The tiles have a low density, but are also very fragile and brittle. A tougher outer coating can be applied to reduce the chance of damage by minor impacts. With the use of ceramic tiles it is more common to use a large number of small ones, compared to a smaller number of larger tiles. This is because they experience minimal thermal expansion, and thus do not move accordingly with an underlying structure that exhibits a larger expansion under heat loads. This typical construction of many small tiles, differing in size and shape, complicates the maintenance [12]. Another disadvantage of ceramic tiles is that they need to be waterproofed between flights

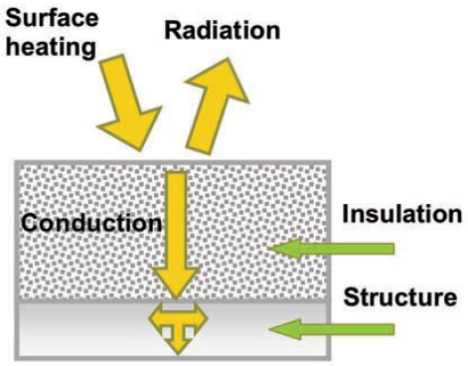

Figure 2.10: Schematic representation of the working of external insulation [20]

Table 2.1: Typical materials used in MLI TPS [19]

Outer cover layer	Fiberglass woven cloth impregnated with PTFE Teflon PVF reinforced with Nomex bonded with polyester adhesive FEP Teflon
Interior layer	Aluminzed Mular
Inner cover layer	Dacron netting Normex netting

[13]. The best known example of the use of tiles is the Space Shuttle, which experienced a stagnation heat load up to 200 kW/m^2 [14].

Flexible blankets
A variation on ceramic tiles are flexible blankets, also known as FEI. Silica fibers are encased in a woven cloth to produce the blanket. Other possible variations make use of ceramic or glass fibers [5]. Two significant advantages over the tiles are that they can be produced and applied in larger sizes, simplifying the required maintenance. Furthermore, the brittleness is lower than that of the tiles. The disadvantages of the blankets are that they require waterproofing between flights like the tiles, and are still easily damaged [12]. Besides, they are not suitable for areas with thin boundary layers as they trigger transition to turbulent flow [42]. Thus, they are only applicable on the leeward side of a spacecraft, were they were used in the case of the Space Shuttle. Blankets have been produced as insulation for temperatures up to 1350 K.

Surface Protected Flexible Insulation (SPFI)
SPFI combines FEI and CMC technologies, as it consists of a flexible blanket with a cover of a thin ceramic face sheet. The advantage over common flexible blankets comes from the rigid cover, which makes SPFI an attractive choice for the windward side of reentry vehicles on areas that experience high specific thermal loads [5]. SPFI can serve as TPS when temperatures up to 1475 K are reached. Table 2.2 portrays the limit temperatures of different insulation techniques. It must be noted that the reusable limit temperatures for the insulation materials are lower than the single use temperatures displayed in the table.

Metallic TPS
An option besides the previously discussed insulation based TPS to be used for RLVs is a metallic TPS. An example of a metallic TPS panel is given in Figure 2.11. In general a metallic TPS consist of a metallic box which encapsulates a light-weight fibrous ceramic insulation. This box rest on a support system, in the figure an RTV and nomex felt support. The box is attached to the structure by mechanical fasteners. High temperature superalloys are applicable for the highest temperature regions, whereas the lighter titanium alloys are applied to the lower temperature regions. The upsides of a metallic TPS are that they result in a more robust TPS. Furthermore the design is easily adaptable for different requirements by sizing the facesheet thickness. Also the encapsulation makes for a waterproof design. On the downside metallic TPS does not have an extensive usage history in space missions, compared to the other possible passive systems. As a result hereof it is also expected that the initial costs will be high. In the tool developed in the thesis work a metallic TPS is not considered, for these reasons as well as to be comparable to the one dimensional (1D) TPS design tool of DLR.

Table 2.2: Overview of the limit temperature of different insulations [5]

Name	Limit temperature [K]
Ceramics	1875
FEI	1375
SPFI	1475

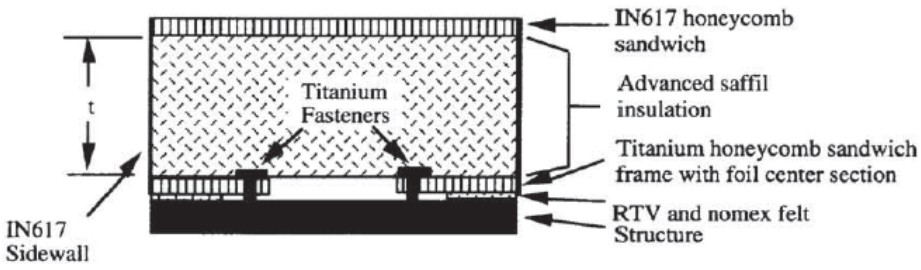

Figure 2.11: Example of a metallic TPS panel; the second generation superalloy honeycomb metallic TPS [34]

2.3. Aurora

The mission that will be the main subject for the thesis work is the Aurora mission. This project originated at DLR, more specifically the Space Launcher Systems Analysis (SART) department in Bremen. Aurora is planned to be an SSTO or semi-SSTO space launcher, with the option of using drop tanks for fuel storage [25]. There are two configurations planned to be developed, one using a rocket propulsion system (Aurora-R) and one using a combined air-breathing/rocket propulsion system (Aurora-AB). The vehicle is planned to have both a horizontal take-off and landing phase. Originally the mission was developed purely for cargo transport, but if a significant cost reduction compared to current space transportation systems is achieved, also human transport should be considered. Aurora is currently in its early development stage, with only a preliminary system design for the Aurora-R performed [25]. From this it was found that an exclusively passive TPS will be sufficient. It is chosen to limit the TPS design in the thesis work to a passive system, because there is more experience with passive systems and they are thus more proven. Furthermore active systems are more complex, and their development costs are thought to be higher. However, this could be subject to change after more elaborate studies have been performed. For the preliminary design of the Aurora-R the reentry trajectory is computed from an altitude of 120 km. The resulting maximum heat load and temperature over the trajectory are plotted in Figures 2.12 and 2.13. The heat flux reaches a maximum value up to 90.055 kW/m^2. For the temperature the value varies from 191.1 to 1176.3 K. It can be seen that the maximum values are reached after 1450 s. The temperature curve follows the same trend as the heat flux curve. At 1850 s another small peak can be found in the heat flux, leading to a small increase in the temperature. From their the heat flux gradually decreases to zero again, and the temperature also drops towards its minimum value. A cold or warm structure approach is preferred, to minimize the coupling between structure and TPS. A preliminary design of the Aurora-R vehicle is given in Figure 2.14. The vehicle is a wing-body configuration, with a circular shaped fuselage cross-section that is extended with a wing box, to enable the attachment of the wings. The delta shaped wing blends in with the fuselage, leading to a flat vehicle bottom. A fin is present to ensure yaw stability and control. The wing is equipped with elevons for pitch and roll control. In the design the placement of the drop tanks can be clearly seen below the vehicle wings. A summation of the properties of Aurora in terms of geometry and mass is provided in Table 2.3. In the thesis work a simpler model of Aurora is taken into account, consisting solely of the fuselage and wing, and their main structural components.

Table 2.3: Main properties of the Aurora-R [25]

Total length [m]	52.7
Wing span [m]	24.0
Maximum fuselage diameter [m]	5.75
Drop tank length [m]	24.0 - 33.0
Drop tank diameter [m]	2.4 - 3.2
Fuselage stored propellant mass [kg]	$15.0 \cdot 10^4$
Drop tank stored propellant mass [kg]	$24.0 \cdot 10^4$
Vehicle dry mass [kg]	$52.2 \cdot 10^4$
Drop tanks dry mass [kg]	$10.0 \cdot 10^4$
Payload mass [kg]	$7.0 \cdot 10^4$
Total take-off mass [kg]	$459.2 \cdot 10^4$

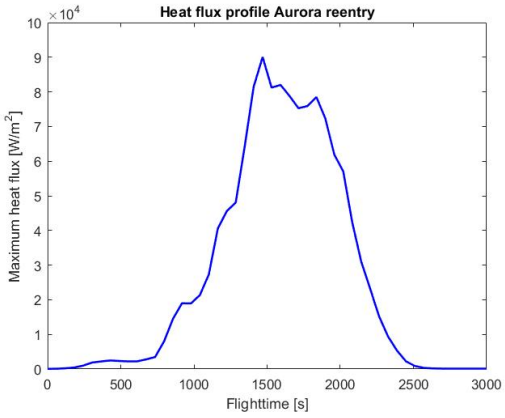

Figure 2.12: Maximum heat flux reentry Aurora-R

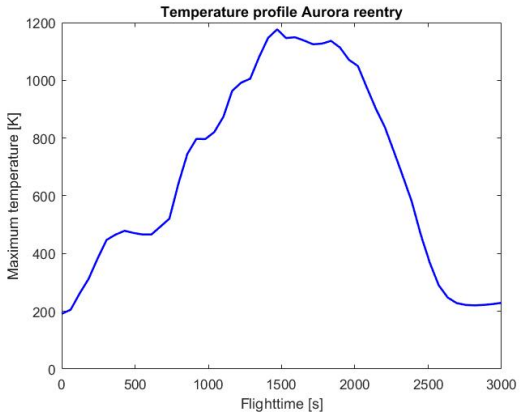

Figure 2.13: Maximum temperature reentry Aurora-R

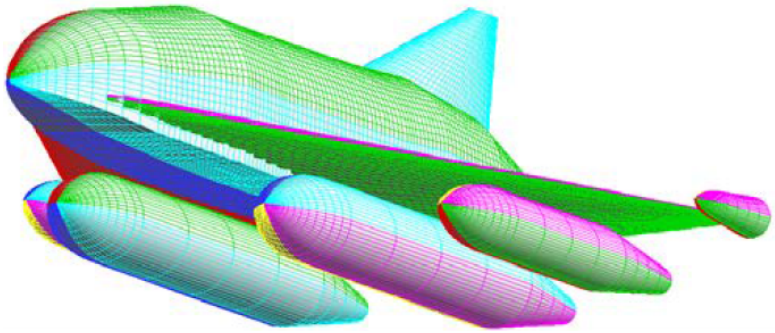

Figure 2.14: Preliminary design of the Aurora-R [25]

2.3.1. Restrictions

Some restrictions are applied on the thesis work, to simplify the model and keep it manageable within the restricted time frame. These restrictions lead to assumptions that are being made in the modeling of the problem. The restrictions are given below.

Restrictions

- Aurora-R is chosen as the nominal reference mission, thus it is assumed that the entry phase is the critical phase of the mission regarding heat loads
- TPS panels are not discretely modeled in the model, thus also panel gaps, seals, panel sizes and shapes are not taken into account to simplify the model

2.3.2. Aurora Requirements

Mission requirements

As taken from [25].

MR01 The vehicle shall transport payload into LEO.
MR02 The payload mass shall be 7000 kg.
MR03 The target orbit shall have a perigee height of 80 – 120 km and an apogee height of 400 – 600 km.
MR04 The vehicle shall be reusable with exception of the drop tanks for a minimal number of 10 missions.
MR05 The vehicle shall perform a horizontal take-off and landing.
MR06 The vehicle shall perform reentry, descent and landing in gliding mode without propulsion.
MR07 The vehicle shall experience a maximum normal acceleration of 2 g.
MR08 The vehicle shall experience a maximum axial acceleration of 4.5 g.
MR09 The Aurora-R vehicle shall experience a maximum dynamic pressure of 45 kPa.

System requirements

As taken from [25].

SR01 The vehicle length shall not exceed 55 m.
SR02 The vehicle wing span shall not exceed 30 m.
SR03 The vehicle shall be winged.
SR04 The Aurora-R vehicle shall be rocket powered.
SR05 The Aurora-R vehicle shall use drop tanks for propellant storage.
SR06 The maximum take-off weight of the vehicle shall not exceed 500,000 kg.
SR07 The propellant mass fraction shall be at least 80 %.
SR08 The TPS of Aurora-R shall consist of only passive TPS.
SR09 The maximum nose temperature shall not exceed 1200 K.
SR10 The maximum wing leading edge temperature shall not exceed 1800 K.
SR11 The maximum cold structure temperature shall not exceed 500 K.
SR12 The maximum temperature of the internal members shall not exceed room temperature, 293 K.

TPS requirements

TR01 The system shall be reusable for a minimal number of 10 flights.
TR03 The system shall not be subjected to degradation caused by oxidation.
TR04 The system shall maintain its interfaces with the primary (cold) structures.
TR05 The system shall have repair and replace procedures in case of damage.
TR06 The system shall keep the structural temperature below To Be Determined (TBD) K (around 500 K, the structural functional temperature of aluminum)).
TR07 The system shall keep the temperature of the internal members at room temperature at 293 K.

3

Flight Dynamics

In this chapter an elaboration is given on the flight dynamics of a winged re-entry vehicle. First the reference frames and transformations are given in Section 3.1. Secondly the models used to define Earth are introduced in Section 3.2. Thereafter in Section 3.3 the state variables of the flight are discussed. Section 3.4 elaborates on the external forces and moments experienced by the vehicle in flight. Lastly the Equations of Motion (EoM) are discussed in Section 3.5.

3.1. Reference Frames

The general flight dynamics theory that is the basis for the winged re-entry vehicle is treated in this section. First the relevant reference frames will be explained. Hereafter the transformations between reference frames is discussed.

3.1.1. Reference frame definitions

Multiple reference frames can be of use in the solving of a re-entry vehicle problem. One can divide the different frames into Earth-fixed and vehicle-fixed ones. All reference systems discussed in this sub-section are right-handed orthogonal systems. Which reference frame is most appropriate to use depends on the problem. The reference frames have been obtained from [30].

Intertial planetocentric reference frame F_I

The inertial planetocentric reference frame has its origin at the center of mass (c.o.m.) of the Earth. The $X_I Y_I$-plane is coinciding with the equatorial plane of the body. The Z_I-axis points north and coincides with the rotational axis of the body. The direction of the X_I-axis is determined by the reference meridian, which is defined by the zero-longitude at zero time. The right-handed system is completed by the Y_I-axis. The inertial reference frame does not rotate, even though the central body does. The inertial reference frame of Earth is shown in Figure 3.1.

Rotating planetocentric reference frame F_R

The rotating planetocentric reference frame coincides with the inertial reference frame at zero time and is fixed to the central body. The Z_R-axis points north, coinciding with teh rotational axis. The X_R-axis intersects the equator at a longitude of zero. The right handed system is completed by the Y_R-axis. The rotating reference frame of Earth is depicted in Figure 3.2.

Body-fixed reference frame F_B

The body-fixed frame is fixed to the body as the name says. The reference point and axes can be defined arbitrarily, but usually the following orientation is chosen. The c.o.m. serves as the vehicle's reference point. When the gravity field is constant the c.o.m. will coincide with the center of gravity (c.o.g.) of the vehicle. The X_B-axis is pointed forwards and lies in the vehicle's symmetry plane. The Z_B is directed downwards and also lies in the symmetry plane. The system is completed by the Y_B axis, which is directed perpendicular to the symmetry plane.

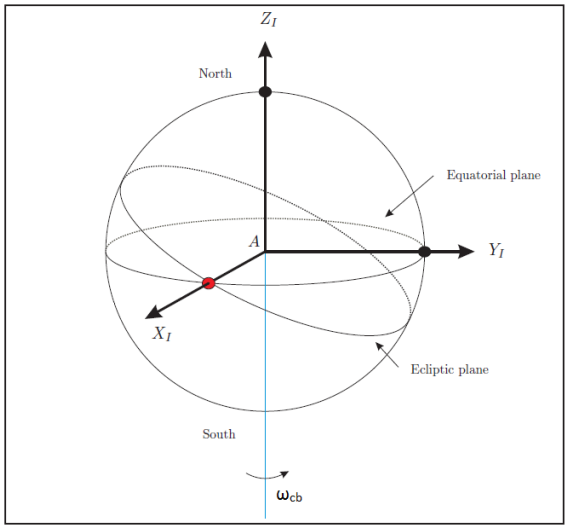

Figure 3.1: Earth-Centered Inertial (ECI) reference frame [33]

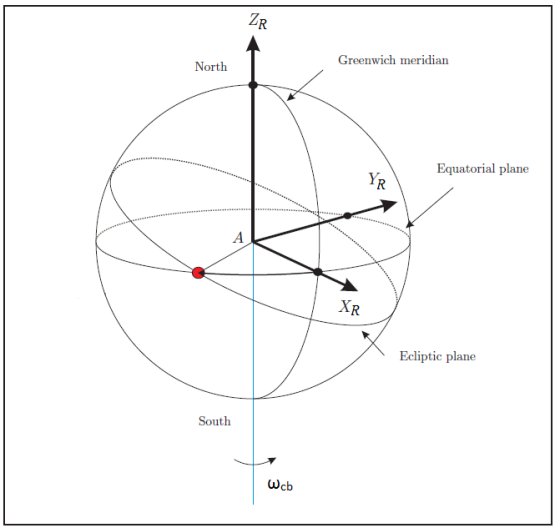

Figure 3.2: Earth-Centered, Earth-Fixed (ECEF) reference frame [33]

Vertical reference frame F_V
In the vertical reference frame the origin lies in the vehicle's c.o.m. as in the F_B frame. The Z_V-axis points towards the c.o.m. of Earth, along the radial component of the gravitational acceleration. The X_V-axis lies perpendicular to the Z_V-axis, in the meridian plane, and is pointed to the northern hemisphere. The Y_V-axis completes the right-handed system. The $X_V Y_V$-plane is often defined as the local horizontal plane.

Trajectory reference frame F_T
The trajectory reference frame is defined based on the groundspeed of the vehicle. The X_T-axis is positive along the vehicle's velocity vector relative to the atmosphere. The Z_T-axis is directed downwards in the vertical plane. Finally the right-handed system is completed by the Y_T-axis.

Aerodynamic reference frame F_A
The aerodynamic reference frame is also defined based on the airspeed, like the F_T frame. The X_A-axis is pointed along the velocity vector of the vehicle, relative to the atmosphere and is collinear with the X_T-axis. The Z_A-axis is then defined to be collinear with the aerodynamic lift force based on airspeed variables, but in opposite direction. The aerodynamic system is completed with the Y_A-axis, conform to the right-and rule. It can be noted that when the vehicle is not banking the T- and A-frame are coincident.

3.1.2. Transformations

The reference frames introduced in Subsection 3.1.1 are used to express the position and velocity of a spacecraft. With these parameters the motion of the vehicle can be determined. To produce the overall motion of the vehicle, motions (velocities and accelerations) from different reference frames need to be expressed in one reference frame. Therefore, transformations are used.

Euler angles can be used to express the rotation transformation between two different reference frames. Alternatively Directional Cosine Matrices can be used for the transformations, or quaternions [30]. In the scope of this study it is decided to focus solely on the transformation method based on Euler angles. A total of three Euler angles are defined; φ_x, φ_y and φ_z. They represent a rotation around the X-axis, Y-axis and Z-axis respectively. By using body-referenced Euler angles the orientation of one reference frame compared to another can be described. The amount of rotations needed depends on the particular frame transformation. One must note that only the orientation of a reference frame is addressed by Euler angles, hence the reference point of the system does not change.

With the use of Euler angles transformation matrices can be computed. A transformation matrix holds all the necessary transformation angles required to express the position of a body from one reference frame to another. It thus describes the orientation of the one with respect to the other. A maximum of three (sub-

)matrices can be used to form the total transformation matrix when Euler angles are used. At most one per axis around which a rotation takes place.

A rotation around the X-axis will be demonstrated. Figure 3.3 shows this rotation. The transformation matrix for a rotation around the X-axis can now be defined as in Equation (3.1). Such a transformation matrix is called a unit-axis transformation matrix.

$$\mathbb{T}_{21} = \mathbb{T}_x = \begin{bmatrix} 1 & 0 & 0 \\ 0 & \cos\varphi_x & \sin\varphi_x \\ 0 & -\sin\varphi_x & \cos\varphi_x \end{bmatrix} \tag{3.1}$$

In the same manner the unit axis transformation matrices $\mathbb{T}_y$ and $\mathbb{T}_z$ can be computed. They are displayed in Equation (3.2) and (3.3) respectively. The unit transformation matrices are all orthonormal, thus its inverse is simply its transpose.

$$\mathbb{T}_y = \begin{bmatrix} \cos\varphi_y & 0 & -\sin\varphi_y \\ 0 & 1 & 0 \\ \sin\varphi_y & 0 & \cos\varphi_y \end{bmatrix} \tag{3.2}$$

$$\mathbb{T}_z = \begin{bmatrix} \cos\varphi_z & \sin\varphi_z & 0 \\ -\sin\varphi_z & \cos\varphi_z & 0 \\ 0 & 0 & 1 \end{bmatrix} \tag{3.3}$$

When for a transformation between two reference frames rotations around multiple axes are required, the total transformation matrix can be computed by multiplying the unit axis matrices in sequential order. For example, if a transformation is needed with the rotation sequence $\varphi_z \rightarrow \varphi_y \rightarrow \varphi_x$ the total transformation matrix can be computed as shown in Equation (3.4). The vector expressed in the second reference frame is then calculated by Equation (3.5).

$$\mathbb{T}_{21} = \mathbb{T}_x \mathbb{T}_y \mathbb{T}_z \tag{3.4}$$

$$\mathbf{v}_2 = \mathbb{T}_{21} \mathbf{v}_1 \tag{3.5}$$

A transformation matrix satisfies two criteria. First the matrix must be orthogonal, as it represents a rotation from one orthogonal reference system to another. Second the determinant of the rotation matrix must be equal to 1. This is because the vector will not have changed its length after the rotation. The frame transformations used within the thesis work are stated in Appendix A.

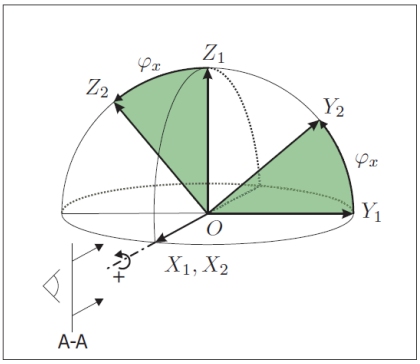

Figure 3.3: Rotation around the X-axis [33]

3.2. Earth Model

The body from and to which the space vehicle flies is of importance in the trajectory simulations. For the project at hand Earth is taken as the body from and to which the trajectories need to be modeled, for the reference mission Aurora. Therefore the shape and most importantly the atmosphere of Earth will be discussed, in Subsections 3.2.1 and 3.2.2 respectively. Gravity is elaborated upon in Subsection 3.4.2.

3.2.1. Shape

The Earth is not a perfect sphere, but has an irregular shape determined by many factors, such as gravitational tides, winds and plate motion. To simplify calculations, the Earth is usually modeled as a sphere, or oblate sphere, or when higher precision is desired as an ellipse. For calculations of flight very close to the Earth's surface a flat Earth approximation is sufficient. For the trajectory simulation of the thesis work a rotating spheroid will be used to model the Earth's shape. This is chosen as the trajectory simulation that will be used as a basis for the trajectory simulation to be computed (see Appendix C) also assumes the Earth to have a spherical shape. Furthermore, in the simulation of a reentry trajectory this assumption does not lead to a large error, as the actual change in the gravity force will not be very large during reentry. The vehicle is relatively close to the Earth.

3.2.2. Atmospheric model

The atmosphere has a large influence in the design of a TPS, as due to friction between the vehicle and atmosphere the vehicle heats up to high temperatures. Besides, the friction causes the vehicle to slow down during re-entry, as kinetic energy is converted into heat, which is helpful in reaching acceptable landing speeds [30].

To model the atmosphere to a very high degree of accuracy is a very challenging task, and also not necessary for the trajectory simulation [30]. It is sufficient to use a simplified atmosphere model. Use will be made of the US Standard Atmosphere 1976 (US76). This model is chosen for its accurate representation of the atmosphere, while still being relatively simple. The US76 is the most common used atmospheric model in aerospace applications. In a standard atmosphere it is assumed that the physical properties such as density, pressure and temperature, are solely dependent on the altitude. An alternative to standard atmospheres are reference atmospheres, where temporal variations are taken into account. Reference atmospheres are by definition more complex and detailed than standard atmospheres, up to a level that is deemed unnecessary in the thesis work. A depiction of the US76 atmospheric model, for the temperature, speed of sound, pressure and density is given in Figure 3.4. The figure provides the trends up to an altitude of 100 km. The US76 model assumes that the atmosphere is an ideal gas, and thus obeys the ideal gas law [35]:

$$p = \rho RT = \rho \frac{R^*}{M} T \tag{3.6}$$

Here R is the gas constant for air, equal to $\frac{R^*}{M}$. The density and temperature are given by ρ and T respectively. R^* is the universal gas constant and M is the molecular mass of the atmosphere. Furthermore it is assumed that the atmosphere is in a state of hydrostatic equilibrium, where the hydrostatic equation is:

$$dp = -\rho g dz \tag{3.7}$$

where p is pressure and z the geopotential altitude. The relation between the gepotential and geometric altitude h is given by:

$$g_0 z = g dh \tag{3.8}$$

The last assumption is that the atmosphere is homogeneous to an altitude of 80 km.

Temperature

Within the atmosphere there are different regions for which the temperature can be calculated in different ways. For temperatures up to 86 km the molecular shape temperature T_M is used.

$$T_M = T \frac{M_0}{M} \tag{3.9}$$

[1] Image from https://commons.wikimedia.org/wiki/File:Comparison_US_standard_atmosphere_41962.svg visited on 22/03/2017

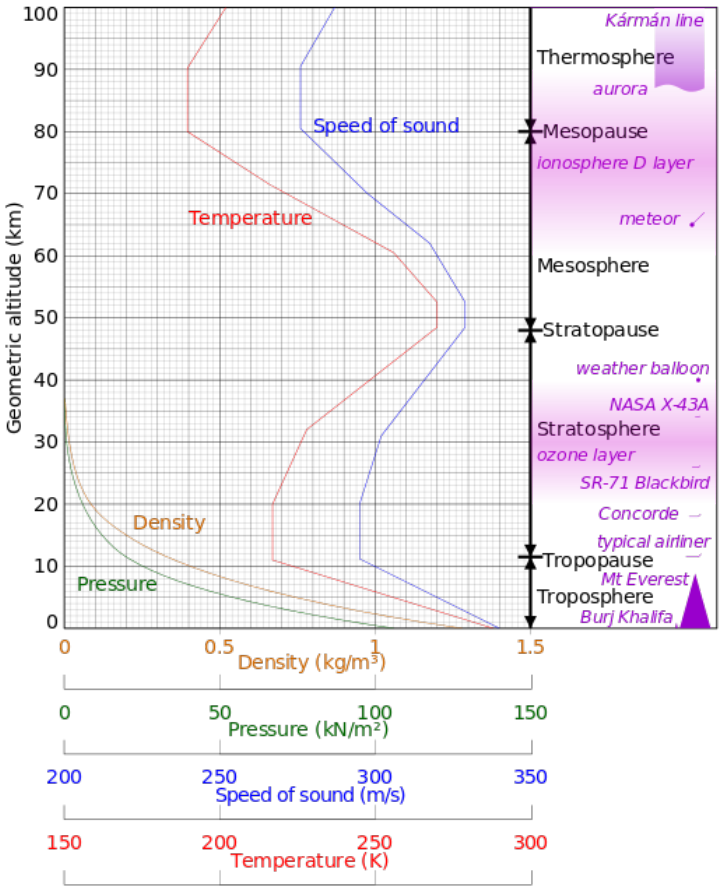

Figure 3.4: US76 atmospheric model for temperature, speed of sound, pressure and density [1]

M is the mean molecular weight and M_0 the mean molecular weight at sea level ($28.9644 \cdot 10^{-3}$ kg/mol). At altitudes higher than 86 km the model is based on the geometric altitude. Three functions are made relating the temperature to the altitude z, for three atmosphere regions having different atmospheric conditions [30].

The first layer is from 86 – 91 km and is isothermal, thus the temperature is constant given by

$$T = T_7 = 186.863K \tag{3.10}$$

The second layer has altitude 91 – 110 km and has an elliptically shaped temperature-altitude function:

$$T = T_c + A\sqrt{1 - \frac{z - z_8^2}{a}} \tag{3.11}$$

Here T_c is 263.1905 K, A is −76.3232 K, a is −19.9429 km and z_8 is an altitude of 91 km.

The third region, going from 110 – 120 km, has an exponential function running towards an asymptote for increasing values of z.

$$T = T_9 + L_{K9}(z - z_9) \tag{3.12}$$

In this function T_9 is 240.0 K L_{K9} is 12.0 K/km and z_9 is 110 km.

The equation for the atmospheric pressure is a variation on the ideal gas law:

$$p = \frac{NR^* T}{N_A} \tag{3.13}$$

In this equation N is the total number density (m^{-3}) and N_A is Avogadro's constant ($6.0225 \cdot 10^{26}$ $kmol^{-1}$). The total number density is computed by linear interpolation. The atmospheric density is computed by the ideal gas law, where M is taken from linear interpolation. Finally the speed of sound is calculated as follows:

$$a = \sqrt{\gamma RT} \tag{3.14}$$

where γ is the ratio of specific heats of 1.4, and R the gas constant of 287 $JK^{-1}kg^{-1}$. The ratio of specific heats is a simple fraction; $\frac{C_p}{C_v}$, in which C_p and C_v are the specific heat at constant pressure and volume respectively.

3.3. State Variables

State variables are used to present the instantaneous state of a vehicle with respect to a certain reference frame. In this section first state variables used to describe the position and velocity of a vehicle will be discussed, after which expressing the attitude of a vehicle with state variables will be elaborated upon.

3.3.1. Position and velocity

There are different notations that can express position and velocity state variables. Cartesian components are often preferred to perform numerical computations as the equations are simpler and the numerical integration is usually faster. Spherical components, though, are more intuitive to use. Therefore the state of a vehicle is easier to discuss in spherical components, when the actual computations are performed with Cartesian components. Kepler elements are most applicable to describe the state of a vehicle in orbit, and are not discussed in the scope of this literature study as only the ascent and re-entry phase will be evaluated in the thesis work.

Cartesian components

Cartesian components usually express the position and velocity with respect to the inertial reference frame F_I or the rotating reference frame F_R. The same notation is used to express the position for both reference frames $\mathbf{p}(x, y, z)$, but with different subscripts to indicate the frame (I and R respectively). The velocity components are expressed differently based on the choice of reference frame: $\mathbf{V_I}(\dot{x}, \dot{y}, \dot{z})$ and $\mathbf{V_R}(u, v, w)$.

Spherical components

Spherical components are denoted with respect to the F_R frame. The position and velocity components both consist of a magnitude and two angular components. Their notations are position $\mathbf{p}(R, \tau, \delta)$ and velocity $\mathbf{V}(V, \gamma, \chi)$. Distance R measures the radial distance between the c.o.m. of the central body, hence the origin of F_R, and the c.o.m. of the vehicle. The longitude τ measures the angular distance from the Greenwich merid-

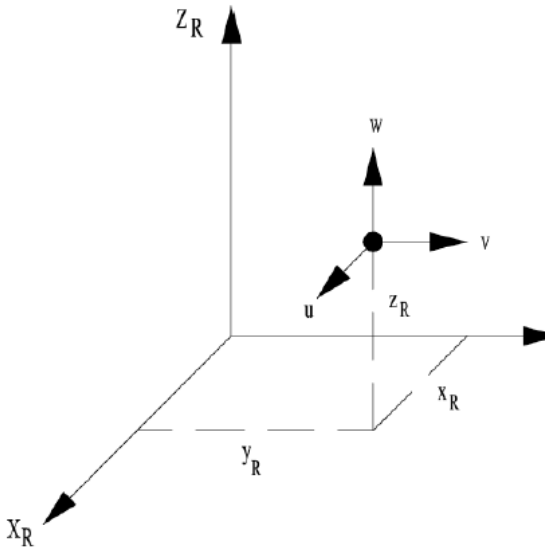

Figure 3.5: Definition of the Cartesian components with respect to the reference frame F_R [30]

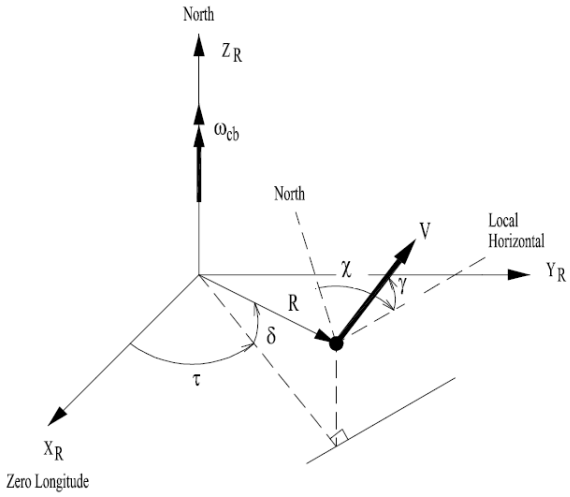

Figure 3.6: Definition of the spherical components [30]

ian and is positive towards the east ($0\,\text{deg} \leq \tau < 360\,\text{deg}$). The latitude δ is the angular distance measured from the equator towards the north, it is positive in the northern hemisphere and negative in the southern ($-90\,\text{deg} \leq \delta \leq 90\,\text{deg}$).

The relative velocity V is the modulus of the velocity vector **V**. The flight path angle γ is the angle measured between the vector **V** and the local horizontal plane. It is negative when **V** is below the local horizon ($-90\,\text{deg} \leq \gamma \leq 90\,\text{deg}$). Finally, the heading angle χ defines the direction of **V** in the local horizontal plane and the local North. If the vehicle moves eastward the angle is positive ($-180\,\text{deg} \leq \chi < 180\,\text{deg}$).

3.3.2. Attitude

The attitude of a vehicle expresses the orientation of a body-fixed reference frame with respect to another reference frame. There are multiple ways to describe the attitude. In the scope of the study at hand the attitude will be limited to a description using aerodynamic angles. Classical attitude angles (roll, pitch and yaw) describe the body frame with respect to the inertial space or the local horizontal plane. The aerodynamic angles are preferred as they are more common to describe the attitude of a spacecraft, and can easily be implemented in the EoM. Quaternions eliminate the occurrence of singularities in a transformation. As singularities typically occur with large rotation angles they are not expected in the scope of the thesis subject and thus are not deemed necessary.

The aerodynamic angles consist of the angle of attack α, the angle of sideslip β and the bank angle σ. The angle of attack describes the angle between **V** and the body axis of the vehicle in the vertical plane, and is positive in a nose-up attitude ($-180\,\text{deg} \leq \alpha < 180\,\text{deg}$). The sideslip angle measures between **V** and the vehicle's body axis in the horizontal plane. It is positive for a nose-left attitude ($-90\,\text{deg} \leq \beta \leq 90\,\text{deg}$). Finally the bank angle describes the inclination of the vehicle about its longitudinal axis, and is positive when banking is performed to the right ($-180\,\text{deg} \leq \sigma < 180\,\text{deg}$). Figure 3.7 shows the orientation of the aerodynamic attitude angles. The use of these angles in the equations of motion define the attitude of the vehicle with respect to the ground speed.

3.4. External Forces

There is a number of external forces and moments that work on a spacecraft. For the thesis work rotational motion will not be considered as it increases the complexity of the simulation while it is expected not to have a significant impact on the outcome of the TPS. Thus it is assumed that the spacecraft performs solely instantaneous rotations during flight, and only the forces will be discussed in this section. When the reentry phase of the vehicle is considered, the working forces primarily consist of aerodynamic and gravitational ones.

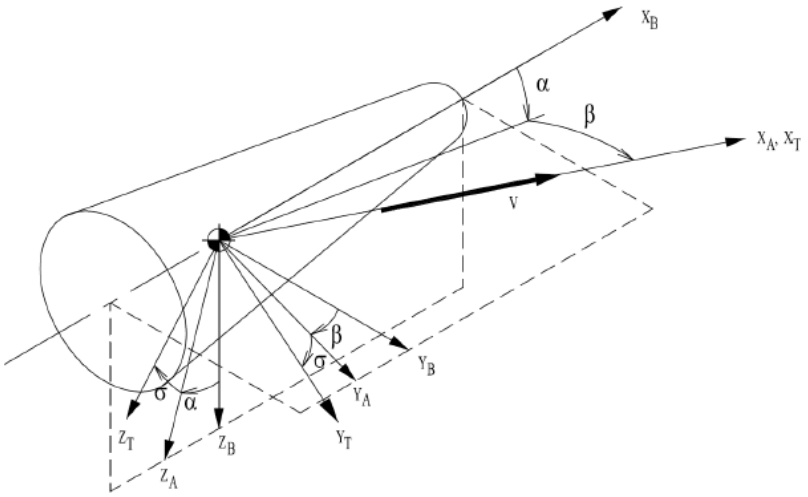

Figure 3.7: Definition of the aerodynamic attitude angles with respect to reference frames F_B, F_A and F_T [30]

3.4.1. Aerodynamics

The aerodynamic forces depend on the atmospheric density ρ and the previously discussed variables V, α and β. The variable σ is also taken into account to define the reference frame. The aerodynamic conditions for the vehicle are represented by the Mach number M and the dynamic pressure $\bar{q}$. The equations for both quantities are given below, where a is the speed of sound.

$$M = \frac{V}{a} \tag{3.15}$$

$$\bar{q} = \frac{1}{2}\rho V^2 \tag{3.16}$$

Forces

Equation (3.17) represents the aerodynamic forces in the aerodynamic reference frame F_A, where D, S and L respectively are the aerodynamic drag, side and lift force, C_D, C_S and C_L their coefficients, and S_{ref} the reference area.

$$\mathbf{F_{A,A}} = -\begin{bmatrix} D \\ S \\ L \end{bmatrix} = -\begin{bmatrix} C_D \bar{q} S_{ref} \\ C_S \bar{q} S_{ref} \\ C_L \bar{q} S_{ref} \end{bmatrix} \tag{3.17}$$

There are minus signs because the components are defined opposite in direction compared to the axes of the F_A frame. The aerodynamic force coefficients are dimensionless and unique for every vehicle. The coefficients are varying with Mach number and aerodynamic angles, and they must be obtained empirically. When aerodynamic forces have to be simulated models and tabulated values can be applied which comprise the relation between the coefficients, Mach number and attitude angles.

3.4.2. Gravity

In the reentry phase of a space mission the central body, in the thesis work Earth, will exert a gravitational force on the vehicle. Newton's Law of gravitation expresses the attractive force $\mathbf{F_G}$ that two point masses exert on one another when they are a vector distance $\mathbf{r}$ apart (Equation (3.18)). Here G is the universal gravity constant (G=6.67259 $\cdot 10^{-11} \mathrm{m^3 s^{-2}}$), M is the mass of the central body, m is the vehicle mass, R is the modulus of the vector distance $\mathbf{r}$ and $\hat{\mathbf{r}}$ is the normalized vector distance.

$$\mathbf{F_G} = \frac{GMm}{R^2}\hat{\mathbf{r}} \tag{3.18}$$

The gravitational potential of the central body is expressed in Equation (3.19). The gravitational parameter μ of the central body is computed by taking the product of the universal gravity constant and the body's mass GM. Equation (3.19) is also known as the central field model and represents the simplest approximation of the gravitational potential.

$$U = -\frac{\mu}{R} \tag{3.19}$$

3.5. Equations of Motion

In the trajectory simulation that will be used in the thesis work the equations of motion are implemented in Cartesian coordinated in the inertial reference frame F_I [38]. An elaboration on the trajectory simulation is given in Chapter C. All components to be used in the simulation are thus first transformed to the F_I frame before numerical computations. The motion of a vehicle can be divided into the motion of the c.o.m. and the motion around the c.o.m., the translational and rotational motion respectively. In the thesis work three degrees of freedom of the translational motion will be taken into account. Rotational motion is only considered in the sense that the vehicle remains trimmed during the ascent and entry phase.

3.5.1. Translational Motion

The equations of the translational motion give information about the position and velocity of the vehicle in three directions, or degrees of freedom. For a high-velocity spaceplane the assumptions of a non-rotating and flat Earth cannot be used, as they would introduce significantly large errors. Therefore it is preferred to set up the equations of motion in the rotating reference frame F_R. This definition makes it easier to understand and interpret the equations. It is assumed that the Earth has a spherical shape, with an according spherical gravity field, and it has a constant rotation represented by angular velocity, ω_{cb}. This assumption

is made to simplify the equations, and is expected to not have a large effect on the final outcome of the thesis. Furthermore, it is assumed that the vehicle is not subjected to wind forces nor longitudinal gravitational acceleration. The equations can be either expressed in Cartesian or spherical components, or a combination of the two. For numerical applications the Cartesian method is preferred, as it is much less complex and thus less time-consuming for numerical integration. However, spherical components are easier to interpret and understand, and provide more inside in the physics of the vehicle's motion. Therefore both methods will be explained.

Cartesian components
In the trajectory simulation to be used as a basis in the thesis work the equations of motion are expressed in Cartesian coordinates in the F_I frame. Equations (3.20a) and (3.20b) define the translational motion of a rigid body in the inertial frame F_I for a rigid boy with constant mass. The first equation is known as the dynamic equation and represents the acceleration vector of a body due to external forces. The second is the kinematic equation which describes the velocity of the body. In these equations r_I is the distance to the origin of the reference frame, F_I represents the total external force the vehicle is subjected to, m is the vehicles mass and V_I is the vehicle's inertial velocity.

$$\frac{d\mathbf{V_I}}{dt} = \frac{1}{m}\mathbf{F_I} \tag{3.20a}$$

$$\frac{d\mathbf{r_I}}{dt} = \mathbf{V_I} \tag{3.20b}$$

The Cartesian position and velocity state variables were discussed in Section 3.3, and their respective vectors in the inertial frame are given by Equations (3.22a) and (3.22b).

$$\mathbf{r_I} = (x_I, y_I, z_I)^T \tag{3.21a}$$

$$\mathbf{V_I} = (\dot{x}_I, \dot{y}_I, \dot{z}_I)^T \tag{3.21b}$$

The Cartesian position and velocity are expressed in the rotational frame with the transformation matrix $\mathbb{T}_{R,I}$, which is the transpose of $\mathbb{T}_{I,R}$, introduced in Appendix C. Their respective equations are:

$$\mathbf{r_R} = \mathbb{T}_{R,I}\mathbf{r_I} \tag{3.22a}$$

$$\mathbf{V_R} = \mathbb{T}_{R,I}(\mathbf{V_I} - \omega_{cb} \times \mathbf{r_I}) \tag{3.22b}$$

The resulting force the vehicle is subjected to is dependent on the flight phase that is considered. For a rocket-based vehicle the reentry phase is critical. In the reentry phase the resulting external force consists of the aerodynamic and gravitational and propulsion forces, as shown in the following equation.

$$F_{I_{reentry}} = \mathbf{F_{A,I}} + \mathbf{F_{G,I}} \tag{3.23}$$

The resulting dynamic and kinematic equations are as follows.

$$\frac{d\mathbf{V_I}}{dt} = (\ddot{x}_I, \ddot{y}_I, \ddot{z}_I)^T = \frac{1}{m}\mathbf{F_I} \tag{3.24a}$$

$$\frac{d\mathbf{r_I}}{dt} = (\dot{x}_I, \dot{y}_I, \dot{z}_I)^T \tag{3.24b}$$

Both the aerodynamic force and the gravitational force are computed in different reference frames, the aerodynamic frame F_A and the vertical frame F_G respectively. Their transformation to the inertial frame is given in Equations (3.25a) and (3.25b).

$$\mathbf{F_{A,I}} = \mathbb{T}_{I,A}\mathbf{F_{A,A}} \tag{3.25a}$$

$$\mathbf{F_{G,I}} = \mathbb{T}_{I,V}\mathbf{F_{G,V}} \tag{3.25b}$$

Spherical components
In Section 3.3 the state variables were introduced. As stated the position of the vehicle is defined by the distance R, longitude τ and latitude δ, whereas the velocity is defined by its magnitude V, flight-path angle

γ and heading angle χ. The coordinate transformation from Cartesian position to spherical components is given below [36].

$$R = \sqrt{x^2 + y^2 + z^2} \tag{3.26a}$$

$$\tau = \arctan \frac{y}{x} \tag{3.26b}$$

$$\delta = \arccos \frac{z}{\sqrt{x^2 + y^2 + z^2}} \tag{3.26c}$$

The spherical velocity component V is found by the following equation:

$$V = \sqrt{u^2 + v^2 + w^2} \tag{3.27}$$

A transformation of the velocity vector from the rotational frame to the vertical frame can be performed with transformation matrix $\mathbb{T}_{V,R}$, which is the inverse of matrix $\mathbb{T}_{R,V}$ introduced in Appendix C.

$$\mathbf{V_V} = \mathbb{T}_{V,R}\mathbf{V_R} \tag{3.28}$$

The projection of V_G in the local horizontal plane is equals the sum of v_x and v_y. The flight path angle $gamma$ and heading angle X can be computed with the following equations.

$$\gamma_G = \arccos\left(\frac{\sqrt{v_\delta^2 + v_\tau^2}}{V_G}\right) \tag{3.29}$$

$$X = \arctan\left(\frac{v_y}{v_x}\right) \tag{3.30}$$

For completion also the transformation from spherical to Cartesian coordinates is given.

$$x = R\cos\delta\cos\tau \tag{3.31a}$$

$$y = R\cos\delta\sin\tau \tag{3.31b}$$

$$z = R\sin\delta \tag{3.31c}$$

3.5.2. Rotational Motion

The only rotational motion that is considered is rotation over the longitudinal direction of the vehicle, i.e. the pitch motion. An equilibrium is considerd to keep the vehicle in a trimmed flight condition. This condition is reached when the sum of the pitch moments C_m of the vehicle with a 0° body angle C_{m_0}, and the induced moment caused by a body angle deflection C_{m_b} is zero.

$$C_m = C_{m_0} + \Delta C_{m_b} \tag{3.32}$$

The zero angle moment coefficient is function of the angle of attack and Mach number: $C_{m_0} = f(\alpha, M)$. The moment coefficient increment depends on angle of attack and Mach number, as well as the body flap deflection δ_b: $C_{m_b} = f(\delta_b, \alpha, M)$. As in trimmed condition the total moment coefficient equals zero, the needed change in moment coefficient resulting from the body flap deflection follows from the body coefficient.

$$\Delta C_{m_b} = -C_{m_0} \tag{3.33}$$

The deflection of the body flap is than determined to be such that the ΔC_{m_b} is reached. The tables with the aerodynamic coefficients for the Aurora vehicle are stated in Appendix B. The bodyflap function of Aurora is fulfilled by two wing flaps, one on each side. Their deflection is calculated by inversely interpolation of the coefficients over the deflection angles for the current angle of attack and Mach number. At every step of the trajectory the moment coefficient increment for the current combination of angle of attack and Mach number is computed for all known bodyflap deflections. Between these values an interpolation is performed to find the value of ΔC_{m_b} for which Equation (3.33) is met.

4

Aerothermodynamics

Aerothermodynamics are an important aspect in the design of a TPS. The spacecraft heats up due to aerodynamic friction, after which the heat spreads through the vehicle. In the thesis work it is assumed that the temperature increase of the vehicle occurs solely due to aerodynamic heating, an elaboration of this is made in Section 4.1. In Section 4.2 heat transfer through conduction and radiation are discussed. The thermal energy balance of the vehicle is presented in Section 4.3. The DLR tool HOTSOSE is used to obtain the heat flux over the vehicle that follows from the chosen trajectory. The theory behind this tool is presented in Section 4.4. Section 4.5 gives a description of the influence of thermal loading to the structure.

4.1. Aerodynamic heating

A spacecraft in reentry phase, entering the atmosphere at high velocity, has a large amount of kinetic energy. Due to pressure drag and friction between the skin of the vehicle and the atmosphere the vehicle decelerates, as the kinetic energy is converted into heat. The heat input of the vehicle is found by taking the integral of the heating rate over the entire trajectory. The heating rate is a complex property to exactly calculate and depends on the vehicle specific hypersonic aerodynamic properties.

$$q_c = c^* R_N^n \left(\frac{\rho}{\rho_0}\right)^{1-n} \left(\frac{V}{V_c}\right)^m \tag{4.1}$$

Equation (4.1) gives a good approximation of the heating rate q_c [11]. Here R_N is the vehicle's nose radius, ρ and ρ_0 are the atmospheric density and density at sea level respectively, V is the velocity of the vehicle and V_c is the circular velocity at the vehicle's altitude. c^*, n and m are constants, their values are given to be $c^* = 1.1097 \cdot 10^8$, $n = 0.5$ and $m = 3.15$ [11]. The value of 0.5 for n assumes a laminar flow, whereas a value of 0.33 would be used for a turbulent flow. The constants describe the airflow characteristics around the body, however their derivations are not in the scope of the thesis work.

The reentry conditions have a large influence on the level of aerodynamic heating. Higher entry velocities and higher entry angles typically result in higher heat loads. The entry angle is best kept as low as possible to reduce heating, especially for RLVs. However, when the entry angle is too low it can result in a skipping flight. The vehicle then generates enough lift to increase altitude again, when touching upon the atmosphere, hence a skipping flight.

4.2. Heat Transfer

Heat transfer can take place through multiple methods. In the thesis work only heat transfer through conduction and radiation will be taken into account. Convection arises from temperature differences through a body of fluid, and are thus not applicable for the thesis work, as the TPS and structure of the space vehicle are solid.

4.2.1. Conduction

In thermal conduction heat is transferred by collisions of particles and the movement of electrons. Conduction through solids, such as in a launcher vehicle, works through molecules vibrating about fixed positions.

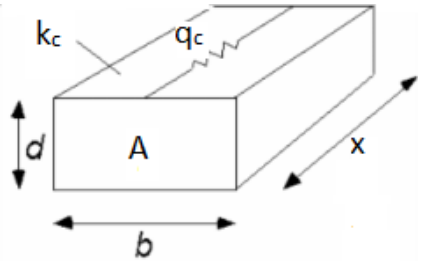

Figure 4.1: Heat transfer by conductivity[1]

Energy is transmitted from molecules with a higher energy content to adjacent molecules with a lower temperature performing less violent motions. Free electrons passing through the molecular lattice also transfer energy, especially in metallic materials. Conduction through solids is shown in Equation (4.2) in a simplified form [22]. Here, k_c is the thermal conductivity of the material, A is the transfer area and x the length, and T_1 and T_2 are respective locations of the solid body. Conduction is visualized in Figure 4.1.

$$q_{cond} = \frac{k_c A}{x}(T_1 - T_2) \tag{4.2}$$

Heat conduction through liquids, gases and vapors can only occur when thin layers of fluid are present. When the body of the fluid is too thick, density differences will occur between the different temperature regions, resulting in convection heat transfer. In practice true conduction takes place through stationary fluid layers that adhere to a surface. Conduction is purely dependent of the properties of the fluid, whereas convection depends on the properties of the fluid and condition of the motion [22].

4.2.2. Radiation

Heat transfer through radiation takes place in all heated objects. The radiant energy is transmitted via space, and heats up any absorbing object. The energy properties, intensity and frequencies, depend on the material and its temperature. The radiation heat transfer is given in Equation (4.3), where ϵ is the emissivity, σ is the Stefan-Boltzmann constant, A is the surface area and F the geometric form factor. The geometric form factor, also known as the view factor, is defined as the fraction of the radiation emitted by one surface that is directly incident on the sink surface. When two surfaces are very close to each other the view factor will approach 1. $T_{surface}$ and T_{sink} are are respectively the surface and radiation sink temperature. Thermal radiation is affected by the surface properties, such as reflectivity, absorptivity, and transmissivity, and geometric form factors [22].

$$q_{rad} = \epsilon \sigma A F (T^4_{surface} - T^4_{sink}) \tag{4.3}$$

4.3. Thermal Energy Balance

Not all heat the vehicle is subjected to is being transferred away, some of it is also stored. The thermal energy that is stored in a body is represented by Equation (4.4), where ρ is the density, V the volume, C_p the specific heat and dT/dt represents the temperature rate of change.

$$q_{stored} = \rho V C_p \frac{dT}{dt} \tag{4.4}$$

An energy balance equation can now be drafted, when one keeps in mind that thermal energy can not disappear and thus $q_{in} = q_{out}$. In the equation q represents the incoming source heat flux [22]. Conduction of the vehicle's TPS can take place both inwards (to the vehicle interior) and sideways [9].

$$q - q_{cond} - q_{conv} - q_{rad} = q_{stored} \tag{4.5}$$

When a first approximation is to be made for a passive TPS, there are some assumptions that can be made. As the level of heating is approximately constant along the surface sideways conduction can be neglected,

[1] Private communication, Martin Lemmen, November 2016

because the heat difference is minimal. Light-weights materials are typically used on launchers, therefore the stored energy can be assumed close to zero and can thus be neglected in a first approximation. Insulation is usually present in the launcher, preventing the interior from heating up, thus inwards conduction can be neglected. Finally, an uncooled system will not make use of convection, so this can be assumed non-existent. An equation remains that enables a direct wall temperature calculation from the incident heat flux (Equation (4.6)) [9]. Due to all the assumptions this simplified equation provides the upper limit estimation of the wall temperature.

$$q = \sigma \epsilon T_{wall}^4 \tag{4.6}$$

4.4. Theory Heat Flux Distribution Tool

To determine the heat flux distribution over the vehicle surface the DLR tool HOTSOSE is used. Based on the reference trajectory the heat flux is calculated over the vehicle for every time point. In this section the theory that is applied in HOTSOSE to calculate the heat flux distribution is presented, as well as the assumptions that are made[2]. The methods used for the computation of local heat transfer and skin friction coefficients are usually based on the incompressible boundary layer theory. With Eckert's reference enthalpy concept the incompressible solutions can be applied to high speed flows:

$$h^* = 0.28h_e + 0.5h_w + 0.22h_{aw} \tag{4.7}$$

here h is the enthalpy, subscript e the boundary layer edge, subscript w the wall and aw the adiabatic wall. The latter enthalpy is computed as follows:

$$h_{aw} = h_c + r_f \frac{V_e^2}{2} \tag{4.8}$$

In this equation r_f is the recovery factor which takes into account partial dissipation of the freestream kinetic energy due to viscosity in the boundary layer. The recovery factor is dependent on the state of the flow (laminar or turbulent).

In HOTSOSE approximate methods for the heat flux calculations are present for blunt bodies, such as the reference vehicle Aurora. The heat flux to the stagnation point of a blunt body is given by the following equation, where an equilibrium boundary layer on a spherical nose is assumed.

$$q_w = 0.76 Pr_w^{-0.6} (\rho_e \mu_e)^{0.4} (\rho_w \mu_w)^{0.1} \sqrt{\left(\frac{dV_e}{ds}\right)_s} (h_0 - h_w) \left[1 + (Le^{0.52} - 1)\frac{h_D}{h_0}\right] \tag{4.9}$$

h_D is the dissociation enthalpy. Le is the Lewis number, which is the ratio of thermal diffusivity to mass diffusivity. For this number a value of one is assumed, reducing the term between square brackets in Equation (4.9) to one. The velocity gradient is dependent on the nose radius.

$$\left(\frac{du_e}{ds}\right)_s = \frac{1}{R_N} \sqrt{\frac{2(p_s - p_\infty)}{\rho_s}} \tag{4.10}$$

In the stagnation regions, the regions downstream of the stagnation point, the heat flux is determined by the following equation.

$$q_w = \frac{c_1}{Re^m} \frac{\rho^*}{\rho_e} \left(\frac{\mu^*}{\mu_e}\right)^m \rho_e V_e \frac{h_{aw} - h_w}{Pr_w^k} \tag{4.11}$$

The Reynolds number Re is dependent on the kind of flow. The exact computation of this number is out of the scope of this thesis. Constant c_1 is dependent on the Reynolds number, and differs for laminar and turbulent flow. m is 1 for a laminar flow, its value for a turbulent flow is dependent on the Reynolds number. The constant k has a value of 0.6 for laminar, and 0.4 for turbulent flow.

The skin of the vehicle is cooled by radiation in hypersonic flows at high altitude. Therefore a radiation-adiabatic equilibrium is assumed, as was shown in the previous section in Equation (4.5). With neglection of the background, or sink, temperature the radiative heat transfer rate simplifies to Equation (4.6). By solving these two equations in an iterative manner the radiation adiabatic temperature can be obtained, starting

[2]Private communication, Alexander Kopp, DLR, 23/6/2017

from a constant wall temperature. An adiabatic wall generally has a variable wall temperature, such as is the case for the vehicle surface during hypersonic flight. In the HOTSOSE computations the effect that streamwise wall temperature gradients will have on the heat transfer, and thus radiation adiabatic temperature, is neglected. This assumption is valid when there is a smooth variation in the wall temperature.

4.5. Structural Design

The TPS of a launch vehicle and its structure are closely connected. A hot structure is a structure that takes on both mechanical and thermal loads. In a cold structure the functionality is separated, and the structure is assumed not to take on thermal loads. For Aurora a cold structure is assumed, and the structure is desired to stay within its functional temperatures whiles being affected minimally by the heat load. When the structure is not desired to take a significant amount of the heat load upon itself, the structure will still be affected by the fluctuating temperature. The most relevant considerations regarding the influence of heat loads on the structure will be discussed in this section.

4.5.1. Radiation Equilibrium Temperature

The radiation equilibrium temperature is the upper level temperature that can be reached by the surface of a structure. At the surface of a structure the equilibrium entails that the aerodynamic heat flux equals the heat flux emitted by radiation (Equation (4.12)) [45]. Here q_w is the local heating rate, h the convection coefficient, T_{aw} and T_w represent respectively the adiabatic wall- and wall temperature, σ is the Stefan-Boltzmann constant, ϵ the surface emissivity and T_r finally is the radiation equilibrium temperature. The adiabatic wall temperature is the temperature which is reached when thermal insulation is enforced, thus $q_w = 0$. In the equation it is assumed that all incident aerodynamic heat flux is emitted by radiation, hence no heat flux is conducted into the structure from the TPS. The actual temperature of the surface is likely to be lower as part of the heat transfers into the structure by conduction. The radiation equilibrium temperature is a critical factor for the flight regime of a thermal structural launcher design.

$$q_w = h(T_{aw} - T_r) = \sigma \epsilon T_r^4 \tag{4.12}$$

4.5.2. Thermal expansion

Thermal expansion entails the reaction of a structure on a change, typically an increase, in temperature. When a rod is heated up to a higher temperature than its temperature at rest, it will expand and increase in length. When such a rod is constrained at one end and free at the other, stress in the rod is zero as it is able to expand. The strain ϵ_T is the growth of the rod ΔL divided by the original length L_0 (Equation (4.13)).

When the rod is constrained at both sides, the strain is zero, as the length of the heated rod equals the original length. The stress however is not zero, instead it equals the multiplication of the modulus of elasticity E, the thermal expansion α_T and the temperature difference ΔT (Equation (4.14)).

$$\epsilon_T = \frac{\Delta L}{L_0} \tag{4.13}$$

$$\sigma = E \alpha_T \Delta T \tag{4.14}$$

The situation that is the greatest challenge in thermal structures is caused by a temperature gradient. When a rod is constrained on both sides in one direction, and there is a temperature gradient in the other direction, both the stress and strain resulting are non-zero [20]. The strain is non-zero because the rod is growing in its unconstrained direction. The stress is non-zero because there is a thermal expansion of the material, a temperature differential and a structural constraint of the thermal growth. Thermal stresses are in general harder to process than mechanical stresses, as it is not easily dealt with by adding thickness to the structure. From the thermal analysis performed for the TPS design, presented in Section 5.6 it was found that the temperature over the vehicle surface has large differences as the local heat flux input varies. Especially the wind leading edge reaches a high temperature. The leeward side of the vehicle stays the coolest. An example of the temperature over the vehicle was given for the point in the trajectory where the first heat flux peak is encountered, in Figure 5.13.

4.5.3. Attachments

A big challenge is the attachment of various components of the launcher vehicle, including the TPS, structure, insulation, etc., as they are typically made of different materials and are operating at a large range of temperatures. They can expand and contract with different magnitudes which is the main cause of the challenge. A practical example of this is connection between hot control surfaces and a much cooler actuator, located inside the vehicle [20]. If the control surfaces expend under heat, whilest the actuator stays constant, the connection will be challenged. When isolation materials are used on the TPS panels that are sensitive to permanent compaction, attention must be paid to the deflection of the upper TPS panel. To prevent the compaction from happening the limit deflection value should not be exceeded [16].

4.5.4. TPS panel gaps

Expansion and shrinking of TPS components due to heat can cause gaps in the system. Sneak flow could be a consequence of such gaps, heat then radiates into the gaps between the TPS panels [20]. In the development of the ARMOR TPS a studie was performed to the effect of the gap area to the structural temperature increase [6]. A visualization of the results is shown in Figure 4.2. It was found that the structural temperature increase ratio is nearly proportional to the heat amount that is allowed through the TPS. The two main conclusions that can be drawn from Figure 4.2 are that small gaps are capable to cause large increases in the heat that will reach the structure, and that reduction of the gap emittance is not a satisfying solution to gap radiation. The best solution is to eliminate the panel gaps all together where possible.

In Section 5.6 the different TPS areas were depicted in Figures 5.17 to 5.21. When the actual TPS is applied the division should not be per element, but per area. Gaps will then be likely to arise between the different TPS areas, and individual panels. In the preliminary TPS design, and hence the thesis work, panel gaps are not considered. However, for future application, panel gaps should be taken into account and solutions need to be sought.

Seals

A possible solution for the TPS panel gaps is the use of seals between the gaps. The sealing will prevent heat flows from penetrating the vehicle, and will protect the vehicle from radiation [24]. Especially with a cold structure design it is important that no heat flux leaks into the structure. Flexible seals can be used, or a combination of rigid and flexible seals, as was done in the SHEFEX studies performed by DLR [47]. Manufacturing the rigid seal contours so that they coincide with the panel shape is a very difficult task though, as

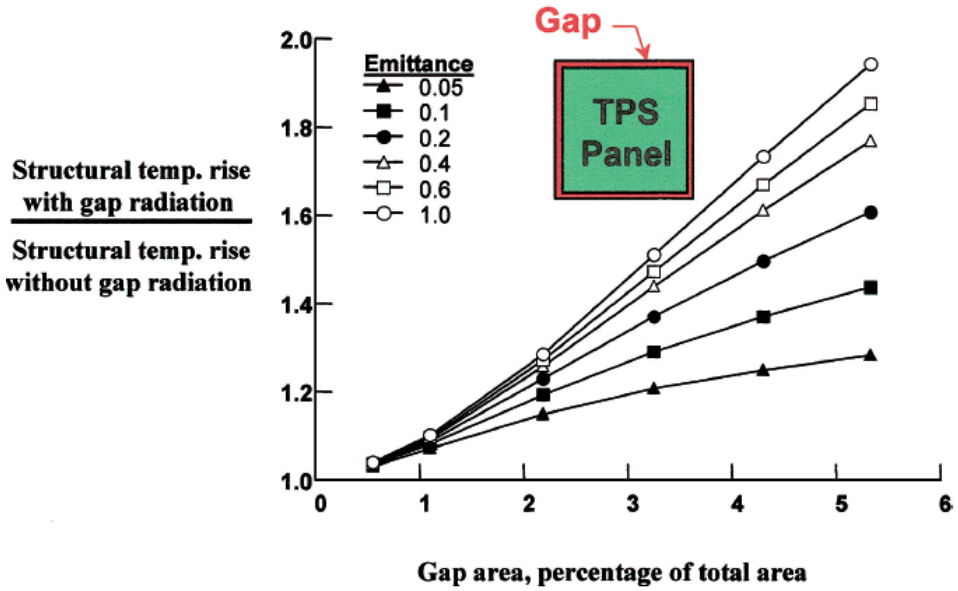

Figure 4.2: Temperature increase of the structure with and without panel gaps ratio as a function of the gap area [6]

a lot of different single parts are necessary to generate the panel shape. A material was developed that has a flexible state during the manufacturing process, but hardens during operation; an oxide ceramic based CMC called WHIPOX.

5

TPS Design & Analysis

An initial TPS design must be made for Aurora before the optimization of the thickness can be performed. This TPS design is based on the heat flux profile that the vehicle is subjected to, which results from the flown trajectory. Based on these heat flux input and the finite element model of the vehicle a thermal analysis can be performed. Section 5.1 provides the considerations and set-up in this analysis. Based on the outcome temperatures over the entire vehicle TPS materials are assigned to different temperature regions. This process is addressed in Section 5.2. The materials used for the different TPS areas are described in Section 5.3. To perform the thermal analysis first a finite element model of Aurora must be made in ANSYS. The choices made in this model, as well as the resulting outcome, are presented in Section 5.4. In Section 5.5 verification of the thermal analysis is performed. The outcome of the TPS design and analysis scheme, in terms of the TPS division over the vehicle, and the experienced temperatures, is presented in Section 5.6. Note that in this outcome the insulation thicknesses are not optimized yet.

5.1. Thermal analysis in ANSYS

The thermal analysis can be performed with as inputs the FEM and heat flux inputs. An elaboration on the FEM is provided later in this chapter, in Section 5.4. The heat fluxes over the vehicles surface are generated by the aerodynamic tool HOTSOSE provided by DLR[1]. An elaboration of the theory behind the HOTSOSE tool is presented in Chapter 4. A number of flight points can be given as an input, to serve as the number of points in time over the reentry trajectory for which the heat flux should be calculated. For each of those flight points the heat flux is determined for every node of the vehicles skin surface. The desired outcome of the analysis is the temperature of the vehicle skin for all layers, as well as the temperature of the vehicles inner structure.

There are two types of thermal analyses that can be performed in ANSYS; a steady-state analysis or a transient analysis. The latter is most suited for the thesis work and is therefore selected. In a steady-state analysis only one point in time is considered and an equilibrium is sought for that point. A transient analysis allows load inputs for multiple time steps, and calculated the output over time. Because multiple flight points (points in time) are considered to evaluate the entire reentry trajectory, a transient analysis is most suitable. Furthermore, this type of analysis allows the heat flux load to transfer through the different layers and thickness of the TPS, as it does in practice. This principle is depicted in Figure 5.1, for a varying heat flux input. It can be seen that the outer layer heats up the fastest, whilest towards the inside of the TPS the layers heat up slower. Also a slight delay in the response can be seen. For example the point between the third and fourth layer, TE4, reaches its maximum temperature later than the outer layer. The point below, TE3, even keeps heating up when the layers above it are cooling down.

For the thermal analysis some boundary conditions are given. As discussed before in Subsection 5.4.1 the radiation nodes have a constant temperature; 4 K for the external and 293 K for the internal radiation. A uniform starting temperature is provided for all nodes, of 293 K. Furthermore the heat flux load is provided for

[1] Private communication, Alexander Kopp, DLR, 3/8/2016

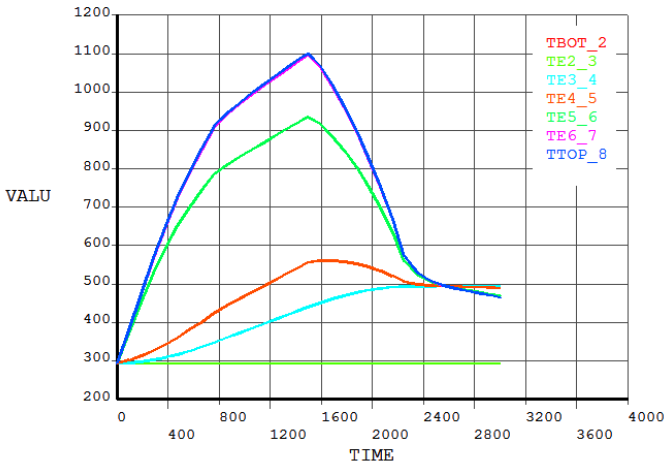

Figure 5.1: Temperature variation over time for the layers of an arbitrary TPS node

each pre-determined flight point. Between the provided input load the heat flux is considered to be ramped. Thus going linearly from the heat flux value at one point in time, to the given value at the next point in time.

5.2. TPS Division over Vehicle

Based on the outcome temperatures over the vehicle surface of the first performed thermal analysis, the TPS area division over the vehicle is performed. In this first thermal analysis the vehicle is assumed to have only one TPS, FRSI, with an insulation thickness of 1.0 cm. More information on the considered TPS materials is given in the next section. The analysis is performed with the sole purpose of assigning the right TPS to each element of the vehicles skin. The maximum temperatures reached at the skin top layer are evaluated for each element. Based on that temperature it is decided which TPS will be assigned. For the assignment the maximum reusable temperatures of the TPS areas are considered, previously stated in Table 5.3. To account for the discrepancy in experienced temperature, caused by the fact that the temperature is considered for each element for FRSI with a very low insulation thickness, a factor of 0.9 is used on the maximum reusable temperature for the assigning of the TPS materials on the elements. This factor was determined on a trial an error base, where the results of the thermal analysis after the TPS application were checked for different division factors. The temperature ranges that are selected for the different TPS areas are stated in Table 5.1. Note that for the highest temperature TPS CMC the original re-usability temperature is taken as the limit. The results of the TPS division can be found in Section 5.6.

The TPS division as is makes it possible for every element to have a different TPS assigned to it. In reality TPS areas consist of larger, consistently shaped areas. It is not implementable to apply different TPS materials to very small areas. As the tool resulting from the thesis work is designed to make a rough preliminary TPS design, this discrepancy was not taken into account. However, when the TPS design is required to be applicable in real life it must be adapted to assign different TPS materials to areas of the vehicle, and not elements.

Table 5.1: Temperature Range per TPS for TPS assignment to elements

TPS	Temperature range top layer [K]
FRSI	0 – 579.6
AFRSI	579.6 – 829.8
TABI	829.8 – 1260.0
AETB TUFI	1260.0 – 1440.0
CMC	1440.0 – 1850.0

5.3. TPS and Materials

In the TPS optimization scheme the vehicles surface is divided into different areas, depending on the temperatures that are reached in those areas. The different temperature areas are all assigned a passive TPS, for which the materials out of which it consists varies. These material combinations determine the temperature range for which the TPS is reusable. All combinations consists at least of a coating, an insulation layer and the structural layer underneath. A database has been constructed in the thesis work, consisting of five different material combinations. These combinations and their individual materials will be shortly discussed here. The same passive TPS combinations are taken that are used in the 1D TPS design tool of DLR; Thermal protection system Optimization Program Version 2 (TOP2) [18]. Their properties were provided by DLR, and are given in Appendix E. It was chosen to use the same TPS materials as this enables the possibility to compare the results from the three dimensional (3D) analysis made in the thesis work, and the results from the 1D TOP2 tool. Results of this comparison are given and discussed in Chapter 8. Obviously more TPS areas/materials can be added to the database if desired, for a more elaborate TPS selection.

The combinations are Alumina Enhanced Thermal Barrier (AETB) Toughened Uni-Piece Fibrous Insulation (TUFI), Advanced Flexible Reusable Surface Insulation (AFRSI), CMC, Flexible Reusable Surface Insulation (FRSI) and Tailorable Advanced Blanket Insulation (TABI). Each combinations consist of a multitude of layers. The materials used for the layers of each combination are given in Table 5.2, where also for each combination the insulation layer that is to be optimized is identified. The values given for the insulation thicknesses in the table are just general values, in the thesis work tool this layer will be optimized and can thus result in a different value. The bottom layer always represents the structural material that embodies the primary structure, aluminum. A visualization of one of the combinations, TABI, is given as an example in Figure 5.2. Some general properties of the combinations, including the maximum temperature for which they are still reusable, can be found in Table 5.3. Furthermore the mass equation is provided, dependent on the Area A that is covered and the insulation layer thickness t_{il}.

As mentioned before, the TPS is modeled in ANSYS using shell elements. The heat transfer in ANSYS occurs between layers of different elements that have the same layer number. Thus conduction happens between the top layers, the second layers, the bottom layers, and so on, as depicted in Figure 5.3, independent of the relative thicknesses of the layers. The heat conduction between the TPS and the elements of the inner structural members works in the same manner. This causes some discrepancies in the heat conduction, as not all layers of the different TPS material combinations have the same thickness, nor do all insulation layers are placed in the same layer number. Also errors appear in the interaction with the structural members, which only consist out of one layer aluminum. When a six-layered TPS element is connected to an element of the inner structure, all TPS layers of that element will conduct heat to the structural element. It is desired that only the bottom layer conducts heat to the structural member, as in practice only this layer is actually in connection with the structure.

These discrepancies are mostly solved by the use of dummy-layers. To better the interaction between TPS

[2]Private communication, Alexander Kopp, DLR, 27/7/2016
[3]Private communication, Alexander Kopp, DLR, 27/7/2016

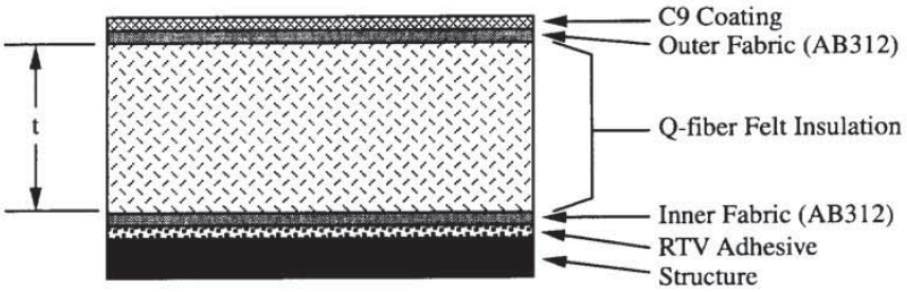

Figure 5.2: Visualization of the material layers of TABI [34]

Table 5.2: Material layers of the selected passive TPS material combinations [2]

TPS	Layer	Thickness [mm]	Optimization insulation layer
FRSI	DC 92 Coating	0.254	
	AB 312	0.279	
	FRSI	50.0	✓
	AB 312	0.229	
	RTV Adhesive	0.203	
	Aluminium	20.0	
AFRSI	C9 Coating	0.254	
	AB 312	0.279	
	AFRSI	60.0	✓
	AB 312	0.229	
	RTV Adhesive	0.203	
	Aluminium	20.0	
TABI	C9 Coating	0.254	
	AB 312	0.229	
	Q-fiber Felt Insulation	51.0	✓
	AB 312	0.229	
	RTV Adhesive	0.229	
	Aluminium	20.0	
AETB TUFI	TUFI Coating	0.254	
	AETB-8	100	✓
	RTV Adhesive	0.203	
	Nomex Felt	0.203	
	RTV Adhesive	0.208	
	Aluminium	5.0	
CMC	CMC	6.0	
	ZIRCAR Alumina Material	150	✓
	Aluminium	20.0	

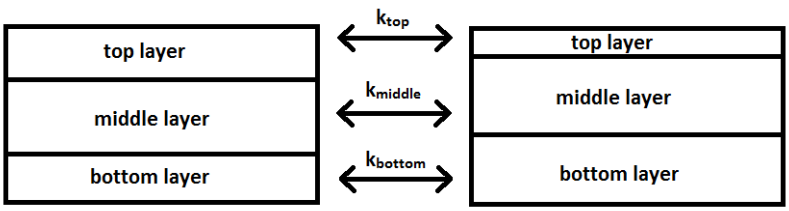

Figure 5.3: Conduction takes place between layers of the same layer number

elements it was desired to have the top, bottom and insulation layers connected. A dummy material was created with a very high conductivity and very low heat capacity, so the heat can transfer easily through the dummy-layer. With the dummy-layers all elements consist out of seven layers. The implementation of the dummy layers for the different TPS material combinations is shown in Table 5.4. With the dummy layers in place throughout the TPS design the coating layers are connected, as well as the insulation layers and the structural skin layers. Therefore it is ensured that conduction takes place between those respective layers.

For the interaction between the TPS and structural members a different dummy material was created with a very low conductivity and heat capacity. While for the interaction between TPS elements the dummy layer has properties to ensure easy conduction, the dummy layer of the inner structural elements functions to withhold conduction. The structural shell element was also given seven layers, of which the first six layers consist of the dummy material. This insures that practically no heat transfer takes place between the upper layers of the TPS and the structure. The actual properties of the dummy materials are given in Appendix E. It must be noted that even with the application of the dummy layers there will still be discrepancies in the heat conduction, due to the difference in material thickness, as mentioned previously. However, it is assumed that

Table 5.3: General properties of the selected passive TPS material combinations [3]

TPS	Maximum Reusable Temperature [K]	Mass[kg]
FRSI	644	$(57.25 + 96.11 \cdot t_{il}) \cdot A_{TPS}$
AFRSI	922	$(57.36 + 96.11 \cdot t_{il}) \cdot A_{TPS}$
TABI	1400	$(57.35 + 96.11 \cdot t_{il}) \cdot A_{TPS}$
AETB TUFI	1600	$(56.89 + 128.15 \cdot t_{il}) \cdot A_{TPS}$
CMC	1850	$(67.46 + 35 \cdot t_{il}) \cdot A_{TPS}$

Table 5.4: Dummy layer application

Layer #	FRSI	AFRSI	TABI	AETB TUFI	CMC
1	Coating DC 92	Coating C9	Coating C9	Coating TUFI	CMC
2	AB 312	AB 312	AB 312	**Dummy layer**	**Dummy layer**
3	Insulation FRSI	Insulation AFRSI	Insulation Q-fiber felt	Insulation AETB-8	Insulation ZIRCAR
4	**Dummy layer**	**Dummy layer**	**Dummy layer**	RTV adhesive	**Dummy layer**
5	AB 312	AB 312	AB 312	Nomex felt	**Dummy layer**
6	RTV adhesive	RTV adhesive	RTV adhesive	RTV adhesive	**Dummy layer**
7	Aluminium	Aluminium	Aluminium	Aluminium	Aluminium

the effects are sufficiently small not to have a large impact on the solution.

5.4. Finite Element Model

The finite element model is made in ANSYS. An initial model of the vehicle consisting of lines and areas is provided by DLR[4]. The vehicle model is a preliminary design of Aurora and contains five main parts;

- Wing ribs
- Wing spars
- Wing skins
- Fuselage frames
- Fuselage skins

In the generation of a finite element model there are many options available. For the thesis work the model is designed to be most appropriate to perform a thermal analysis on the winged space plane. In this section the choices made in the design of the model with regard to the element type and meshing are stated and reasoned.

5.4.1. Element Types

The elements appropriate for a thermal analysis, that are available in ANSYS, are numerous [1]. As it is desired to do a 3D analysis in the thesis work, this limits the options. Keeping in mind the geometry of the TPS, the two main element choices are either to use 3D solid elements, or shell elements. Shell elements are applicable for geometries where one of the three dimensions is significantly thinner, as is the case for the TPS. Solid 3D elements are generally preferred for thick structures in 3D space that have neither a constant cross section nor an axis of symmetry.

For the thesis work it is decided to use shell elements. They have several advantages compared to solid 3D elements for the application desired in the thesis work. As shell elements are modeled as two dimensional (2D) areas with a thickness in the third dimension, the meshing can be performed in 2D. This decreases the computation time and power. Also using shell elements reduces the implementation time and effort. The TPS that is to be modeled by the elements consists of several layers with different materials (see Section 5.3). Within the shell elements different layers with individual thicknesses can be specified, which is convenient in the application of different TPS materials. The largest advantage comes from the fact that in the optimization tool the thickness of one of the TPS layers is adjusted for every new thermal analysis. With shell elements this

[4]Private communication, Alexander Kopp, DLR, 8/8/2016

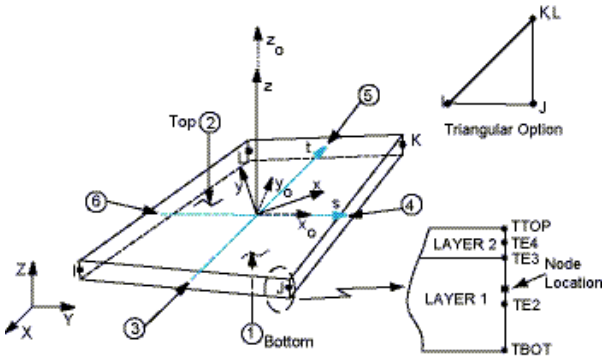

Figure 5.4: SHELL131 element [2]

is easily adaptable, without having to adapt the finite element model of the vehicle.

The specific shell element that is chosen is SHELL131, a depiction of the element is given in Figure 5.4. It is a layered element with thermal conductive capabilities both in-plane and through the thickness [2]. The element is applicable to a transient thermal analysis, which is the analysis performed in the thesis work. The elements have 4 nodes, and the degrees of freedom are multiple temperatures at each node, for each layer edge [1].

Radiation space nodes
The vehicle will lose heat by radiation. Heat will radiate from the outside of the vehicle skin to deep space, and on the inside of the skin towards the spacecraft interior. To account for radiation two radiation space nodes are created. The first is the node representing the deep space environment the vehicle will be radiating to. The second space node represent the interior of the spacecraft, thus all subsystems that will be present inside the vehicle. These subsystems are not taken into account in the vehicle model, as the preliminary model solely exists out of the skin and main structure. For the radiation nodes the ANSYS element SURF152 is used. This element enables radiation between the surface of the skin and the extra (radiation) node. Within the element it can be indicated that one extra node will be generated, valid for the radiation calculations. Furthermore it is specified that radiation will be used with the form factor real constant. The radiation form factor is the proportion of the radiation which leaves one surface that strikes another, in a radiative heat transfer. This is also known as the view factor [10].

The coordinates of the external radiation node are arbitrary, and thus can be randomly selected outside the vehicle. The second node representing the interior is placed roughly in the middle of the vehicle. Both nodes are given an emissivity of 0.85 and thus are assumed to be effective in the emitting of energy as thermal radiation, comparable to, e.g., iron oxide and glazed silica [5].

For the form factor both nodes are assumed to have the value 1.0. Hence it is assumed that the radiation from both the deep space environment and the spacecraft subsystems are completely touching the vehicle. As no other objects are considered in the analysis this is valid. Both nodes are given a temperature constraint as boundary condition. For the environment the temperature is assumed to equal the temperature of deep space; 4 K. In this assumption it is not considered that the vehicle faces anything other than a space background. For a higher precision a changing view factor should be taken into account, as during re-entry flight a larger and larger portion of the Earth will be in view of the spacecraft. However, for the analysis at hand the deep space assumption is sufficient. To verify the deep space assumption the minimum and maximum temperatures the vehicle skin reaches are compared for the two extreme possibilities the view factor and its temperature can have; 4 K when the vehicle faces solely deep space, and 293 K when the spacecraft has landed on Earth, thus only Earth is in sight. The results are given in Table 5.5, for an arbitrary vehicle configuration. One can see that especially the difference in percentage for the maximum experienced temperature is small and thus can be neglected. For the minimum experienced temperature the difference is larger, however it is still assumed sufficiently low to be neglected.

[5] http://www.optotherm.com/emiss-table.htm, visited on 31/08/2016

Table 5.5: Temperature ranges for different external environment temperatures

External node temperature [K]	Minimum vehicle temperature [K]	Maximum vehicle temperature [K]
4	334.1	828.8
293	354.2	830.4
Percentage difference [%]	6.0	0.2

The temperature assumed for the vehicle interior is room temperature, hence 293 K. Here, the assumption is made that most subsystems function at or around room temperature. In practice there may be a slight variation in the operational temperatures of the subsystems, however this is assumed to be small enough for the assumption of room temperature in the vehicles interior to be valid.

5.4.2. Meshing Options

The meshing of the vehicle model into elements and nodes is to be performed after the element types have been assigned to the models. Two types of meshing are possible; free or mapped meshing. It was chosen to apply a free mesh, as it is easier to apply on a multitude of geometries and creates a mesh faster. Also the need for manual adaption of the mesh is kept to a minimum. The downside of a free mesh is that there is less control over the quality of the mesh. Especially in the critical regions of the geometry the mesh should be visually inspected. The critical regions are defined to be the regions that endure the largest heat flux during flight, which are typically the leading edges of the wing and the nose region.

As shell elements are used, meshing is done in 2D. There are two 2D shapes available for the elements; quadrilaterals and triangles. A small study was performed to find which element type leads to better results, both for the wing and fuselage skin. Meshings were performed with both element shapes for different element sizes. From these meshings warnings and potential errors arose. Furthermore, the meshings were visually inspected on consistancy and shape. Based on the number of potential errors and warnings given for the different shapes, and the visual inspection, a conclusion could be drawn for both the wing and fuselage. The wing mesh is found to be best with a triangular mesh, the fuselage with a free quadrilateral mesh. A depiction of the skin mesh, where the triangular elements of the wing skin and the quadrilateral elements of the fuselage skin are visible, is given in Figure 5.5. The structural elements are all meshed in quadrilateral-shaped elements, as this leads to a higher accuracy for elements with no mid-side node [2], which is the case for the structural elements as they consist of only one functional layer. The structure mesh is shown in Figure 5.6.

Meshing regions

The fuselage nose and wing leading edge are the critical regions of the vehicle when it comes to temperatures, as these regions endure the highest aerodynamic heat load. As these regions are more sensitive a denser mesh

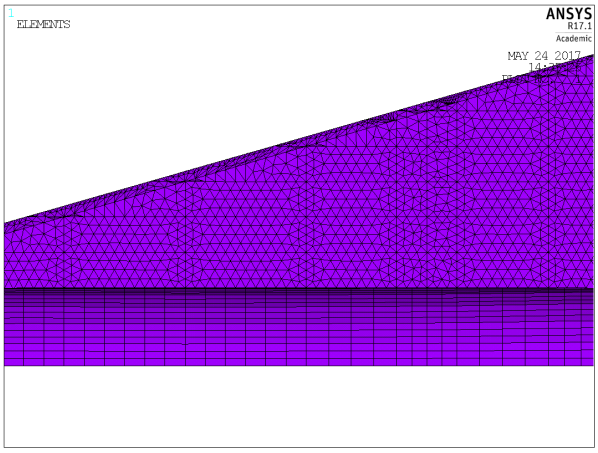

Figure 5.5: Quadrilaterial meshing of the fuselage skin, and triangular meshing of the wing skin of Aurora

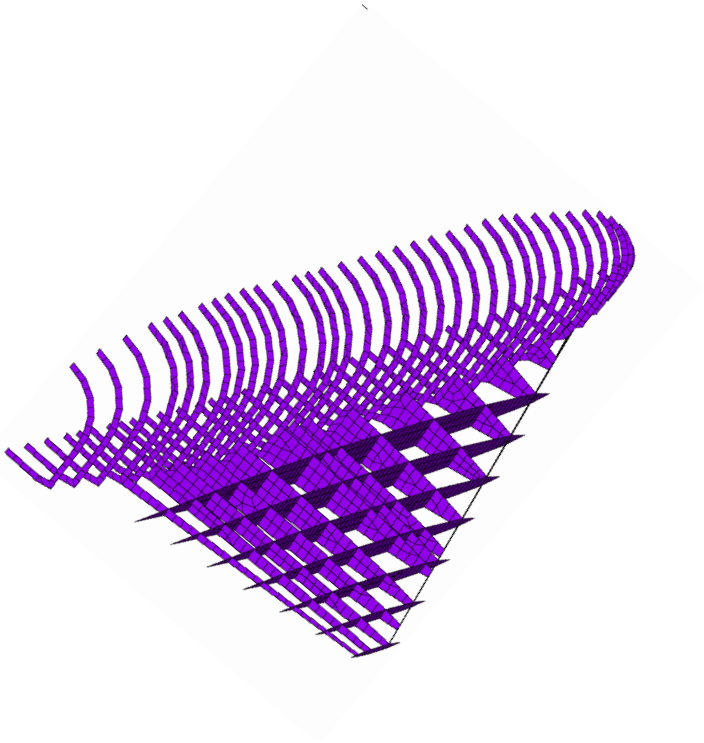

Figure 5.6: Quadrilaterial meshing of the structure of Aurora

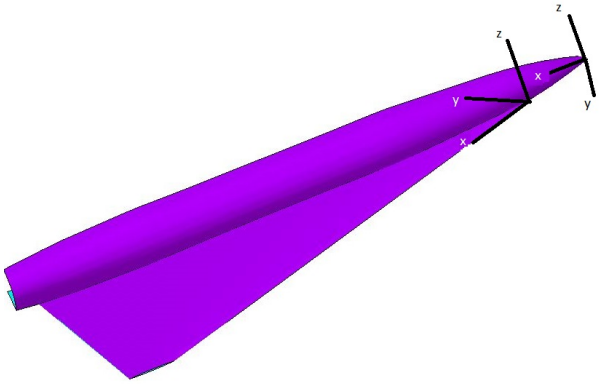

Figure 5.7: Aurora with the two coordinates systems used for the meshing

is desired here. A coarser mesh can be applied to the rest of the vehicle, as the temperature sensitivity is lower, and the application of a coarser mesh takes less time. It was chosen to divide both the fuselage and the wing in two regions for the meshing. The regions of the fuselage are defined by the x-axis of the Cartesian coordinate system, shown at the nose of the vehicle in Figure 5.7. For the wing a new coordinate system was defined, with its x-axis parallel to the wing leading edge, and the y-axis perpendicular to it in the wing skin plane. The z-axis points upwards, similar to the z-axis of the Cartesian system. The new system is shown in Figure 5.7 at the root of the wing. Table 5.6 shows the different regions and their element size. Also, for the percentages representing the mesh regions, the used coordinate systems and the axis over which the percentages are taken are specified.

5.4.3. Resulting Finite Element Model

The FEM resulting from the design choices discussed in the previous section is shown in Figure 5.8. The internal structural members consists of a total of 2416 elements. The vehicle skin is divided into 13386 elements. All skin elements also have two surface radiation elements; one to represent radiation to outer space and one

Table 5.6: Meshing regions

Vehicle part	Mesh region	Element size [m]	Coordinate system
Wing	0 - 10%	0.1	Local y-axis
	10 - 100%	0.4	Local y-axis
Fuselage	0 - 2.5%	0.05	Cartesian x-axis
	2.5 - 100%	1.0	Cartesian x-axis

to represent radiation to the inner subsystems. This leaves the FEM with a total of 42574 elements. For more

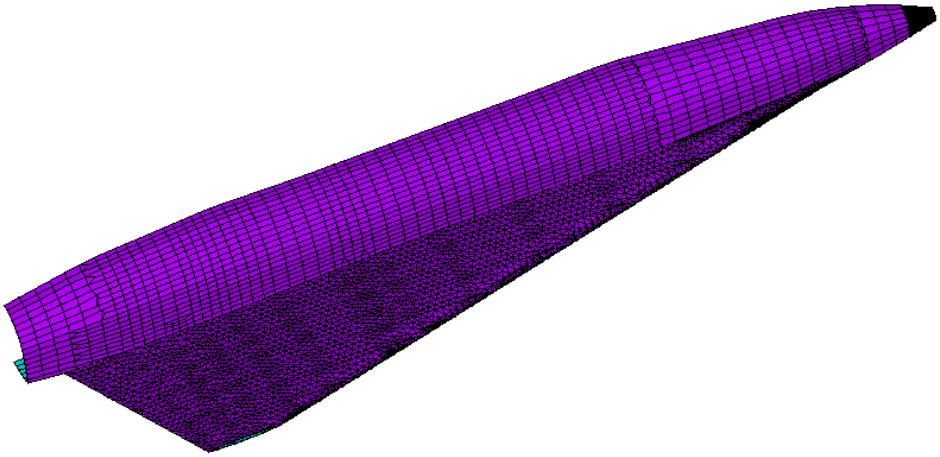

Figure 5.8: FEM of Aurora, consisting of the fuselage and wing

visualizations of the Aurora Fem the reader is referred to Appendix D.

5.5. Verification TPS Design & Analysis

The TPS design and thermal analysis performed in ANSYS must be verified, to ensure the model and tool can be used to optimize the insulation thickness, as is desired in the thesis work. The verification is focused on the multi-layered shell elements, and the transient analysis. These will be discussed in the following subsections.

5.5.1. Verification Multi-layered Shell Elements

The verification of the use of multi-layered shell elements is done with a steady state thermal analysis. For the verification not the entire vehicle model was considered, to decrease the computation time. A small area of the wing skin was considered, consisting of 66 elements. The wing skin areas are shown in Figure 5.9, where the blue area is the one chosen for the verification. The sample shell elements consist of three layers; a coating, the main insulation layer and the aluminum structural layer. The heat flux the small sample is subjected to has a constant value of 30 kW/m^2. The nodes all have an initial temperature of 293 K. Some qualitative analyses were performed on this model.

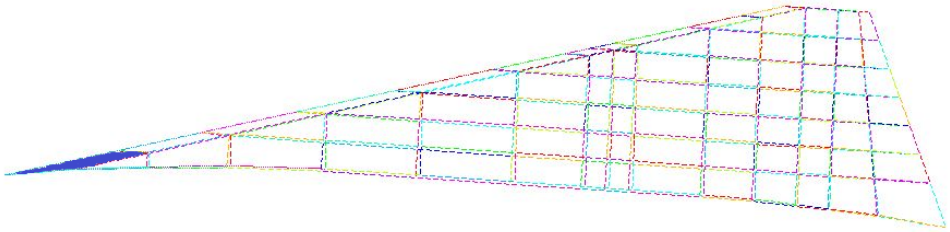

Figure 5.9: Depiction of the wing area used as a small sample for verification

Table 5.7: Temperature ranges for different skin thicknesses

Insulation layer thickness [cm]	Maximum temperature bottom layer [K]	Maximum temperature top layer [K]
1	459.0	875.8
5	357.0	885.3
10	330.7	886.7
20	313.9	887.4
50	302.0	887.9
100	297.6	888.1

Variation of thickness
To ensure the correct effect of a variation in thickness, the thickness of the materials insulation layer is varied from 1.0 to 100 cm. The results are listed in Table 5.7, showing the maximum temperature experienced by the bottom (aluminum) and top (coating) layer. The maximum temperature the top can reach can be calculated with the radiation equilibrium temperature, which is introduced in Chapter 4, Equation (4.12). In this equation it is assumed that all heat flux is emitted by radiation, and thus none by conduction. For the heat flux input of 30 kW/m^2 and an emissivity of the top layer of 0.85, the radiation equilibrium temperature is 888.4 K. From Table 5.7 it can be seen that the top layer indeed stays below, but close to, this temperature. With an increase of thickness the temperature of the top layer slightly increases, while the temperature of the bottom layer reaches significantly lower temperatures. Thus for an increase in the thickness, less heat flux is transferred by conduction. This is in line with the conduction heat flux equation, Equation 4.2, also given in Chapter 4. With an increase in thickness the conduction heat flux decreases. Furthermore, a thicker insulation layer changes the value of the thermal conductivity of the material. This value will decrease, also leading to a decrease in the conductive heat flux. This behavior is clearly visible from the verification Table. A small similar study was also performed taking the entire vehicle into account, to make sure no different behavior is present in a more complicated model. Similar results were found, ensuring that for the complete vehicle the multi-layered shell elements also work as expected.

Variation of TPS areas
The various TPS areas and their respective materials (presented in Section 5.3) have also been analyzed. All were applied to the small sample area depicted in Figure 5.9. The insulation layer was kept at a constant thickness of 5 cm for all TPS areas. It was verified that the TPS areas were functioning for their respective reusable temperature regions. The maximum experienced temperatures by the top layer and structural bottom layer were investigated by a sanity check. The radiation equilibrium temperature was calculated to ensure that the top layer temperature did not exceed the maximum possible temperature. Furthermore, the conductivity of higher temperature TPS areas is typically decreasing, and hence results in less heat transfer to the bottom layer by conduction. So for higher temperature TPS areas the structural layer will reach lower temperatures. An equal analysis has been performed taking into account the entire vehicle, leading to similar satisfying results.

5.5.2. Verification Transient Analysis

In a transient analysis the heat flux input can be given at multiple time steps. To ensure the right implementation of the transient analysis in ANSYS multiple input variations were analyzed. Here for the small skin sample was used, previously described in Subsection 5.5.1. Three load steps were considered, the first with an end time of 10 s, the second 20 s, and the third 40 s. As previously discussed in Section 5.1, ramped loading was enforced. As before the starting temperature of all nodes is 293 K, and radiation occurs to a node representing deep space, with an enforced constant temperature of 4 K, and a node representing the internal environment, with an enforced constant temperature of 293 K. A heat flux of 10 kW/m^2 was applied in the first load step, and kept constant in the following load steps. The applied heat fluxes are constant for all skin elements, as a result the temperature over the object is almost equal at every point, and can thus be considered constant (differences are in the tenths of K). Results of the reference case bottom and top temperature are shown in Figure 5.10, for node 20, which is located in the middle of the plate. As the load is ramped it will increase from 0 to 10000 in the first load step, from where it remains constant. This can be seen in the temperature increase of the top layer. As the heat will partly transfer over time to the bottom layer due to the

TPS, one can see that the increase in temperature of the bottom layer is much less steep, as was expected.

After analyzing the response to an increasing and constant heat flux, the effects of decreasing the heat flux was analyzed. Here the heat load of 10 kW/m^2 was again applied in the first time step, but the load was deleted in the second time step. Results for the bottom and top layer are given in Figure 5.11. When the heat load is deleted the temperature is decreasing in an almost linear fashion for the top layer, whereas the bottom layer temperature is still increasing. This makes sense as the top layer is still transferring heat to the bottom layer, warming it up. In studies performed for the Space Shuttle and Japanese HOPE this behavior was also found, where certain parts of the TPS keep heating up even after landing [44] [3].

Finally it was investigated what happens when the heat load is not deleted but decreased. In this test the heat load was set from 10 kW/m^2 to 1 kW/m^2 in the second time step. Figure 5.12 shows the proper working of a decreased heat load, as the temperature increase of the top layer becomes less steep when the load decreases. One can see the working of the ramped load, as in the second time step the temperature increase, and thus heat flux increase, happens gradually.

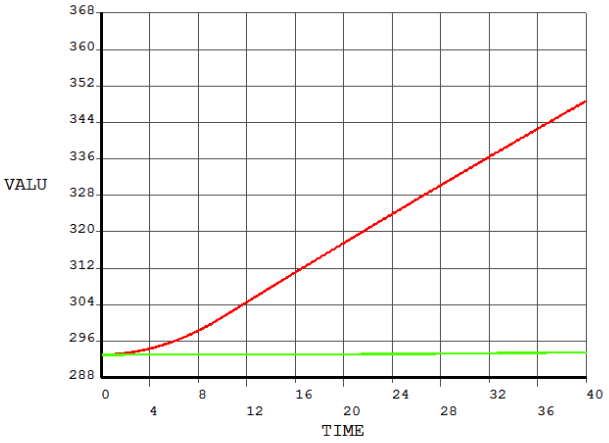

Figure 5.10: Temperature of the bottom and top layer, the green and red line respectively, of the reference case for the transient thermal analysis

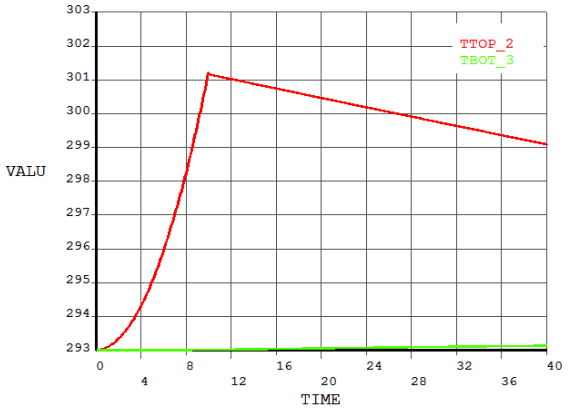

Figure 5.11: Temperature of the bottom and top layer, the green and red line respectively, where the heat load was deleted in the second time step for the transient thermal analysis

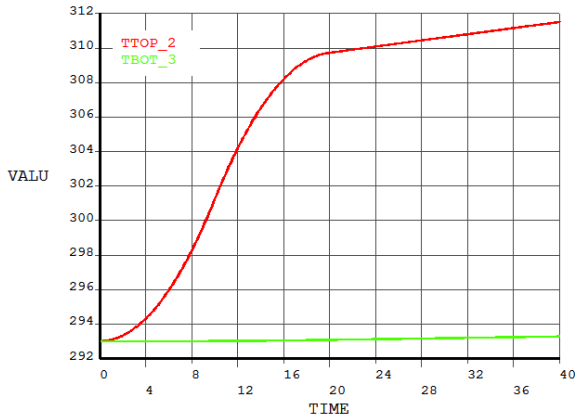

Figure 5.12: Temperature of the bottom and top layer, the green and red line respectively, where the heat load is decreased to 1000 W/m^2 in the second timestep, for the transient thermal analysis

5.6. Baseline TPS Design

In this section the results from the described thermal analysis and its resulting TPS division over the vehicle surface will be described. In the thermal analysis all experienced maximum temperatures of the skin top layers are within the ranges of the re-usability of the TPS areas, thus all elements are assigned a passive TPS material combination. The temperature over the skin of the vehicle for four different points over the trajectory is visualized in Figures 5.13 to 5.16. The time points are chosen as they have the most interesting heat flux input, with a maximum at the first and third, a minimum at the second time, and the last time at 3000 s is at the end of the analyzed trajectory. It is found that the highest temperatures are reached at the wing leading edge. Furthermore the windward side of the vehicle gets significantly hotter than the leeward side, as expected. Over the fuselage the temperature is about 850 K on the windward side, up to 1000 K towards the nose. On the leeward side the majority of the fuselage does not exceed 600 K, except for a small area of the nose which does heat up to about 900 K. The largest area of the wing surface on the windward side reached a temperature of about 1000 K. This value increases towards the leading edge, where the maximum value of about 1700 K is reached. This temperature is also experienced on the wing leading edge of the leeward side. However, the majority of the leeward wing surface stays below 400 K. At the first maximum, at 428.6s, depicted in Figure 5.13, it can be seen that the maximum temperature area of the wing leading edge covers a relatively large part of the wing, compared to the other figures where only the actual edge of the wing leading edge reached the highest temperature. The difference is due to the angle of attack under which the vehicle flies. It has a large value at the start of the flight, 65°, and gradually decreases to a constant value of 20° is reached at 1400 s. At 428.6 s the angle of attack is just below its maximum. At the local minimum of the heat flux at 979.6 s the maximum temperature decreases with about 300 K from the previous maximum, as can be seen in Figure 5.14. However, the minimum temperature of the vehicle surface increases. This is due to conduction from adjacent elements. The starting temperature for all nodes is given as 293 K, thus conduction from underlying elements and layers that have not radiated their heat away will also lead to a temperature increase, when the surface element temperature is below 293 K. At 1408.2 s the maximum temperature of the vehicle over the trajectory is reached, as shown in Figure 5.15. At the final analyzed flight point the vehicles temperature has significantly decreases due to the decrease in heat flux (Figure 5.16). The temperature over the vehicle becomes more uniform, as an equilibrium is sought through conduction when the heat flux input is zero. Heat is radiated away to the external radiation node, representation radiation into space, during the flight. Radiation towards the internal subsystems has less effect, as their temperature is assumed to be 293 K, which is also the assumed starting temperature of the elements.

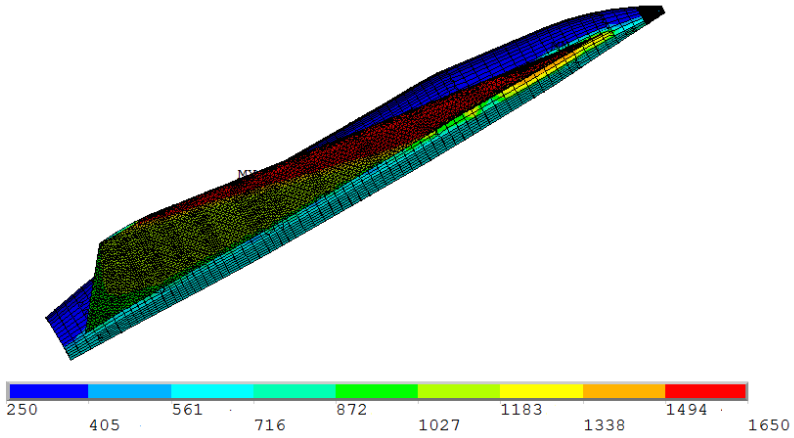

Figure 5.13: Temperature over the surface of the vehicle at 428.6 s

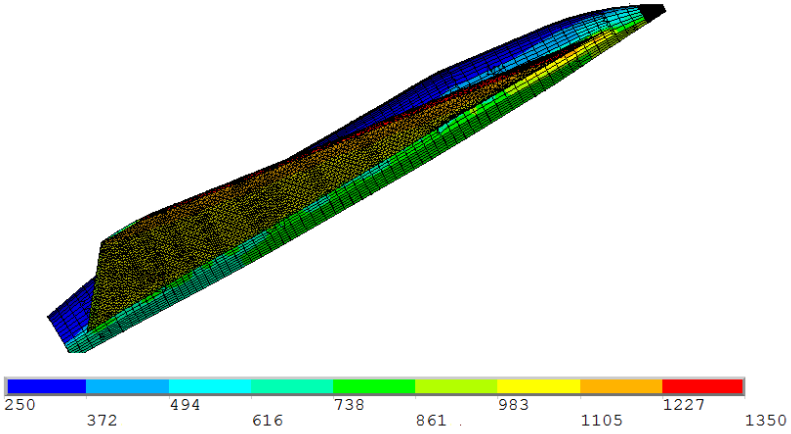

Figure 5.14: Temperature over the surface of the vehicle at 979.6 s

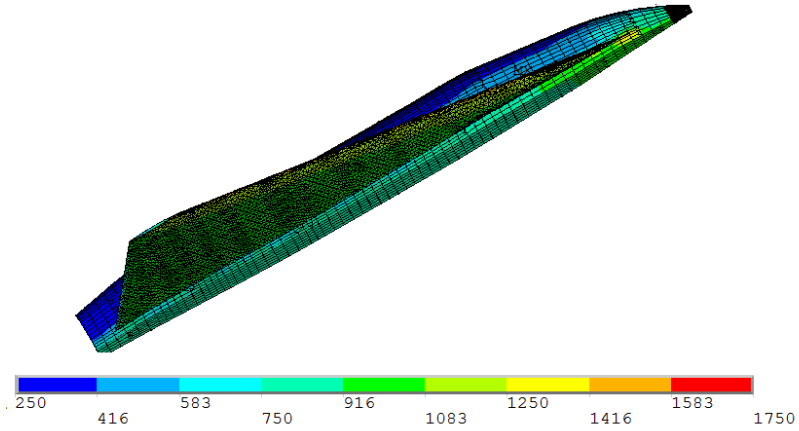

Figure 5.15: Temperature over the surface of the vehicle at 1408.2 s

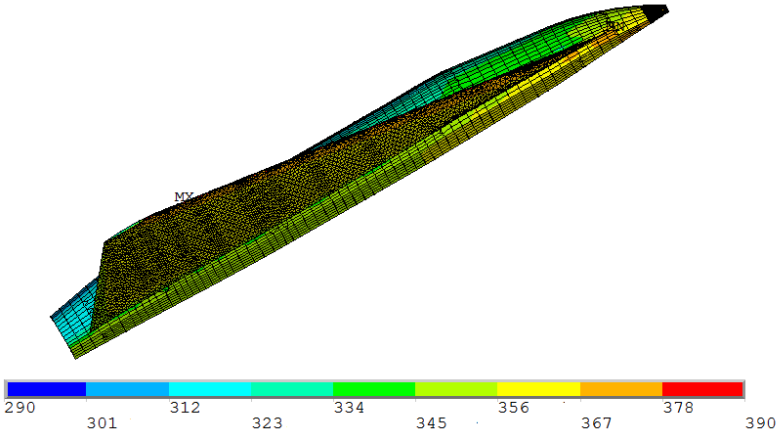

Figure 5.16: Temperature over the surface of the vehicle at 3000 s

The division between the different TPS areas is shown in Table 5.8, with the number of elements per TPS area, the node which experiences the highest top layer temperature, the highest top layer temperature and highest bottom layer temperature reached. As expected FRSI has the largest amount of elements. This is expected because the top side of the vehicle will endure much lower heat fluxes, as it is the leeward side and thus the friction with the atmosphere is a lot lower than for the windward side. As a result the experienced temperatures stay lower. The division of the elements into the different TPS areas is visually shown in Figures 5.17 to 5.21. The purple colored elements are elements of the leeward side, and the blue elements of the windward side. In Figure 5.17 it can be seen that the majority of the leeward side of the fuselage and wing is covered by FRSI. Towards the leading edge of the wing, the end of the wing, and the nose region, hotter temperatures are experienced and the elements are given AFRSI (Figure 5.18). Also the aft side of the fuselage on the windward side stays relatively cold and is assigned AFRSI. The front side of the windward fuselage section gets hotter, and is given TABI, as shown in Figure 5.19. Also the backside of the windward wing stays in this temperature region. The leading edge of the wing on the leeward side has very thin temperature areas. A thin line can also be seen in the TABI region. An even thinner line is also covered with AETB TUFI (Figure 5.20). Furthermore, a line roughly located in the middle of the wing on the windward side shows a division in the temperatures that are reached over the wing, and is given AETB TUFI. Also the connection between the wing and fuselage on the windward side can achieve high temperatures, which makes AETB TUFI the appropriate TPS area. The hottest areas of the vehicle is the outer wing leading edge on the leeward side, and a thicker leading edge on the windward side of the wing. This highest temperature region is assigned CMC.

Table 5.8: Results TPS area division

TPS area	Number of elements	Critical node	Maximum temperature top layer [K]	Maximum temperature bottom layer [K]
FRSI	4212	772	579.0	379.1
AFRSI	1161	8680	829.8	379.1
TABI	4092	5213	1258.5	379.0
AETB TUFI	405	1439	1438.9	379.1
CMC	3516	1787	1786.5	379.1

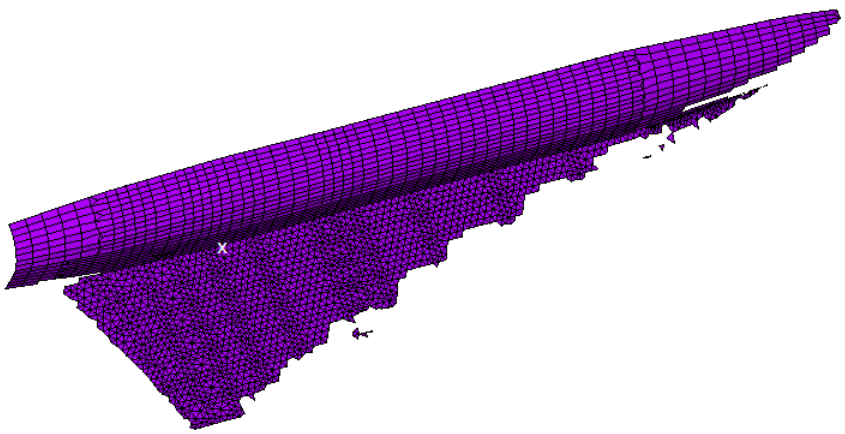

Figure 5.17: Elements that are assigned TPS area FRSI

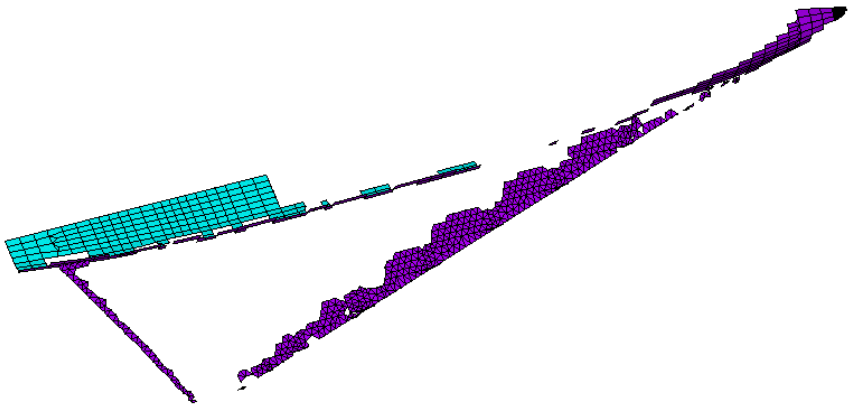

Figure 5.18: Elements that are assigned TPS area AFRSI

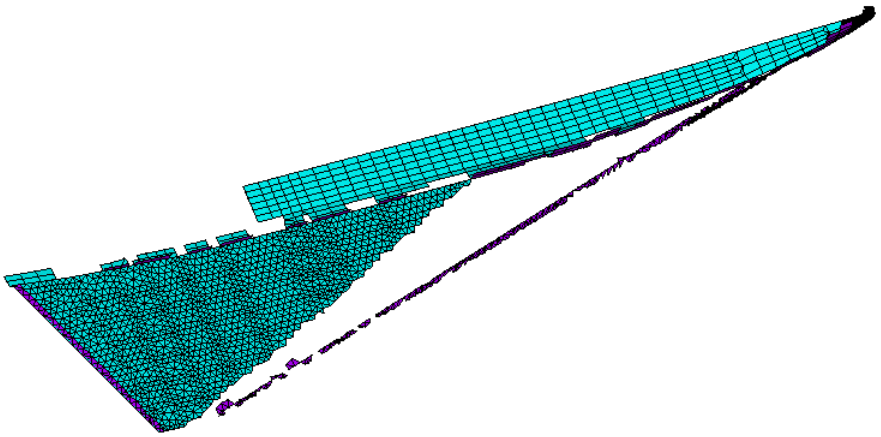

Figure 5.19: Elements that are assigned TPS area TABI

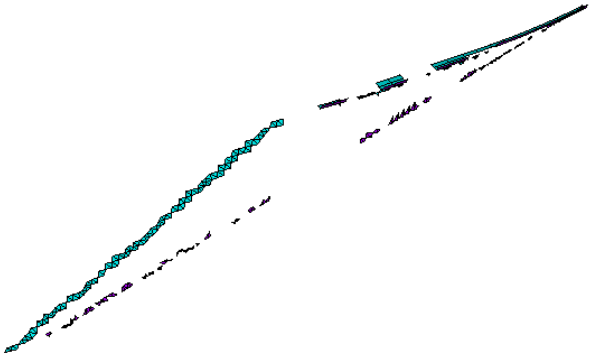

Figure 5.20: Elements that are assigned TPS area AETB TUFI

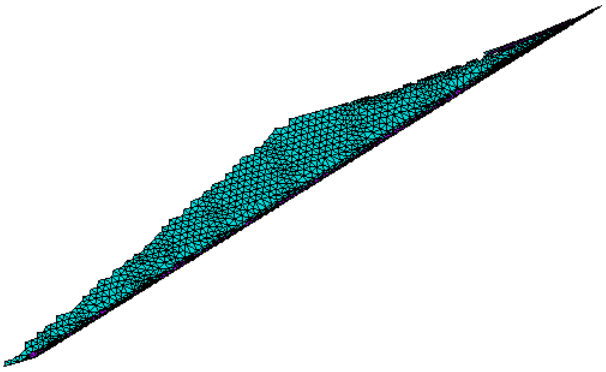

Figure 5.21: Elements that are assigned TPS area CMC

The critical node per TPS area embodies the node that experiences the highest top layer temperature. For each TPS area the layer temperatures of the critical node are plotted over time. Also the heat flux values are shown over time. These results are shown in Figures 5.22 to 5.26. As a 3D thermal analysis is performed, the temperature response of the nodes is not only dependent on the input heat flux, but also on the thermal load of the neighboring elements. Overall it can be seen that the temperatures reached by the top layer, indicated by TTOP, follows the same trend as the heat flux input. The subsequent layers from the top to the bottom layer are respectively labeled by TE7, TE6, TE5, TE4, TE3, TE2 and TBOT. Here TBOT is the structural aluminum layer. The baseline model used to obtain a result for the TPS division consist of one TPS, FRSI, with constant layer thicknesses, as discussed in Section 5.2. The only large change in temperature throughout the TPS can be seen in the insulation layer. From the figures and Table 5.8 it can be seen that the maximum reached structural temperature is constant throughout the different temperature zones. Furthermore the figures show that the maximum temperature is reached approximately at the end of the analysis and thus trajectory. This is as expected, as the heat load input is counteracted and delayed by the TPS.

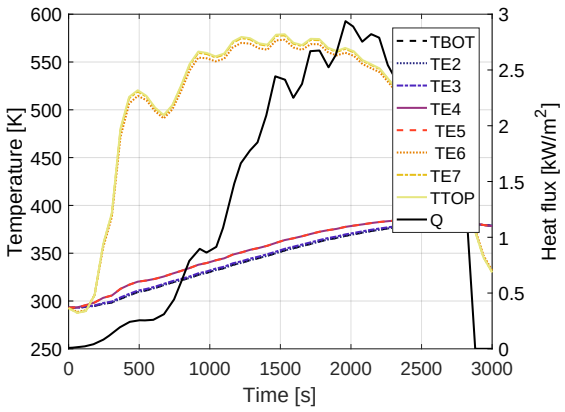

Figure 5.22: Temperatures of the layers of the critical node of the first temperature zone plotted with the input heat flux at that node

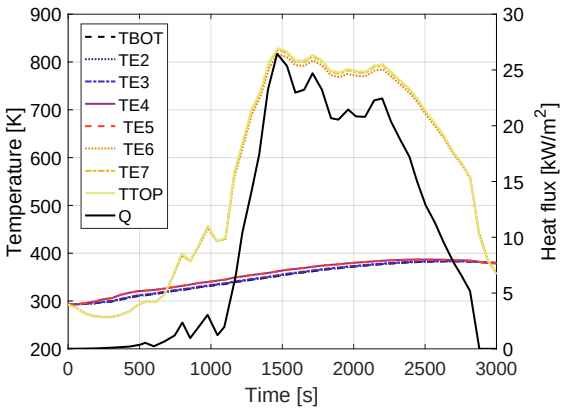

Figure 5.23: Temperatures of the layers of the critical node of the second temperature zone plotted with the input heat flux at that node

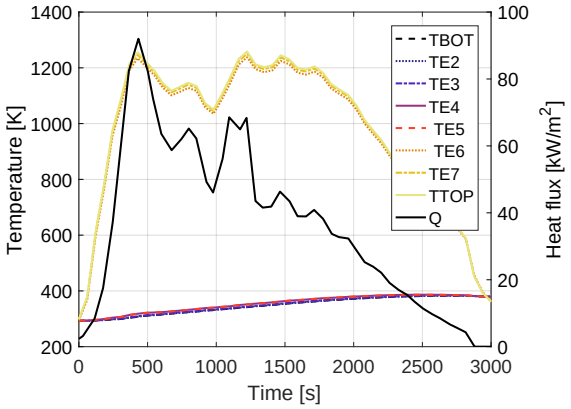

Figure 5.24: Temperatures of the layers of the critical node of the third temperature zone plotted with the input heat flux at that node

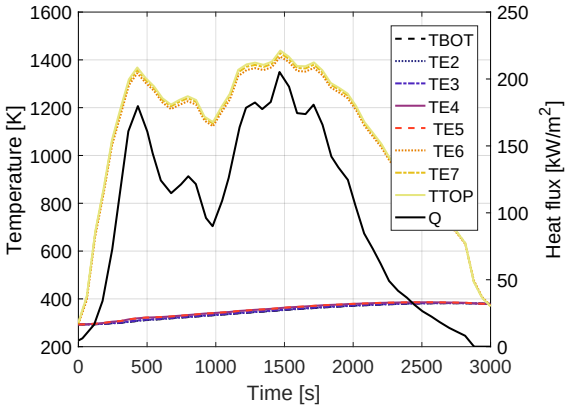

Figure 5.25: Temperatures of the layers of the critical node of the fourth temperature zone plotted with the input heat flux at that node

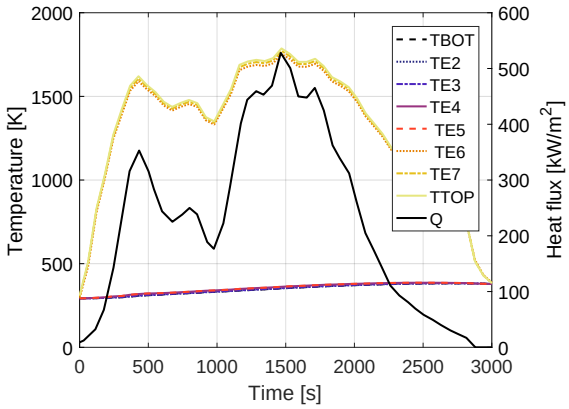

Figure 5.26: Temperatures of the layers of the critical node of the fifth temperature zone plotted with the input heat flux at that node

6

Numerical Methods

Numerical methods are sought to solve analytically complex problems, and to ensure relatively fast and easy execution of multiple calculations with varying variables. Both for the thermal analysis performed for the thesis (described in Chapter 5, as for the trajectory simulation, found in Appendix C and in the optimization scheme described in Chapter 7 numerical methods are needed. In this chapter the computational method used for the FEM model in ANSYS is described in Section 6.1. Next a closer look is taken at numerical integration in Section 6.2 and numerical interpolation in Section 6.3. These methods are used in the thermal analysis scheme and the trajectory analysis. Finally the optimization method used for the optimization of the insulation layer thicknesses is stated in Section 6.4. The use of each method is specified in the text.

6.1. Computational Methods

Numerical solutions are made at discrete points that approximate the exact solutions. The three common classes of numerical computational methods are finite difference, finite volume and finite element. The latter is used in the ANSYS software and thus used within the thesis work to model the Aurora vehicle.

6.1.1. Finite element method

The finite element method has been developed in the first half of the twentieth century. At first it was mostly used to solve torsion and stress problems, but now it is used for many applications including heat transfer. According to [29] there are seven basic steps that are involved in all finite element analyses, that can be divided into three phases;

- **Preprocessing phase**
    1. Create and discretize the solution domain into finite elements.
    2. Assume a shape function to represent the physical behavior of an element.
    3. Develop equations for an element.
    4. Assemble the elements to present the entire problem. Construct the global stiffness matrix.
    5. Apply boundary conditions, initial conditions and loading.
- **Solution phase**
    6. Solve a set of linear or nonlinear algebraic equations simultaneously to obtain nodal results.
- **Postprocessing phase**
    7. Obtain other important information.

In the first step the solution domain gets subdivided into a finite number of subdomains, which are connected at the nodes. For two-dimensional problems triangular or quadrilateral shaped elements are most commonly used. The element shapes (and the resulting nodal points) can be varied to fit the geometry that needs to be analyzed. The discretized equations must then be written for each element. These element based equations

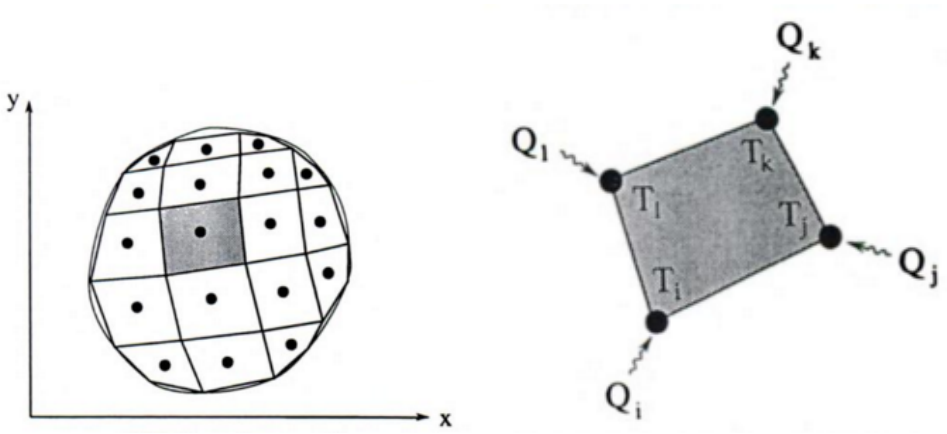

(a) Finite element mesh (b) Finite element node

Figure 6.1: Finite element method [45]

must be assembled in the next step to obtain a set of simultaneous algebraic or ordinary differential equations for the total mesh. The example depicted in Figure 6.1 shows a possible mesh and a possible element with four nodes [45]. When applied to thermal problems, at each node the respective temperature T and heat flow Q can be determined. The finite element method then determines the state of the entire element by of the state at the four nodes. For example, when the temperature of the element needs to be determined based on the four nodes i, j, k and l, Equation (6.1) can be used, in which the $N_i(x,y),...,N_l(x,y)$ parameters represent the interpolation functions of the nodes.

$$T(x,y) = N_i(x,y)T_i + N_j(x,y)T_j + N_k(x,y)T_k + N_l(x,y)T_l \tag{6.1}$$

When it comes to relating the temperature of a node to its heat flow there are two manners that can be used; a variational approach or a weighted residual approach [45]. In the first approach the partial differential equation, which expresses the conservation of energy, is replaced by an equivalent variational principle. An equation expressing the discretized conservation of energy equation for a particular element can be obtained, by using Equation (6.1) and minimization techniques from the variation calculus.

In the weighted residual method an approximate solution for the partial differential equations is assumed. This solution must obey the initial and boundary conditions. The approximate solution will not be exact, thus substition of the solution in the differential equations will lead to errors or residuals. In the weighted residual method the error vanishes (or minimizes) over a selected interval. When applied to the thermal problem a residual function is created by substituting Equation (6.1) in the partial differential equation. The discretized equations are found by integrating the weighted residual over the element domain. The discretized equation expressed as four algebraic equations are then similar to Equation (6.2), where the $[K]$ matrix represents the element's conductance. Equation (6.3) is he shorter version. In finite element computations the $[K]$ matrices are added as to form the conductance matrix for the entire system. This assembly proceeds element by element to create the total mesh [45] [29].

$$\begin{bmatrix} K_{i,i} & K_{i,j} & K_{i,k} & K_{i,l} \\ K_{j,i} & K_{j,j} & K_{j,k} & K_{j,l} \\ K_{k,i} & K_{k,j} & K_{k,k} & K_{k,l} \\ K_{l,i} & K_{l,j} & K_{l,k} & K_{l,l} \end{bmatrix} \begin{pmatrix} T_i \\ T_j \\ T_k \\ T_l \end{pmatrix} = \begin{pmatrix} Q_i \\ Q_j \\ Q_k \\ Q_l \end{pmatrix} \tag{6.2}$$

$$[\mathbf{K}](\mathbf{T}) = (\mathbf{Q}) \tag{6.3}$$

The finite element method is mathematically more complex than the other computational methods [45]. More steps need to be performed to generate the discretized equations. It is applicable, though, for complex shape modeling and when nonhomogeneous and anisotropic materials are used. This makes the method superior. For the thesis work the finite element method will be used, as it is already embedded in the ANSYS software that will be used. ANSYS is very suitable for the finite element analyses needed in the thesis work,

as it is capable of performing (among others) static and dynamic heat transfer problems [29]. It has been a leading finite element analysis program for about 40 years.

6.2. Numerical Integration

Numerical integration is used for finding approximate solutions for an ordinary differential equation (ODE). They are also known as numerical differential equation methods. There are many numerical integration methods, of which the most important ones used in the thesis work will be discussed in this section. The Euler method in Subsection 6.2.1 is not used in practice very often, but clearly describes the principles underlying several other numerical integration methods. The Runge-Kutta method described in Subsection 6.2.2 is a popular numerical integration method, as it is applicable for most numerical integration problems, although it may not always be the fastest method [40].

When selecting a numerical integration method there are several aspects that should be kept in mind;

- Truncation error; the error made in a single integration step.
- Ease of changing stepsize.
- Speed; the number of evaluations done for a certain interval for a given accuracy is known as the efficiency, often a trade-off between speed and accuracy must be done.
- Stability; the measure of how much the end results change due to minor changes in the initial conditions
- Error accumulation; the total uncertainty resulting from all error sources.

6.2.1. The Euler method

In the Euler method, it is assumed that there is a dependent variable y that is dependent on an independent variable x (often referred to as the 'time variable'). When y is vector-valued with N components it takes the following form [8];

$$y(x) = \begin{pmatrix} y_1(x) \\ y_2(x) \\ \vdots \\ y_N(x) \end{pmatrix} \tag{6.4}$$

$$y'(x) = f(x, y(x)), \qquad y(x_0) = y_0 \tag{6.5}$$

The differential equation and initial value are the input from which y can be determined for different point of x. They are written in Equation (6.5). Here the initial condition is indicated by the subscript 0. This equation can be rewritten in a scalar form, with y_{10} being the initial value of $y1$. Furthermore all partial differential equations can be written in terms of their individual components. The total equation for the dependent variable y than becomes [8];

$$\begin{pmatrix} y_1'(x) \\ y_2'(x) \\ \vdots \\ y_N'(x) \end{pmatrix} = \begin{bmatrix} f_1(x, y_1(x), y_2(x), \cdots, y_N(x)) \\ f_2(x, y_1(x), y_2(x), \cdots, y_N(x)) \\ \vdots \\ f_N(x, y_1(x), y_2(x), \cdots, y_N(x)) \end{bmatrix}, \qquad \begin{pmatrix} y_1(x_0) \\ y_2(x_0) \\ \vdots \\ y_N(x_0) \end{pmatrix} = \begin{pmatrix} y_{10} \\ y_{20} \\ \vdots \\ y_{N0} \end{pmatrix}$$

The integration of an ODE, or set of ODEs, is basically the solving of the initial value problem. All values of y are determined at the initial point x_0, but need to be determined at other points of x. An ODE can be defined in finite steps Δy and Δx, which leads to an equation that expresses the value of y for each step size Δx. When the limit is taken to be $\Delta x \to 0$ an approximation of the solution is reached. The implementation hereof is known as the Euler's method, and leads to Equation (6.6) [40].

$$y(x + \Delta x) \approx y(x) + \Delta y \qquad \text{where} \qquad \Delta y = \dot{y}(x)\Delta y \tag{6.6}$$

The Euler method will not be used in the thesis work, as it has a relatively high error accumulation, low efficiency and stability. However, the Euler method forms the basis for the often used Runge-Kutta method, as it is considered the simplest Runge-Kutta method.

6.2.2. Runge-Kutta methods

The previously described Euler methods suffers from some limitations, notably that the function f is only evaluated once every time step (Δx). In Runge-Kutta methods the derivative is evaluated multiple times per time step [8]. In this subsection the focus will first be on the fourth-order Runge-Kutta (RK4) method, also called the classical Runge-Kutta. Four different approximations are used to estimate the changes of the parameters in one integration step. The four approximations are then given weights and being averaged. The method is single-step, as the new solution y_n only depends on the previous value y_{n-1}. The RK4 method is described by Equations (6.7) and (6.8) [40].

$$y_n = y_{n-1} + \frac{k_1}{6} + \frac{k_2}{3} + \frac{k_3}{3} + \frac{k_4}{6} + O(\Delta x^5) \tag{6.7}$$

$$\begin{aligned} k_1 &= f(x_n, y_n)\Delta x \\ k_2 &= f(x_n + \frac{\Delta x}{2}, y_n + \frac{k_1}{2})\Delta x \\ k_3 &= f(x_n + \frac{\Delta x}{2}, y_n + \frac{k_2}{2})\Delta x \\ k_4 &= f(x_n + \Delta x, y_n + k_3)\Delta x \end{aligned} \tag{6.8}$$

The values of the four k's are calculated by the step size Δx and an estimation of the slope specified by function f at different locations. Δy for each step is the weighted average of the increments k. The $O(\Delta x^5)$ term describes the truncation error, which is in the order of Δx^5. The RK4 method is not subject to the shape of the derivative function as the step size Δx is fixed [40].

Adaptive step size control can be a great benefit for an integrator, as smaller steps can be taken where the function behaves unpredictable and larger steps when it is smoother. This will increase the accuracy and speed respectively [40]. It is favorable to keep the truncation error below a predefined value for every step, for this reason the truncation error must be estimated with each step. The step size Δx will be adapted such that the truncation error is at the predefined value. Erwin Fehlberg discovered a method with a fifth-order Runge-Kutta requiring six function evaluations, where a different combination of the six functions results in a fourth-order method. This method is known as the Runge-Kutta-Fehlberg (RKF45) method [40]. At each step it is determined of the proper Δx is being used by comparing the solutions of the fifth-order method and the embedded fourth-order method. The difference between the two is considered an estimation of the truncation error. If the difference is acceptably small the step size is deemed just. When it is found that the specified accuracy is not reached Δx is reduced, when the solutions are found to agree significantly better than necessary Δx is increased.

Equation (6.9) shows the general form of a fifth-order Runge-Kutta method. Here the k's represent the intermediate values and y_{n+1} the fifth-order solution. The embedded fourth-order solution is given in Equation (6.10). a, b, c and c^* are constants with several definitions. The values of these constants estimated by Cash and Karp are given in Table 6.1.

$$\begin{aligned} k_1 &= hf(x_n, y_n) \\ k_2 &= hf(x_n + a_2 h, y_n + b_{21} k_1) \\ &\cdots \\ k_6 &= hf(x_n + a_6 h, y_n + b_{61} k_1 + \cdots + b_{65} k_5) \\ y_{n+1} &= y_n + c_1 k_1 + c_2 k_2 + c_3 k_3 + c_4 k_4 + c_5 k_5 + c_6 k_6 + O(h^6) \end{aligned} \tag{6.9}$$

$$y^*_{n+1} = y_n + c^*_1 + c^*_2 + c^*_3 + c^*_4 + c^*_5 + c^*_6 + O(h^5) \tag{6.10}$$

The truncation error scales with Δx^5 and is given in Equation (6.11). For a step Δx with an error ϵ, the step Δt^* with the desired accuracy ϵ^* is estimated with Equation (6.12). From this the amount with which the step size should be increased or decreased follows.

$$\epsilon = y_{n+1} - y^*_{n+1} = \sum_{i=1}^{6} (c_i - c^*_i) k_i \tag{6.11}$$

Table 6.1: Cash-Karp Parameters for the Embedded Runga-Kutta Method [40]

i	a_i	b_{ij}					c_i	c_i^*
1							$\frac{37}{378}$	$\frac{2825}{27648}$
2	$\frac{1}{5}$	$\frac{1}{5}$					0	0
3	$\frac{3}{10}$	$\frac{3}{40}$	$\frac{9}{40}$				$\frac{250}{621}$	$\frac{18575}{48384}$
4	$\frac{3}{5}$	$\frac{3}{10}$	$-\frac{9}{10}$	$\frac{6}{5}$			$\frac{125}{594}$	$\frac{13525}{55296}$
5	1	$-\frac{11}{54}$	$\frac{5}{2}$	$-\frac{70}{27}$	$\frac{35}{27}$		0	$\frac{277}{14336}$
6	$\frac{7}{8}$	$\frac{1631}{55296}$	$\frac{175}{512}$	$\frac{575}{13824}$	$\frac{44275}{110592}$	$\frac{253}{4096}$	$\frac{512}{1771}$	$\frac{1}{4}$
j	=	1	2	3	4	5		

$$\Delta t^* = \Delta t \left| \frac{\epsilon^*}{\epsilon} \right|^{\frac{1}{5}} \tag{6.12}$$

For the propagator of the trajectory an integration method must be selected. The Runge-Kutta methods are chosen for this purpose based on their performance and the availability of a verified Runge-Kutta integrator within the trajectory simulation software TU Delft Astodynamics Toolbox (TUDAT).

6.3. Numerical Interpolation

Interpolation is the practice of fitting an unknown function $f(x)$ through a known set of data points $x_1, x_2, ..., x_N$. With an approximate function $f(x)$ an unknown data point, or set of data points, can be estimated. When the desired unknown x is between the known values of the smallest and largest x_i, it is an interpolation problem, when outside that range it is called extrapolation. Simply said in interpolation a smooth curve is drawn between the data points x_i's. The function representing this curve must be modeled by some plausible functional form, which should be able to approximate large classes functions that might arise in use [40]. The most common functional form available are polynomials, described in Subsection 6.3.1. Next natural neighbor interpolation is described in Subsection 6.3.2. Furthermore spline interpolation is tackled in Subsection 6.3.3. Finally a comparison is made to find the most appropriate interpolation methods in Subsection 6.3.4.

6.3.1. Polynomial interpolation

Polynomial integration, also known as Lagrange interpolation, fits a curve defined by an $N-1$ degree polynomial through N points. The interpolating polynomial is given by Equation (6.13) , also known as Lagrange's classical formula [40].

$$\begin{aligned} P(x) = &\frac{(x-x_2)(x-x_3)\cdots(x-x_N)}{(x_1-x_2)(x_1-x_3)\cdots(x_1-x_N)} y_1 + \frac{(x-x_1)(x-x_3)\cdots(x-x_N)}{(x_2-x_1)(x_2-x_3)\cdots(x_2-x_N)} y_2 \\ &+ \cdots + \frac{(x-x_1)(x-x_2)\cdots(x-x_{N-1})}{(x_N-x_1)(x_N-x_2)\cdots(x_N-X_{N-1})} y_N \end{aligned} \tag{6.13}$$

The downside of polynomial interpolation is that it is non-local, thus when the value of one data point changes this affects the shape of the entire curve. The method is reliable when low-degree polynomials are fitted through the points. With an increasing size of the data set the precision of the solution decreases, as the curves become more irregular.

Linear interpolation

A special case of the Lagrange interpolation equation is linear interpolation [40]. When the number of given data points n is equal to 2, it is a case of linear interpolation. Filling in $n = 2$ in Equation (6.13) gives the general equation for linear interpolation, shown in Equations (6.14) and (6.15). Here linear interpolation is done over an interval $[x_j, x_{j+1}]$ for a function $y_i = f(x_i)$ with $i = 1, ..., n$. Linear interpolation is suitable when there is a large set of data points that lie close together.

$$f(x) = Ay_j + By_{j+1} \tag{6.14}$$

$$A = \frac{x_{j+1} - x}{x_{j+1} - x_j}$$
$$B = \frac{x - x_j}{x_{j+1} - x_j} \tag{6.15}$$

6.3.2. Natural neighbor interpolation

Natural neighbor interpolation is an interpolation technique that makes use of weighted averages, and is developed by Robin Sibson [27]. To understand the natural neighbor method one must consider a data set S, consisting of n points in d-dimensional space, as depicted in Figure 6.2. The Voronoi cell of point p, V_p, contains all points that are closer to p than any of the other points in set S. A Voronoi Diagram (VD) can be computed by uniting all Voronoi cells of all points p in S. A VD is shown in Figure 6.3.

The natural neighbor concept can be used to estimate the value of a certain point x that is not present in the data set S. The natural neighbors of x are then the points in S whose Voronoi cells would change if x was added to VD(S). Hence a new Voronoi cell is created for point x, which takes some of the volume from the Voronoi cells that would be its natural neighbors. The coordinate of x with respect to a certain point p is then [27]:

$$\omega_i(x) = \frac{Vol(C_p^+)}{Vol(C_x^+)} \tag{6.16}$$

Where $Vol(C_p^+)$ is the intersection of the volume of the Voronoi cell of p and x, and $Vol(C_x^+)$ the volume of the Voronoi cell of x. The value $\omega_i(x)$ is always between 0 and 1. With the coordinates, the natural neighbor interpolation can be performed. The natural neighbors of point x are used to estimate the value of the point of another parameter, and the weight of each neighbor equals the coordinate of x compared to its neighbor ($\omega_i(x)$). The natural neighbor interpolation equation, giving the interpolated function value at point x, is:

$$f(x) = \sum_{i=1}^{k} \omega_i(x) a_i \tag{6.17}$$

Here a_i is the scalar of the desired parameter of the natural neighbor p_i. This interpolation method generates a smooth and continuous function $f(x)$, except at the data points, and honors local minimum and maximum values. The natural neighbor method can be preferred when a data set has many points, but with an uneven density distribution.

6.3.3. Spline interpolation

Spline interpolation uses splines, piecewise polynomials, to fit a multitude of low-degree polynomials through the given data points to find a fitting curve function. How well the different polynomials fit together is determined by the degree of continuity C_n. A degree C_0 indicates that the splines are continuous, hence they originate and end in the same point. C_1 indicates that the splines are tangent and C_2 that they are continuous in curvature. The required degree of continuity differs per problem, mostly C_0 and C_1 are found sufficient [40].

Cubic spline interpolation is most common, as it uses the lowest order of polynomials that can be used for

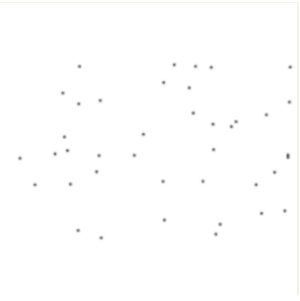

Figure 6.2: Data set S consisting of n points p [27]

Figure 6.3: VD of data set S [27]

interpolation between two points. Cubic spline interpolation strives to find an interpolation equation that is smooth in the first derivative and continuous in the second, within the interval and boundaries of the respective derivative. Assume that besides the tabulated values of y_i, there are also tabulated values of the function's second derivative y''. A cubic polynomial can then be added to the right hand side of Equation (6.14), for which the second derivative has a linear variation from value y''_j on the left to y''_{j+1} on the right. Hereby the continuous second derivative is to be found. The interpolation equation than becomes Equation (6.18), where A and B are as given in the following equations [40].

$$f(x) = Ay_j + By_{j+1} + Cy''_j + Dy''_{j+1} \tag{6.18}$$

$$\begin{aligned} C &= \frac{1}{6}(A^3 - A)(x_{j+1} - x_j)^2 \\ D &= \frac{1}{6}(B^3 - B)(x_{j+1} - x_j)^2 \end{aligned} \tag{6.19}$$

6.3.4. Usage Numerical Interpolation methods

In the thesis work, interpolation is needed for the computation of the heat flux values, as the heat flux will be provided for a certain data set of coordinates over the vehicle but will be needed for another, newly generated, data set of coordinates. The provided heat flux has a dense data set of coordinates. Linear interpolation is thus thought to be sufficient, as over small distances of the vehicle surface the heat flux will not differ largely. However, the density of the provided data set is uneven, which indicates that natural neighbor interpolation could be more appropriate. Overall linear interpolation is the preferred method, as it is the simplest and thus least time consuming method.

Interpolation is also needed to compute the aerodynamic coefficients of the vehicle from provided tabulated data. The tabulated data is given for an even number of Mach numbers, angles of attack, and deflection angles where applicable. Linear interpolation is the preferred method, both in terms of simplicity and time consumption.

6.4. Optimization Methods

In an optimization the optimal value to a certain parameter is sought for a problem, usually within a predefined set of boundary conditions. In the thesis work the optimal value for the thicknesses of the TPS' insulation layers is desired, for which the functional temperature of the structure is not exceeded. In the selection of an optimization method the two main criteria that are assessed are the solution convergence speed and the precision. As in the thesis work for every iteration a new ANSYS analysis needs to be performed, which takes a substantial amount of time, the convergence speed is the main consideration. A more elaborate explanation of the thickness optimization scheme can be found in Chapter 7. The golden-section search method is selected for the thesis work, as it converges relatively fast and the solution precision can easily be adapted if desired.

6.4.1. Golden-Section Search Optimization Method

The golden-section search method can be applied to find the minimum or maximum of unimodal functions (i.e. functions that increase monotonically for values of x smaller than $x_{maximum}$, and monotonically decrease when x is larger than $x_{maximum}$, thus having only one local maximum) [40]. An initial interval must be provided in which the single maximum is present. With the golden-section search method the interval is iteratively decreased, until the single maximum is found within a predefined error.

Figure 6.4 shows a single step in the golden-section search method, where the minimum value x is sought in function $f(x)$. There are always four points considered in the method; $f_1 = f(x_1)$ (with x_1 the lower boundary of the interval in which the maximum or minimum value must be found), $f_3 = f(x_3)$ (where x_3 is located at the upper interval boundary, and $f_2 = f(x_2)$ and $f_{4_{a/b}} = f(x_4)$. Values x_2 and x_3 are determined in the interval by the golden ratio ϕ[1];

[1]Encyclopedia of Mathematics website, http://www.encyclopediaofmath.org/index.php?title=Golden_ratio&oldid=36395, visited on 14/03/2017

$$\phi = \frac{1+\sqrt{5}}{2} \approx 1.6180 \tag{6.20}$$

$$x_2 = x_3 - \phi\frac{x_3}{x_1} \tag{6.21}$$

$$x_4 = x_1 + \phi\frac{x_3}{x_1} \tag{6.22}$$

The golden ratio is implemented to increase the rate of convergence to be as efficient as possible. It ensures that every new search interval is the same fraction of the previous interval. If the value at x_4 is f_{4_a} in Figure 6.4, it is clear that the minimum of the function lies within x_1 and x_4. These point are then the upper and lower boundary of the interval, and the new evaluation points in between are again determined by Equations (6.21) and (6.22). When f_{4_b} is the function value at x_4, the minimum is between x_2 and x_3, and these points become the new interval boundaries. If a minimum is sought this translates to the rule that if $f(x_2) < f(x_4)$ the new interval is between x_1 and x_4. When $f(x_2) > f(x_4)$ the new boundaries are given by x_2 and x_3.

The iterations that narrow down the interval are performed until the interval is within a predefined error value. The termination condition is $\epsilon <$*error*, where;

$$\epsilon = (1-\phi)(x_3 - x_1) \tag{6.23}$$

The error value is the precision within which the found value for $x_{maximum}$ or $x_{minimum}$ must be to the value of the actual maximum/minimum.

[2] Image from https://commons.wikimedia.org/wiki/File:GoldenSectionSearch.png visited on 31/03/2017

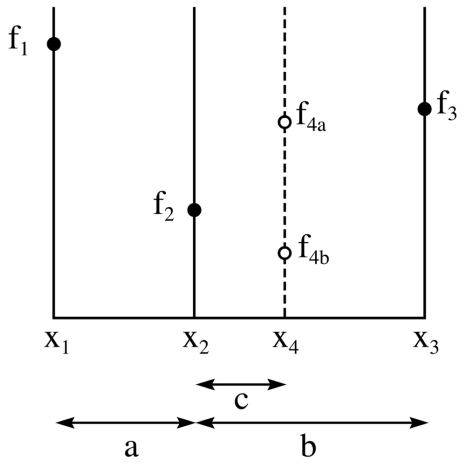

Figure 6.4: Golden section search diagram [2]

7

Optimization of the TPS

The mass of a spacecraft is always a limiting factor. Just a small increase in the mass of a system, such as the TPS, can significantly influence the feasibility of a mission. Therefore the thesis work is aimed at designing the TPS such that it has a minimal mass for the reference trajectory. The thickness of the insulation layer has a linear relation to the mass of the insulation, and thus a direct influence on the overall mass of the TPS and entire vehicle. The thinner the insulation, the lighter the vehicle. For this purpose the insulation layer is optimized to the experienced temperature. Section 7.1 gives an overview of the entire design scheme, by depicting the entire system in a high level architectural design. In Section 7.2 the thickness optimization is discussed, including a verification of the optimization scheme. The outcome of the TPS for the nominal case is presented in Section 7.3.

7.1. Optimization Scheme

For the optimization procedure an architectural design was computed, to show its functionalities and the different steps that are being performed.

7.1.1. Optimization Architectural Design

The complete optimization scheme consists of two main parts; in the first part the different TPS materials are applied to the vehicle surface, according to the results of the thermal analysis described in Chapter 5. The whole process, from the given input to the TPS design output, is depicted by a high level architectural software design in Figure 7.1. The input consists of three main components; the vehicle geometry, both as an input in ANSYS and in the aerothermodynamic program HOTSOSE, the TPS materials database, and the trajectory output data. The number of flight points to be considered is a trade-off between precision and the time the entire optimization procedure will take. An increase in the number of flight points will lead to an increase in accuracy, but also to an increase in computation time. It is desired for the optimization scheme to be completed in a range of hours, not days. A small trade-off has been made were the computation time for different numbers of flight points was estimated, and the precision of the resulting heat flux graphs were evaluated. The number of flight points considered has an almost linear relation to the computation time of the thermal analysis. It is aimed to keep the total computation time of one thermal analysis below one hour. It is estimated that with this guideline the entire optimization loop will not exceed 12 hours, and thus an optimization can be performed within a day. A thermal analysis with 50 flight points typically takes between 45 and 55 minutes. The heat flux graphs of the critical nodes for the baseline TPS division, found in Chapter 5, were checked for 30, 50 and 70 flight points. Figure 7.2 shows the heat flux input with the most variations. It can be seen that all graphs give a similar result, but for 30 flight points the accuracy is less, especially at minima and maxima. The 50 flight point heat flux is almost identical to the 70 one, and gives a better approximation of the minima and maxima compared to 30 flight points. Taking into account the computation time and the accuracy of the heat flux input, it has been decided to consider 50 flight points in the thesis work.

As can be seen in Figure 7.1 the first phase of the TPS design has two separate functions. Firstly the FEM model needs to be generated in ANSYS (as described in Chapter 5). Secondly the heat flux for all flight points needs

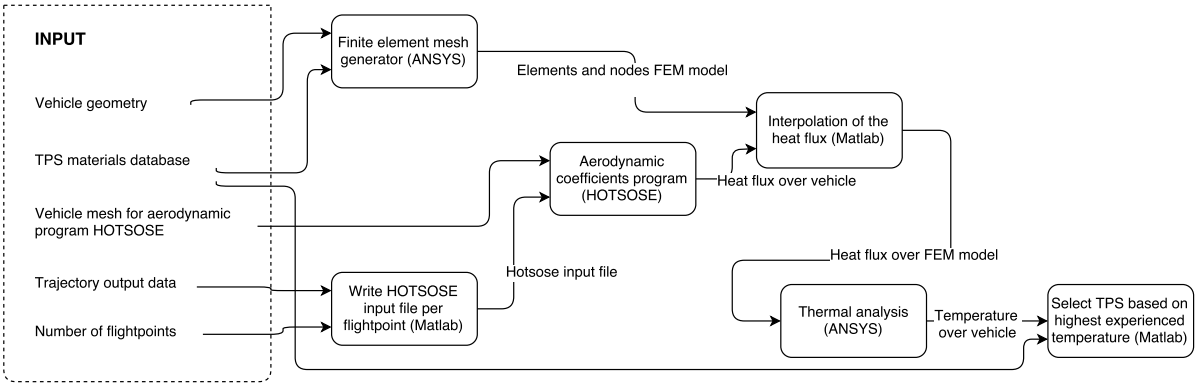

Figure 7.1: Architectural design of the TPS design scheme

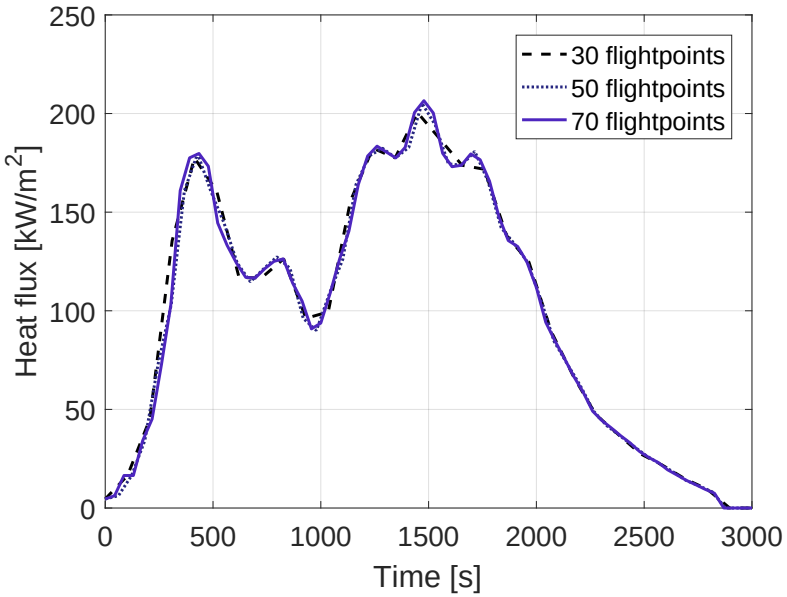

Figure 7.2: Comparison of the heat flux input graph of node 4361 for a number of 30, 50 and 70 flight points

to be generated by running the HOTSOSE software for all flight points. The HOTSOSE software is shortly described at the end of this section. Hereafter, the heat flux resulting from HOTSOSE needs to be interpolated to match the FEM model, this must be done for every flight point. The interpolation is performed in a linear fashion. Then the transient thermal analysis must be performed, to find the temperature division over the vehicle for the entire trajectory. Finally the TPS materials are appliedton the vehicle based on the maximum temperatures that are experienced at every element.

When the TPS application is performed, it is assumed that the TPS assignment to all individual elements does not change anymore. The thickness is then optimized per TPS type, as depicted in Figure 7.3. The optimization scheme specifics will be explained in further detail in Section 7.2. The transient analysis is performed. Hereafter the temperature that is reached by the structure and the TPS is analyzed. For every TPS type the node that reaches the highest structural and TPS temperature is indicated. A starting range of the thickness per TPS is provided, it is assumed that the optimal thickness is within this range. Thermal analyses are performed, from which the maximum experienced TPS and structural temperature are retrieved. The thickness range will convert to the optimum value, which is the thickness value where the structure and/or TPS reach their limit temperature (with a safety margin of 10 K applied). This way the TPS is made as thin as possible, within the functional constraints of the TPS and structural material. The top-level purpose is to have a spacecraft with a TPS mass as low as possible within the applied boundary conditions and constraints. The thickness of the insulation is linearly related to the insulation mass.

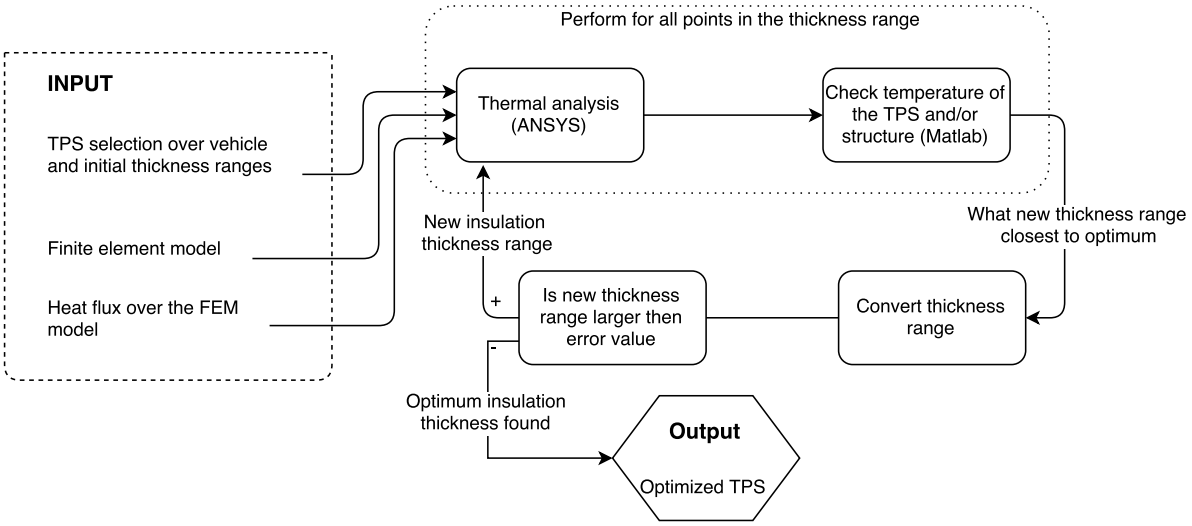

Figure 7.3: Architectural design of the thickness optimization scheme

HOTSOSE - heat flux
The HOTSOSE tool is developed by DLR and calculates the aerodynamic coefficients as well as surface pressure, temperature and heat flux distributions for the vehicle surface. In the thesis work it is used to find the heat flux over the vehicle for every flight point, where each flight point is defined by an input of the Mach number, angle of attack and altitude at that point in the trajectory. HOTSOSE is designed for hypersonic flight, and only produces valid results for high Mach numbers. When M is below 4.5 the results of HOTSOSE are not reliable anymore. Therefore the heat flux at M below 4.5 is assumed to be 0. In practice this results in a zero heat flux assumption after 2816.3 s for the baseline trajectory.

7.1.2. Verification Optimization Architectural Design

To ensure the proper working of the several steps in the complete TPS design and optimization verification steps were taken. Note that the verification of the actual optimization process of the insulation layer thicknesses will be discussed later, in Subsection 7.2.3. The verification of the FEM and thermal analysis are documented in the previous chapter. Most functionalities of the TPS design scheme were performed in Matlab. All of these were checked individually during the development process, by tests with small samples. For example the interpolation of the heat fluxes was tested in this manner. Some values of the input set were left out and computed by the interpolation function. These results were compared to the actual input values. The results hereof are displayed in Table 7.1 for a small section of the sample set, where the correspondence percentage is given of the interpolated heat flux values with the actual values for a set of arbitrary points. From this it was found that the average error is 0.04%. A different verification test was performed to ensure the proper working of the TPS area division. The results are shown in Table 7.2, where different temperature inputs were tested for dummy elements. Note that the division factor used in the verification was 1.0. Random temperature inputs were tested, as well as values that correspond to the maximum reusable temperatures of certain TPS areas, and values that exceed all maximum reusable temperatures. Furthermore the interfaces with the programs outside of Matlab were tested, such as the input file for HOTSOSE, as well as reading in the results of HOTSOSE properly. Besides the working of each individual functionality, also the entire tool was verified. This was done as well with a small sample size. After each individual functionality the results were checked, and when found valid the next step was performed. Within this verification process many iterations were made to the TPS design tool, until all results were satisfactory and considered verified.

7.2. Thickness Optimization

All TPS areas considered in the thesis work have an insulation layer, of which the thickness can be adjusted to withstand the particular experienced heat load. It is desired to find the optimum thickness of this layer for all TPS areas, so that the highest temperatures experienced by the structure of the vehicle during flight does not exceed the maximum structural temperature. The structure of Aurora consists of aluminum, of which the

Table 7.1: Heat flux interpolation verification, expressed in correspondence percentage

Point	Percentage linear interpolation [%]
1	100.00
2	100.22
3	100.00
4	99.97
5	100.01
Average	100.04

Table 7.2: TPS allocation of elements, based on their maximum temperature

Element	Maximum experienced temperature	Assigned TPS area
1	450	FRSI
2	644	AFRSI
3	1000	TABI
4	1400	AETB TUFI
5	1700	CMC
6	3000	error message

assumed maximum functional temperature is set to 450 K. The value of the maximum functional temperature of the structure is user defined and thus can be given as an input. Furthermore, the TPS itself should not experience a temperature above its maximum reusable temperature. The maximum reusable temperatures for the considered TPS areas were stated previously in Section 5.3.

7.2.1. Critical Nodes

When the elements are all assigned a certain TPS, the optimization scheme can begin. In the optimization multiple thermal analyses are performed, with different combinations of insulation layer thicknesses for the different TPS areas (see Subsection 7.2.2). After each thermal analysis it has to be determined for each TPS what the maximum experienced temperature is at the surface layer of the TPS, as well as the maximum experienced temperature of the underlying structure. For this purpose the critical nodes are identified after each thermal analysis. The critical node is the node of the particular TPS that achieves the highest temperatures. Based on the temperatures of this node the insulation layer thickness range is adjusted to be thicker or thinner.

7.2.2. Insulation Layer Thickness Adjustment with the Golden Section Search Method

The optimization of the insulation layers thicknesses can be done either with respect to the maximum experienced temperature in the structure, the maximum experienced temperature in the TPS, or both. In the tool written for the thesis work it can be defined with respect to which temperature constraint the optimization must be performed. The maximum reusable temperatures of all included TPS areas are fixed and stated in Table 5.3. The maximum temperature that is to be experienced by the structure is user defined. Typically the maximum allowed temperature for aluminum is taken between 400 and 450 K in TPS design [34].

The optimization of the insulation layer thicknesses is done with the golden-section search method, previously described in Section 6.4. In this method the minimum or maximum of a function is sought. To make sure that the concerned experienced temperature, either of the TPS or structure, is a function for which the minimum function value is found when the limit temperature is experienced, a simple function is defined. In this function also a safety margin is taken into account, ΔT_m, which is set to 10 K in the thesis work, but is also user defined and can be adjusted. Thus the optimization is done to 10 K lower than the defined maximum temperature.

$$f_{temp} = |T_{max_{TPS}} - (T_{lim_{TPS}} - \Delta T_m)| \tag{7.1}$$

$$f_{temp} = |T_{max_{struc}} - (T_{lim_{struc}} - \Delta T_m)| \tag{7.2}$$

Equations (7.1) and (7.2) are the defined functions, in which $T_{max_{TPS}}$ is the maximum experienced temperature of the TPS, $T_{lim_{TPS}}$ is the maximum reusable temperature of the TPS at hand, $T_{max_{struc}}$ is the maximum experienced temperature by the structure underneath the TPS at hand, and $T_{lim_{struc}}$ is the maximum allowed temperature to be reached by the structure.

Furthermore the range within which the optimum insulation thickness is to found must be defined for the TPS areas that are to be optimized. It has been chosen to set the minimum thickness of the insulation layer to 1.0 cm, and the maximum to 18.0 cm. From literature of other TPS analyses this range was found to be suitable for the considered TPS materials [34] [43]. This range is also user defined and can be adapted when a better sense is available at the start of the optimization of what a feasible insulation thickness would be. When a smaller range can be provided the solution will converge faster, and the computation time will decrease. When the temperatures reached by the structure and TPS are both below their maximum allowed temperatures for the entire thickness range, the insulation will be given the minimum defined thickness.

According to the golden section search method for each considered TPS four thickness values are defined per iteration step. For each of these insulation thicknesses a thermal analysis is performed in ANSYS as described in Chapter 5. For each analysis the maximum experienced temperature for the TPS and/or structure is found for each considered TPS. The functions of Equations (7.1) and (7.2) are evaluated. Based on the outcome of these functions and the golden-section search method, the new range within which the optimum thickness is to be found is defined. The principle of this operation is shown in Tables 7.3 and 7.4 for the outcome of the function and the thickness adjustment for three iterations. It can be seen that the range of thicknesses narrows down to about 40% of the original range in three iterations. For the computation of the first four values, iteration step 0, four thermal analyses must be performed. For every new iteration only one new analysis has to be performed, as the other values were computed in the previous step and can be copied from there. In the tables the newly computed value is indicated in gray.

The error value is set to 1 mm, thus the optimization will be performed until a solution is found with a maximum deviation of 1 mm to the actual optimum. This is done by calculation the value ϵ and checking if this value is smaller than the predefined error. If so, an optimum solution is found and the according thickness value can be calculated.

$$\epsilon = (1-\phi)(t_{max} - t_{min}) \tag{7.3}$$

$$t_{opt} = \frac{t_2 + t_3}{2} \tag{7.4}$$

Table 7.3: Principle of the golden-section search method applied to the TPS insulation thickness optimization, example function values

Iteration #	f(t_{min})	f(t_2)	f(t_3)	f(t_{max})
0	61.40	7.93	6.23	1.20
1	7.93	6.23	2.91	1.20
2	6.23	2.91	1.70	1.20

The optimization problem becomes more complex when multiple TPS areas are to be optimized simultaneously. For the first values of iteration step 0 four thermal analyses are performed, likewise to the procedure when only one TPS area is optimized. Per analysis the thickness values t_{min}, t_2, t_3, or t_{max} are taken for all

Table 7.4: Principle of the golden-section search method applied to the TPS insulation thickness optimization, example thickness values

Iteration #	t_{min}	t_2	t_3	t_{max}
0	0.0100	0.0749	0.1151	0.1800
1	0.0749	0.1151	0.1399	0.1800
2	0.1151	0.1399	0.1552	0.1800

TPS areas. From the resulting temperatures reached for every TPS zone, an iteration to the thickness range is made per TPS area according to the golden-section search method, in the same manner as demonstrated in Tables 7.3 and 7.4. It is likely that not all TPS area thicknesses converge in the same manner. Therefore it could happen that one TPS gets a new value for t_2, and another for t_3. In this case in the next iteration step a thermal analysis is done with all TPS thickness values t_2 and another analysis with all values t_3. It has been decided not to perform the analyses for the t_{min} and t_{max} values, due to time constraints. The optimization computation time would increase significantly which is not desired. However, this practice does introduce a flaw in the optimization scheme implementation as the function values (from Equations (7.1) and (7.2)) at the thickness interval edges do not necessarily correspond with the thickness combinations for all TPS areas once iterations are made.

When multiple TPS areas are to be optimized there are two main strategies that can be applied; either optimize the TPS areas one by one, assuming values for the not-yet optimized TPS areas and setting the insulation thicknesses for every optimized TPS, or optimizing them all simultaneously as discussed above. The latter is the more efficient method in terms of computation time, as less thermal analyses have to be performed. Therefore this method is applied in the tool. In Chapter 8 the first suggested method is tested to find if it increases the validity of the results. It was found that the maximum temperatures reached in one TPS zone can be significantly effected by a change in insulation thickness of an adjacent TPS. Thus the solution has unstable characteristics, which makes it more difficult to come to a valid solution. To account for this unstable behavior when multiple TPS areas are considered at once, some additional conditions are implemented on the iteration procedure, which are stated below.

Boundary conditions implemented on the optimization

- If the achieved temperatures at one iteration step are not decreasing for increasing thicknesses and the maximum temperature is exceeded outside of the safety margin for $T_{max}(t_3)$, the new thickness range is given by t_3 of the last iteration step and the original t_4 (of iteration step 0).
- If the achieved temperatures at one iteration step are not decreasing for increasing thicknesses and $T_{max}(t_2)$ is below the maximum temperature, the new thickness range is given by the original t_1 (of iteration step 0 and t_2 of the last iteration step.
- If ϵ is smaller than the predefined error value and $T_{max}(t_3)$ exceeds the maximum temperature with the safety margin taken into account ($T_{lim} - T_{mar}$), no optimum thickness value is found and the new interval is givel by t_3 and t_4.
- If ϵ is smaller than the predefined error value and $T_{max}(t_2)$ is below the maximum temperature with the safety margin taken into account ($T_{lim} - T_{mar}$), no optimum thickness value is found and the new interval is givel by t_1 and t_2.

7.2.3. Verification of the Thickness Adjustment with the Golden-Section Search Method

The working of the golden-section search method in the optimization of the insulation layer thicknesses was tested for some simple cases. The goal of the verification was to ensure if the method works as was expected, and to ensure its applicability to the thesis work. For this purpose four TPS functions were defined that each represent the temperature the structure would reach as a function of insulation thickness t. These multiplication factors found in the functions are arbitrary values. As in the actual optimization scheme, the absolute value is taken of the difference between the reached structural temperature and the maximum functional structural temperature, $T_{lim_{struc}}$, taken in the example as 600 K.

$$\begin{aligned} f_{TPS1} &= |(800 - 5 \cdot t) - T_{lim_{struc}}| \\ f_{TPS2} &= |(920 - 4 \cdot t) - T_{lim_{struc}}| \\ f_{TPS3} &= |(630 - 3 \cdot t) - T_{lim_{struc}}| \\ f_{TPS4} &= |(700 - 2 \cdot t) - T_{lim_{struc}}| \end{aligned} \tag{7.5}$$

The starting values for the thicknesses were also varied per TPS. It was found that after 8 iterations all solutions has converged. Their values found for all thicknesses and the analytically computed actual optimum values are stated in Table 7.5. The error value was set to 1. It can be seen that indeed all solutions of t have converged to within the error value of the actual value. Thereby the implementation of the golden-section search method is considered verified.

Table 7.5: Results of golden-section search method verification for TPS insulation thickness optimization

	TPS 1	TPS 2	TPS 3	TPS 4
Computed value t_{opt}	39.8948	80.2135	10.6763	20.5623
Actual value t_{opt}	40	80	10	20

7.3. Baseline Optimized TPS Design

The baseline optimum TPS design is generated by performing the optimization on the starting baseline model and TPS division, discussed in Section 5.6. The starting thickness ranges were between 1 and 18 cm for all TPS areas. The resulting outcomes in terms of thicknesses, critical nodes, and maximum experienced temperatures for the TPS and structure are shown in Table 7.6. In this section the design is presented, and a discussion on improvement points to the optimization is given.

7.3.1. Baseline Optimized TPS Design Outcome

The optimized values of the insulation layer thicknesses were found after 10 iterations. As the structural functional limit temperature of 450 K is not approached, the optimization has been performed to match the reusable limit temperatures of the TPS areas, stated in Table 5.3. It can be noted that the optimization scheme is not functioning as desired, because the maximum experienced temperatures of the TPS of FRSI, AFRSI and TABI exceed their respective limit temperature, with the safety margin of 10 K taken into account. A discussion on the reason behind these flawed results and how to avoid them is given in Subsection 7.3.2.

In Figures 7.4 to 7.8 the temperatures of all layers of the critical node of each TPS are given over time, with the heat flux the node is subjected to. It can be seen that all graphs follow the same trend. The highest temperature is reached early in the trajectory, after about 428.6 s. It can be noted that the heat flux values are different from the heat flux values found in Figure 7.2, this is because a different node was considered with thus a different heat flux input. Whereas the layer temperature lines follow the same trend for the different TPS areas, there is more variation in the curves of the heat flux inputs. For example, the critical node of AETB TUFI gets its highest heat flux input significantly later than the highest temperature is reached at the top layer, as depicted in Figure 7.7. This remarkable behavior can be attributed to the fact that the thermal analysis is done in 3D, and therefore the temperature and heat load coming from neighboring elements also has a large effect on the node temperature. For all TPS areas it can be seen that the temperature of the bottom structural layer increases slowly. The maximum temperatures are reached at the final analyzed flight point. The FRSI critical node top layer reaches a relatively low maximum temperature, of 638.7, as is desired. From Figure 7.4 it can be seen that the heat flux the node is subjected to is also relatively low, with a maximum of 7.8 kW/m^2. After the first peak at 428.6 s the heat flux input decreases swiftly. The temperature decrease is less steep, this can be contributed to the fact that radiation of the heat takes time, while the node still receives heat from adjacent nodes. For the AFRSI critical node the heat flux input is relatively low as well, with a maximum of 10.4 kW/m^2. However, the maximum temperature of 1387.8 K that is reached by the node is very high. As the heat flux input is rather low, this cannot be the main responsible source for the high experienced temperature. This high temperature must be a result of the combination of heat flux input and a high heat transfer value by conduction from neighboring nodes. The third TPS area, covered by TABI, reaches only a slightly higher temperature than the AFRSI temperature, but is subjected to significantly higher heat flux values, up to 120 kW/m^2. A second peak is found in the heat flux input, at 1408.2 s, just like the AETB TUFI area. This second

Table 7.6: Results baseline optimized TPS design

TPS	Optimized insulation thickness [cm]	Critical node	Maximum temperature top layer [K]	Maximum temperature bottom layer [K]
FRSI	17.9	3577	638.7	321.8
AFRSI	17.9	4386	1387.8	322.4
TABI	11.4	3907	1409.1	335.6
AETB TUFI	1.0	4361	1450.7	389.9
CMC	1.0	5814	1512.2	322.6

peak has a less significant effect on the temperature curve. This implies that a lot of the heat is conducted away. In the AFRSI graph it can be seen that the temperature stays approximately constant, with some small waves , between 980 and 1750 s, while the heat flux input is very low. Thus it is assumable that the heat of TABI and AETB TUFI is transferred to the AFRSI area by conduction. The CMC area is subjected to the highest heat flux and reaches the highest temperature, as is expected from the highest reusable temperature. The maximum heat flux input is significantly larger, with an maximum of 350 kW/m^2. The difference in maximum experienced temperatures of the AFRSI, TABI, AETB TUFI and CMC areas is relatively small, while the input heat flux values vary significantly. The heat transfer through conduction between the elements must be large. Heat is also lost by radiation to the external radiation node, representing deep space.

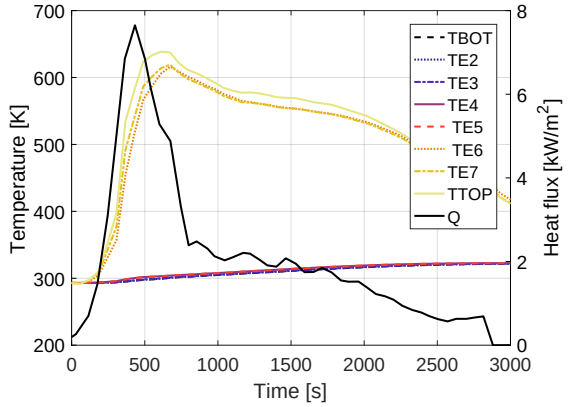

Figure 7.4: Temperatures of the layers of the critical node of FRSI of the baseline optimized TPS design

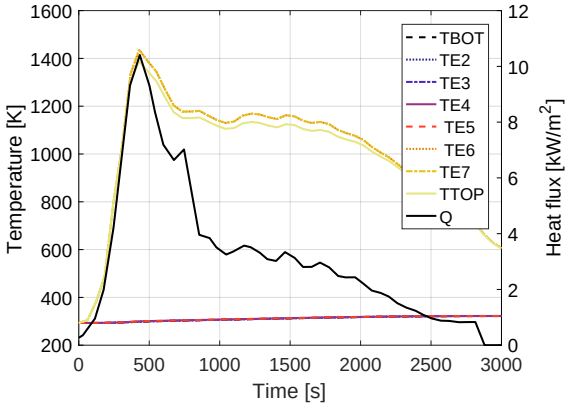

Figure 7.5: Temperatures of the layers of the critical node of AFRSI of the baseline optimized TPS design

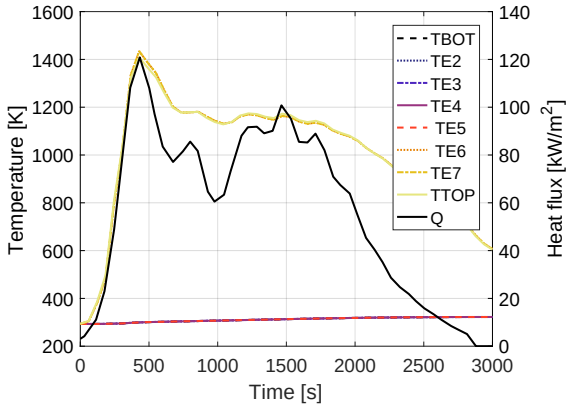

Figure 7.6: Temperatures of the layers of the critical node of TABI of the baseline optimized TPS design

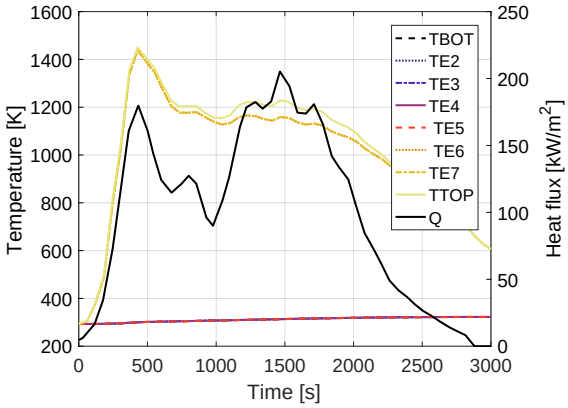

Figure 7.7: Temperatures of the layers of the critical node of AETB TUFI of the baseline optimized TPS design

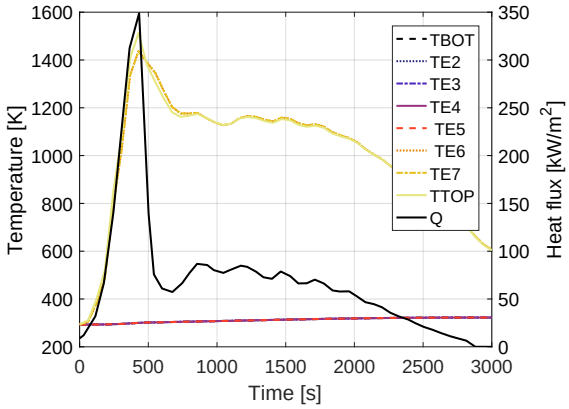

Figure 7.8: Temperatures of the layers of the critical node of CMC of the baseline optimized TPS design

The temperature of the surface of the vehicle is visualized for the time point where the critical nodes reach their maximum temperature, and at the end of the trajectory. For both time steps a view of the wind- and leeward side is provided. The results are shown in Figures 7.9 to 7.12. From these figures it can be seen that at 428.6 s the vehicle reaches high temperatures at local spots, whereas at the last analyzed time step of 3000.0 s the temperature over the vehicle has become more uniform, and the temperature range is much smaller. This makes sense as the heat flux input drastically decreases towards the end of the trajectory (for the final time steps it is even zero), and the main temperature changes come from radiation and conduction. The regions that receive the highest heat loads and thus reach the highest temperatures are the outer wing leading edge on the leeward side, and a thicker wing leading edge are on the windward side. The aerodynamic friction will be largest at the vehicles leading edges, leading to the highest heat fluxes. Therefore also the nose region has a high heat flux input and thus becomes relatively hot. Over time the heat is transferred from their initial input point over the entire vehicle. At the final analyzed flight point, at 3000 s, this is still in progress.

The temperature of the internal structure is also visualized for the same points along the trajectory, in Figures 7.13 and 7.14. The structural temperature is higher at the last time step. This is in line with the other results, as the bottom layer temperature lines of Figures 7.4 to 7.8 show that they slowly heat up during the trajectory, reaching their highest value near the end of the trajectory. The internal structural members are directly connected to the bottom layer of the TPS which is the outer structure. The variation of temperatures of the structure is in line with the surface. The highest values are reached at the leading edges of the wing, the lowest values in the middle of the wing. The leading edges are subjected to the highest heat flux inputs. Therefore the conductive heat transfer in the TPS thickness direction will be relatively larger than at other spots. This results in the higher structural temperatures at the wing leading edges. The highest structural temperature is achieved in the fuselage frames where the leading edge of the wing is connected to the fuselage. This change in shape causes a local hot spot, that also affects the inner structure. The structural material aluminum has a relatively high conductivity, and thus tends to transfer the heat flux in a high rate. However, heat flux inputs from conduction through the TPS are also transferred, and heat is radiated away to the internal radiation node representing the subsystems. In the final analyzed flight point it can be seen that the heat is distributed from the leading edges, but an equilibrium is not found yet due to the above described processes.

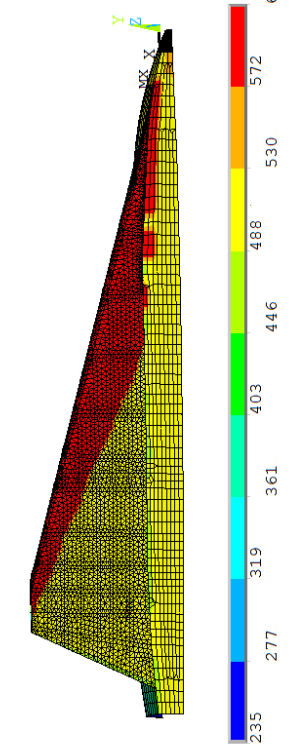

Figure 7.10: Temperature of the TPS top layer of Aurora at 3000.0 s in the trajectory, for the windward side

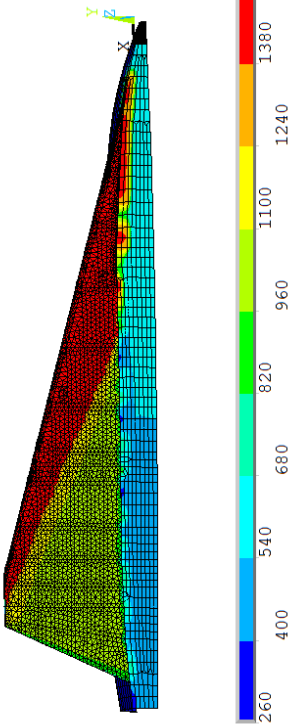

Figure 7.9: Temperature of the TPS top layer of Aurora at 428.6 s in the trajectory, for the windward side

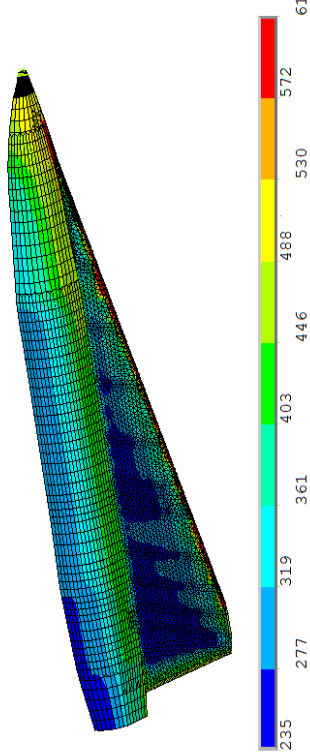

Figure 7.12: Temperature of the TPS top layer of Aurora at 3000.0 s in the trajectory, for the leeward side

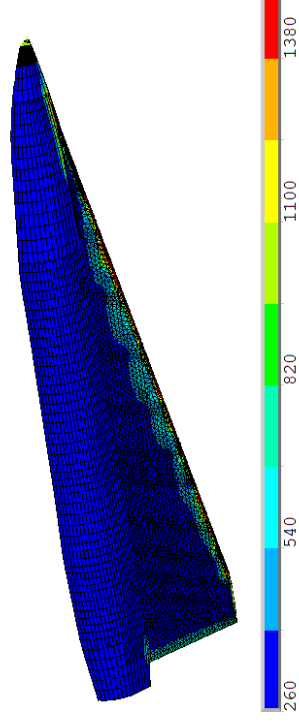

Figure 7.11: Temperature of the TPS top layer of Aurora at 428.6 s in the trajectory, for the leeward side

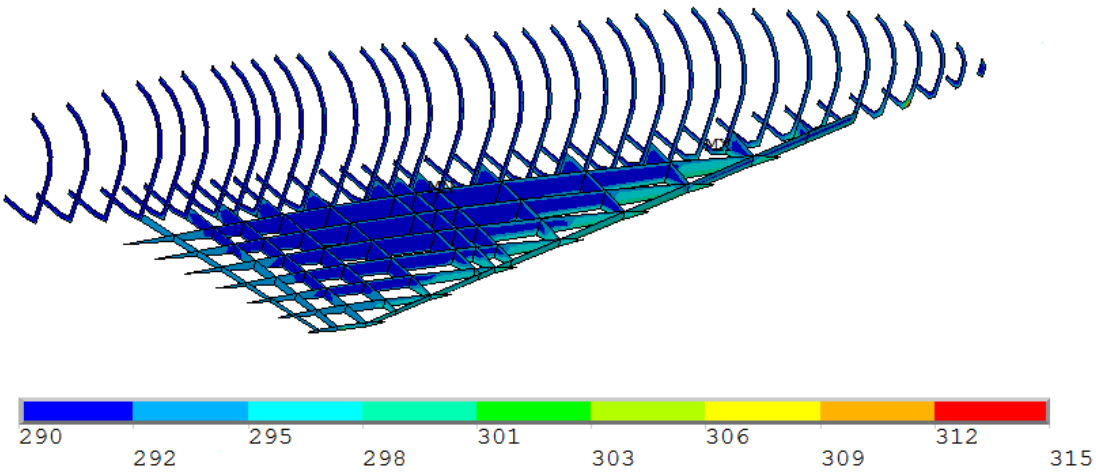

Figure 7.13: Structural member temperature of Aurora at 428.6 s

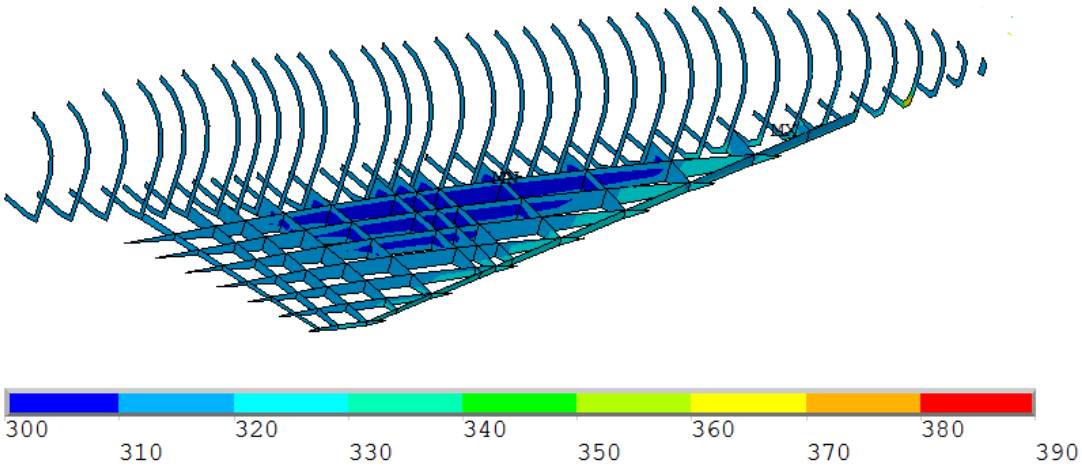

Figure 7.14: Structural member temperature of Aurora at 3000.0 s

7.3.2. Improvement Points Insulation Thickness Optimization

It becomes apparent from the results of the optimized baseline TPS design that the insulation thickness optimization procedure does not yet deliver an optimal result (see Table 7.6). In this section the reasons of the problem will be indicated and suggestions for improvement will be provided. A closer look will be taken at the iteration process of the first temperature region, with TPS FRSI. The iteration tables of the insulation thickness and the resulting maximum experienced temperature of the top layer are provided (Tables 7.7 and 7.8). Newly computed values for the thickness or temperature are indicated by a gray color. It can be seen that throughout the iterations the insulation thickness range is converged towards the initial maximum value of 18 cm. One might notice that in the first iteration there are two new values for the $T_{max_{TPS}}$, meaning that a thermal analysis is performed for both the t_2 as well as the t_3 values of the TPS areas. This implies that another TPS has converged towards the lower limit and created a new value for t_2. The limit temperature of FRSI is 644 K, with the safety margin of 10 K applied this becomes 634 K. From the tables it can be seen that the thickness optimization is going towards that temperature.

From the iterated values the final thickness of the insulation layer of FRSI is 17.89 cm, with a maximum TPS top layer temperature of 638.7 K. This exceeds the limit temperature with the safety margin applied. Moreover, this value exceeds all the temperatures reached in iteration 9. The first cause of the problem lies in the fact that multiple TPS areas are optimized at the same time. At iteration 0 the thickness ranges for all TPS go

Table 7.7: Iteration matrix of the insulation thickness of FRSI for the baseline optimized TPS design of Aurora

iteration #	t_{min} [cm]	t_2 [cm]	t_3 [cm]	t_{max} [cm]
0	1.0	7.49	11.51	18.00
1	7.49	11.51	13.99	18.00
2	11.51	13.99	15.52	18.00
3	13.99	15.52	16.47	18.00
4	15.52	16.47	17.05	18.00
5	16.47	17.05	17.41	18.00
6	17.05	17.41	17.64	18.00
7	17.41	17.64	17.78	18.00
8	17.64	17.78	17.86	18.00
9	17.78	17.86	17.91	18.00

Table 7.8: Iteration matrix of the maximum experienced temperature by the TPS of FRSI for the baseline optimized TPS design of Aurora

iteration #	$T_{max_{TPS}}(t_{min})$ [K]	$T_{max_{TPS}}(t_2)$ [K]	$T_{max_{TPS}}(t_3)$ [K]	$T_{max_{TPS}}(t_{max})$ [K]
0	695.4	641.9	640.2	632.8
1	641.9	663.1	651.0	632.8
2	663.1	651.0	643.5	632.8
3	651.0	643.5	638.8	632.8
4	643.5	638.8	637.2	632.8
5	638.8	637.2	637.2	632.8
6	637.2	637.2	637.1	632.8
7	637.2	637.1	637.1	632.8
8	637.1	637.1	637.0	632.8
9	637.1	637.0	637.0	632.8

Table 7.9: Upper thickness range values of all TPS areas for the first iteration step

iteration #	FRSI t_{max}	AFRSI t_{max}	TABI t_{max}	AETB TUFI t_{max}	CMC t_{max}
0	18.0	18.0	18.0	18.0	18.0
1	18.0	18.0	11.51	1.0	1.0

from 1 to 18 cm, and thus the $T_{max_{TPS}}(t_{max})$ value of FRSI is computed for a vehicle with all insulation thicknesses of 18 cm. However, after the first iteration it was found that AETB TUFI and CMC did not exceed their respective maximum reusable temperatures, thus their optimum thickness value was found to be the minimum of 1 cm. AFRSI converged to the maximum value and so kept the maximum thickness at 18cm, TABI converged towards the minimum and its maximum became 11.51 cm (see Table 7.9). In the implementation of the golden-section search method it is assumed that the values reached by the TPS surface stay constant for an unchanged insulation thickness, but actually this is not valid as the thicknesses of other TPS insulations can change, which will influence the maximum reached temperature because of in-plane heat transfer between adjacent TPS areas.

To further emphasize this point the thermal analyis was performed for the first two iteration steps, for the actual combinations of t_{min} and t_{max}. In Table 7.10 the results are shown when the difference is computed between the maximum TPS temperature values assumed in the optimization scheme, and the actual temperature values. It can be seen that for the first iteration steps the differences are quite large, with a maximum difference of 277.6 K. For the second iteration step with thicknesses t_{min} the difference is zero for most TPS areas. This is correct as the values for this particular thickness combination were computed in the previous iteration step, and due to the thickness range convergence became the new t_{min}. The differences for t_{max} are equal for both iteration steps as the thickness combination is equal, as convergence occurs towards the upper boundary for all optimizing TPS areas.

Table 7.10: Difference maximum experienced temperature by the TPS between the optimization scheme assumed values and the actual computed values

iteration #		FRSI	AFRSI	TABI	AETB TUFI	CMC
1	$\Delta T(t_{min})$ [K]	-38.9	-129.7	-0.1	0.1	-0.1
	$\Delta T(t_{max})$ [K]	-4.2	-277.5	-201.9	-24.5	014.5
2	$\Delta T(t_{min})$ [K]	0.0	0.0	0.0	0.4	0.0
	$\Delta T(t_{max})$ [K]	-4.2	-277.5	-201.9	-24.5	014.5

The same issue is applicable in the exceeded reusable temperature of TABI. The maximum temperature was 1409.1 K for the optimized TPS, while the limit with safety margin is 1390 K. The reusable limit of AFRSI was largely exceeded, by over 400 K. The root hereof is rather straightforward; the optimum insulation thickness did not lie in the predefined range of 1 and 18 cm, and thus could not be found.

A different cause of issues in the optimization, combined with the previously described problem, is the fact that the reached temperatures can be very sensitive to the insulation thickness. Large thickness changes can have minor impact on the reached temperatures, and small changes can have a major impact. This implies that there are turning points for the TPS areas, embodied in insulation thickness points that, when exceeded, cause a large deflection in temperature. This problem will be further discussed in the next chapter Subsection 8.1.1.

Suggestions for improvement

Investigate dependencies TPS insulation thicknesses
As the behavior of one TPS can be highly dependent on the thickness of another TPS, it would be worthwhile to get more insight in the relation between the different TPS areas. A start is made with this in Chapter 8, by varying the thicknesses of all and individual TPS areas and analyzing the results.

Adapt TPS regions (with every new iteration)
Especially from the result that the optimum insulation thickness of AFRSI is not within the predefined range, it can be concluded that the division of TPS areas is not optimal. An better division can be sought. A start is made with this in Chapter 8 by varying the division fraction number that is used. A more precise, but also more time-consuming improvement would be to redefine the TPS regions after every iteration. Due to time and capacity limits this has not been implemented within the thesis work.

Define more TPS regions
A more precise result can be obtained by defining more TPS regions, than just the applied TPS material combinations. Thus multiple regions can be assigned the same TPS. This could increase the results precision whiles also save on mass. However, this method could also introduce more issues as more dependencies would be introduced. Due to time and capacity limits this has not been implemented within the thesis work.

Perform the thermal analysis for every new insulation thickness combination
A large problem in the optimization arises from the fact that not all new insulation thickness combinations are subjected to a thermal analysis to find the appropriated experienced temperatures. It was chosen not to do this in the thesis work as the computation time would increase significantly. A larger capacity is required to implement this improvement.

Different optimization method
The golden-section search method was selected, because it has a fast convergence, to an acceptable accuracy. However, to achieve better results for the problem at hand a different optimization method might lead to more accurate results. Existing methods could be investigated, or a new method could be developed focused on the behavior of the thermal analysis.

8

Sensitivity Analysis

In this chapter sensitivity analyses are performed. Because it was found that the results of the developed optimization tool are not ideal, some studies were done to the optimization tool, and discussed in Section 8.1. To find out how robust the TPS design resulting from the written tool is, a sensitivity analysis is performed. Firstly small changes to the TPS were made, such as in the thickness of the insulation layer, to see how these affect the performance of the TPS when the nominal trajectory is flown. The performed tests and their results are presented in Section 8.2. Secondly several analyses are executed to see how well the nominal TPS design responds to small changes in the trajectory, which will lead to a change in the heat flux profile the vehicle is subjected to. These tests are described in Section 8.3. Finally the conclusions that can be drawn from the sensitivity analyses are stated in Section 8.4.

8.1. Sensitivity Insulation Thickness Optimization

In the previous chapter it was found that there are improvements to be made on the optimization scheme. Therefore, further investigations and variations in the optimization scheme were taken into account in the sensitivity analysis. First, a closer look is taken at the optimization behavior and results when only one TPS is applied to the vehicle. Second a different optimization approach is investigated, where the TPS areas are optimized one by one, instead of simultaneously.

8.1.1. One TPS Application

To get more insight in the behavior of the TPS design during the optimization process, it was decided to perform the optimization with only one TPS applied to the vehicle. Here fore AETB TUFI was chosen, because it is applicable up to a relatively high temperature regime but a low thickness will result in an exceeding of the reusable limit temperature. Thus the insulation thickness optimum lies in the chosen starting range of 0.1 and 18.0 cm. Note that this range is different from the one used for the baseline optimized TPS design. A smaller starting minimum thickness was chosen here to ensure that the optimum was within the range. As the objective of the study was not to find an applicable TPS design, but to get more insight in the optimization procedure, this is considered a valid choice. The optimization was performed both with the previously described temperature regions active, and with only one temperature region considered. The latter will be discussed first.

One temperature region

Here all elements are given the same TPS and thickness, and are all in the same temperature region. It was expected that the optimization procedure would take place straight forward, as with only one temperature region there can be no influences of thicknesses of other regions. However, this was not the case. The results of a couple iteration steps are emphasized as they show some curious behavior. These values of the thickness range and maximum experienced TPS and structural temperature are given in Tables 8.1, 8.2 and 8.3. It can be seen that in the starting step the maximum reusable TPS limit temperature (1600 K for AETB TUFI) should be within the initial insulation thickness range. The structural temperature stays well below its functional limit of 450 K for the starting values. The first remarkable behavior is the maximum experienced temperature for thickness t_2 in the starting range. The resulting temperature is higher than for a TPS with the significantly

Table 8.1: Iteration matrix of the insulation thickness when one TPS (AETB TUFI) is applied on Aurora, with only one region to be optimized, consisting of all skin elements

iteration #	t_{min} [cm]	t_2 [cm]	t_3 [cm]	t_{max} [cm]
0	0.10	6.94	11.16	18.00
1	0.10	4.33	6.94	11.16
⋮	⋮	⋮	⋮	⋮
7	0.10	0.34	0.48	0.72
8	0.10	0.25	0.34	0.48

Table 8.2: Iteration matrix of the maximum experienced temperature by the TPS when one TPS (AETB TUFI) is applied on Aurora, with only one region to be optimized, consisting of all skin elements

iteration #	$T_{max_{TPS}}(t_{min})$ [K]	$T_{max_{TPS}}(t_2)$ [K]	$T_{max_{TPS}}(t_3)$ [K]	$T_{max_{TPS}}(t_{max})$ [K]
0	1791.3	1796.1	562.4	549.6
1	1791.3	611.7	1796.1	549.6
⋮	⋮	⋮	⋮	⋮
7	1791.3	1050.3	1050.2	989.9
8	1791.3	1045.7	1050.3	1050.2

Table 8.3: Iteration matrix of the maximum experienced temperature by the structure when one TPS (AETB TUFI) is applied on Aurora, with only one region to be optimized, consisting of all skin elements

iteration #	$T_{max_{struc}}(t_{min})$ [K]	$T_{max_{struc}}(t_2)$ [K]	$T_{max_{struc}}(t_3)$ [K]	$T_{max_{struc}}(t_{max})$ [K]
0	333.9	298.7	293.0	293.0
1	333.9	293.3	298.7	293.0
⋮	⋮	⋮	⋮	⋮
7	333.9	422.5	384.3	344.1
8	333.9	456.8	422.5	384.3

lower thickness of 0.10 cm. This implies an instability in the thermal analysis.

The optimum insulation thickness solution iterates towards the initial lower limit. The results for iteration step 7 and 8 are displayed in the tables. Here it can be seen that the maximum experienced TPS temperature does not approach the temperature for the thickness of 0.10 cm. In further iteration steps the thickness range keeps becoming smaller, without a significant increase in the maximum experienced temperature. In iteration steps 7 and 8 it can be seen that the maximum experienced temperature by the structure actually increases, even exceeding the functional limit temperature. No explanation has been found yet for this increase in structural temperature. Further studies must be performed to find the reason of this behavior, focused on the heat transfer from the TPS through conduction, as this is the main source of heat load for the structural elements. From the application of one TPS on the vehicle and performing the optimization taken into account the vehicle as a whole, without optimizing the thickness for different predefined regions, it can be concluded that the results of the thermal analysis show unstable behavior.

Multiple TPS regions

Another optimization analysis was performed with one TPS applied to the vehicle, AETB TUFI, but still using the temperature regions of the baseline design. Thus five different insulation thicknesses for the five different regions are optimized. In this optimization procedure an unrealistic reusable limit temperature of 600 K was enforced on the model. This was done to ensure that for every region the optimum thickness was within the predefined thickness region of 0.10 to 18.0 cm. After 9 iterations the solution had converged to its optimum. The optimization procedure worked as intended; for every region the maximum experienced TPS temperature converged towards its limit temperature of 600 K. The optimization was done only with respect to the TPS

Table 8.4: Results optimization with only AETB TUFI applied

Temperature region	Optimized insulation thickness [cm]	Maximum temperature top layer [K]	Maximum temperature bottom layer [K]
1	0.22	875.6	546.6
2	0.60	879.3	546.4
3	0.60	927.9	548.1
4	0.98	961.4	548.1
5	11.05	1027.2	548.3

limit temperature, as for the thickness range the structural temperature stayed below its 450 K limit. The resulting thicknesses and the maximum TPS and structural temperatures per region are tabulated in Table 8.4. It can be seen that the TPS limit temperature is well exceeded for every temperature region, as is the functional structural temperature. This result is very unexpected. The values of the thicknesses and experienced temperatures of the last iteration step are shown in Table 8.5 to emphasize this. As the optimized thickness values are taken as the average of t_2 and t_3 (Equation (7.4)) the resulting temperature values are expected to be in between these values as well. It may be noted that for the fourth and fifth temperature region the limit TPS temperature is exceeded for thicknesses t_2 and t_3. This is a result of the previously discussed problem in Subsection 7.3.2 where the temperature values at t_{min} and t_{max} are no longer completely valid after iteration steps. This is because the thickness combination they represent in a new iteration step is not necessarily the thickness combination used to obtain the temperature values.

Conclusion one TPS application

From the analyses performed with only one TPS applied to the vehicle some conclusions can be drawn. It seems that for certain combinations of thicknesses non-valid results are obtained from the thermal analysis. This was seen in the analysis with one temperature region, where some thicknesses resulted in very high TPS temperatures, and others in very high structural temperatures. For the five temperature regions this behavior was only found for the optimized thickness analysis, where both the maximum experienced TPS and structural temperature were well exceeding the expected temperatures. It was thoroughly checked that the inputs of the thermal analyses are implemented and adapted correctly for every new step. Thus an error or instability must exist in the thermal analysis. It is recommended for this to be further researched. This is, however, not in the scope of the thesis work, due to time constraints.

8.1.2. Optimizing per TPS Region

In Chapter 7 it became apparent that the influence of the TPS insulation thicknesses on each other is very large. A change of the thickness of one TPS can have a large effect on the required thickness of another. It is thought that the heat transfer through conduction to adjacent TPS areas is affected by the insulation

Table 8.5: Values of iteration step 9 for the optimization with only AETB TUFI, for all temperature regions

	thickness	Region 1	Region 2	Region 3	Region 4	Region 5
Insulation thickness [cm]	t_{min}	0.10	0.48	0.48	0.86	10.93
	t_2	0.19	0.57	0.57	0.95	11.02
	t_3	0.15	0.63	0.63	1.01	11.07
	t_{max}	0.34	0.72	0.72	1.10	11.16
TPS maximum temperature [K]	t_{min}	865.3	598.4	609.8	629.4	759.0
	t_2	587.0	592.6	604.1	624.5	754.3
	t_3	580.8	586.1	597.7	617.6	747.5
	t_{max}	581.1	559.6	569.7	559.3	562.4
Structure maximum temperature [K]	t_{min}	444.8	355.7	356.4	330.6	307.5
	t_2	396.3	349.7	332.3	319.0	303.7
	t_3	372.3	336.9	324.5	314.0	301.5
	t_{max}	328.7	300.0	300.1	295.4	293.0

thickness. Especially in the thickness optimization of AFRSI this seemed to be a difficulty. Therefore it is investigated if this problem can be avoided by optimizing the different TPS insulation thicknesses one by one, instead of simultaneously. This is done both for the baseline TPS as well as for the TPS design with a division factor of 0.8. The latter is further discussed in Subsection 8.2.1. The strategy that has been implemented for this investigation is assuming a constant insulation thickness of 5 cm for all TPS areas that are not being optimized. The lowest temperature TPS, FRSI, will be optimized first, within the region of 1 and 18 cm. Hereafter the optimized thickness is set constant for FRSI, and the next TPS (AFRSI) will be optimized within the thickness range. This goes on until all TPS areas are optimized. The downside of this strategy is the large computation time that is required, compared to a simultaneous optimization approach. Furthermore it is critical that the assumed thicknesses of the TPS areas are close to the final optimized values, as a significant change in the thickness of one TPS could effect the maximum experienced temperature of a TPS for which the thickness was previously optimized.

In the implementation of the optimization per TPS region it was found that the influence of the insulation thicknesses of the different TPS areas on the maximum experienced temperatures was too large to come to a better result than in the baseline optimized TPS design. The optimization per TPS region should therefore only be implemented when a valid estimate of the required insulation thicknesses is already present. A different solution could be to take into account the maximum reusable temperatures of all TPS areas when each TPS insulation thickness is optimized individually. Thus optimizing per TPS region, but with respect to the limit temperatures of all TPS areas. An investigation herein must show whether this approach will lead to an improvement in the optimization procedure. Due to time and capacity limitations this was not implemented in the thesis work.

8.2. Sensitivity Analysis of the Nominal Trajectory

To find out if and where improvements can be made on the baseline TPS design, sensitivity studies are carried out. Here the heat flux resulting from the nominal trajectory is taken into account, and variations are applied to the TPS design. Firstly the factor by which the TPS areas are assigned to the elements of the vehicle is varied. Hereafter the insulation thicknesses are varied, for all TPS areas simultaneously as well as individually per TPS. Finally the structural material is varied.

8.2.1. Variation in the TPS Division on the Vehicle

In Chapter 5 it was explained that the assignment of the TPS areas to the different elements is done based on the temperatures reached by these elements after a first performed thermal analysis. This analysis is done for the nominal trajectory, and the assignment is done by the reusable limit temperatures of the TPS areas. A factor is taken into account, for the baseline design this factor was 0.9. In the optimized baseline design it was found that AFRSI well exceeds its reusable temperature for all insulation thicknesses that are within the predefined limit of 1 and 18 cm. Therefore investigations were done, decreasing the factor to 0.8 and 0.7 respectively, to find out how large the effect of this factor is on the optimized TPS design outcome and if a variation in the factor solves the exceeding temperature limit problem. The results of both variations compared to the baseline design are documented in Table 8.6.

A decrease of the division factor causes an increase in number of elements assigned to high temperature TPS areas, as is to be expected. The reusable temperatures of the TPS areas are kept equal to those used in the baseline optimization, with the safety margin of 10 K applied. Thus it makes sense that with a decreasing division factor the required thicknesses of the TPS areas also go down (except for the highest temperature TPS, CMC, which should stay about equal). Because with a lower division factor elements will either be assigned a higher temperature TPS, or the same TPS as in the baseline, the TPS areas will have to endure lower heat loads, except the highest temperature TPS. This behavior can be seen in the results for the TPS areas that did not receive the minimum thickness in the baseline design.

The highest temperatures experienced by the TPS areas also decrease with a decreasing division factor. This is in line with the expectations, as indicated before, as lower temperature elements are given a higher temperature TPS. It is notable that also the maximum experienced temperature of CMC decreases with a decreasing division factor, as the area where CMC is applied only increases. However, if the temperature of neighboring elements remains lower, the conduction in 3D towards the CMC elements will also be lower, and thus also

Table 8.6: Results TPS division

factor		FRSI	AFRSI	TABI	AETB TUFI	CMC
0.9	# Elements	4212	1161	4092	405	3516
0.8		3744	1208	3949	609	3876
0.7		2975	1591	1737	2598	4485
0.9	Thickness [cm]	17.89	17.89	11.39	1.00	1.00
0.8		4.40	17.89	1.00	1.00	1.00
0.7		1.00	11.39	1.00	1.00	1.00
0.9	Max TPS	638.7	1387.8	1409.1	1450.7	1512.2
0.8	temperature [K]	617.6	1313.0	1347.4	1387.6	1473.2
0.7		594.3	1136.6	1165.6	1187.9	1349.9
0.9	Max structure	321.8	322.4	335.6	389.9	322.6
0.8	temperature [K]	345.5	346.5	355.6	404.7	346.1
0.7		344.3	346.6	396.1	400.0	343.7

the conduction between CMC elements. The effect of the conduction is very notable, as the difference in maximum experienced temperature by the TPS for a division factor of 0.9 and 0.7 is over 160 K. The maximum temperature experienced by the structure actually seems to increase for a decreasing division factor, dependent on the location and TPS.

With the lower division factors the TPS areas stay within their reusable temperature bounds, except for AFRSI. With factor 0.8 applied, the same behavior appears as in the baseline, where the optimum insulation thickness is not within the predefined range. For factor 0.7 it can be seen that the thickness value is actually optimized, but the maximum reusable temperature is still exceeded by over 200 K. This can be attributed to the changing thicknesses of the other TPS areas. This problem is explained more elaborately in Subsection 7.3.2.

8.2.2. Insulation Thicknesses Variations

The insulation thicknesses of the TPS areas are subjected to a sensitivity study. They are varied, first simultaneous and thereafter on a group basis. Hereby it is desired to get a better idea of the dependency of the maximum experienced temperatures on the insulation thicknesses. Moreover it is aimed to find a TPS design which performs better than the baseline TPS design. The focus is on the maximum experienced temperature by AFRSI, which in the baseline design is exceeding the maximum reusable temperature of the TPS. Firstly Table 8.7 shows the results of an increase of all TPS insulation thicknesses by 10, 50 and 100%, in terms of the applied thicknesses and the maximum experienced temperatures by all regions. It can be seen that the percentile increases do not have a large effect on the temperatures experiences by the TPS and structure. Only for a thickness increase of 100% significant changes occur. The insignificant response of the maximum experienced temperatures can be attributed to the low thicknesses of AETB TUFI and CMC. In later variations it is found that the thickness influence of these TPS areas can have a large effect on the temperature experienced by AFRSI. With a maximum increase of 1.0 cm the effect is minor. Moreover it is found that for the increases of 10 and 50% the temperatures experienced by the TPS areas increase with small amounts for all TPS areas except FRSI. The temperatures experienced by the structure do decrease for an increasing insulation thickness. The unlikely increase in TPS temperature is thought to result from an error in the thermal analysis. However, if a higher temperature is experienced on part of the vehicle, this error will spread through conduction towards other elements.

Because it was found that the relatively small changes in insulation thickness did not lead to a design where all maximum experienced TPS temperatures were within their reusable limits, new variations were performed to find out how large the effect of the thicknesses of AETB TUFI and CMC are on the performance of the entire TPS design. Their baseline thicknesses of 1.0 cm were multiplied by 5, 10, 15 and 20. The result on the temperature of FRSI was minimal, which is expected as these TPS areas are unlikely to be neighboring each other, such that no direct conduction takes place between them. The temperatures of the other TPS areas do significantly decrease. For a new thickness of 20 cm for the two highest temperature regions AFRSI has the largest decrease, of 321 K. The tables showing all results form the performed variations can be found in

Table 8.7: Results insulation thickness variations for all TPS areas simultaneously by percentage

	Insulation thickness increase [%]	FRSI	AFRSI	TABI	AETB TUFI	CMC
Thickness [cm]	0	17.89	17.89	11.39	1.00	1.00
	10	19.68	19.68	12.53	1.10	1.10
	50	26.83	26.83	17.09	1.50	1.50
	100	35.78	35.78	22.79	2.00	2.00
Max TPS temperature [K]	0	638.7	1387.8	1409.1	1450.7	1512.2
	10	637.0	1388.2	1410.6	1451.0	1513.3
	50	635.8	1389.7	1412.6	1452.5	1514.5
	100	632.6	1364.6	1384.1	1425.2	1485.4
Max structure temperature [K]	0	321.8	322.4	335.6	389.9	322.6
	10	319.0	319.6	331.7	382.0	319.7
	50	311.5	312.0	321.4	360.3	312.1
	100	306.3	306.7	314.0	344.0	306.7

Table 8.8: Results insulation thickness variations for all TPS areas simultaneously by different factors

	FRSI	AFRSI	TABI	AETB TUFI	CMC
Thickness [cm]	35.78	35.78	22.79	25.00	25.00
Max TPS T [K]	593.5	899.6	1195.7	957.5	1131.6
Max structure T [K]	294.0	294.0	294.1	294.1	294.1

Appendix F. Even with this high thicknesses for AETB TUFI and CMC, AFRSI still exceeds its reusable limit temperature of 922. Therefore combinations of thicknesses were made to find a TPS design for which none of the limit temperatures were exceeded by the respective temperature regions. All tried combinations and their results are given in Appendix F. One combination was found that meets the limit requirements. Its results are displayed in Table 8.8. For this design the baseline thicknesses of FRSI, AFRSI and TABI were multiplied by 2, and those of AETB TUFI and CMC by 25. The resulting TPS design is not a realistic one, as the applied thicknesses are exceeding realistic values. Furthermore, all TPS areas except for AFRSI experience temperature well below their limit temperatures, and are thus over designed.

From the variation in thicknesses it can be concluded that the performance of AFRSI has a high dependency on the thicknesses of the other TPS areas. This dependency seems to be a mistake in the FEM of Aurora, as it is out of bounds. Further studies need to be performed to find the root of this problem.

8.2.3. Variation in the Structural Material

It is assumed thus far that the Aurora vehicle will have an aluminum structure. However, other materials will also be considered for the vehicle. Especially light-weight composites are of interest, as they will decrease the vehicles mass and thus lower the mission costs, while still delivering the required strength [25]. Carbon Fiber Reinforced Polymer (CFRP) is considered in the sensitivity analysis. CFRP also has a higher functional limit temperature than aluminum, of 500 K compared to 450 K. The structural internal members are given the CFRP material, as well as the bottom layers of the TPS areas, whom represent the outer structure of the vehicle. The insulation thicknesses that resulted from the baseline optimization are taken for the thermal analysis. The effects of using a different structural material are analyzed. The assumed relevant properties of CFRP are listed in Table 8.9, together with those of aluminum. Note that the thermal conductivity and specific heat vary with temperature, therefore a range is supplied. Data for the thermal variation of CFRP's specific heat was not found, therefore a constant value of 1200 J/kgK was assumed [4].

Table 8.9: Thermal properties of CFRP and aluminum [32] [28]

Material	Density [kg/m^3]	Conductivity [W/mK]	Specific heat [J/kgK]	Emissivity [-]
Aluminum	2803.2	105.9 – 190.0	343.3 – 1150.0	0.018 – 0.06
CFRP	1600	12.0 – 28.0	1200	0.9

The thermal analysis was performed for the vehicle with CFRP applied as the structural material. Furthermore the baseline optimized TPS design was applied. Table 8.10 shows the results of the analysis and a comparison with the baseline results where the structure consists of aluminum. It can be seen that the maximum experienced temperatures are equal for both analyses. A visual inspection of the result confirms this behavior. It is as to be expected, as no changes where made to the TPS design and insulation thicknesses. The structure however reaches higher temperatures, especially at the regions where the heat load is the highest, for TPS areas AETB TUFI and CMC. This is also as expected, for the specific heat of CFRP is higher than that of aluminum, and so it will heat up more under the same thermal load. The conductivity is significantly lower, thus it is expected that the the high temperatures are reached more locally. The temperature over the internal structural members is visualized at 428.6 s, where the heat flux is at its maximum for the critical nodes, and at the end of the trajectory at 3000.0 s in Figures 8.1 and 8.2 respectively. When comparing the temperature distribution with that of the optimized baseline design (Figures 7.13 and 7.14) it can be seen that at the first analyzed time point the figures look almost equal, only CFRP has a slightly larger temperature range. At the end of the trajectory it can be seen that the temperature range of the CFRP structure is significantly larger. This can be attributed to the higher heat capacity and lower conductivity. Higher temperatures are reached under the same load. The heat is transferred at a lower rate, resulting in more local high and low temperature regions. The region in the middle of the wing, that is subjected to the lowest heat load, is able to stay at a low temperature for a longer time.

Table 8.10: Results thermal analysis with CFRP as the structural material, with the baseline optimized TPS design applied

Structural material		FRSI	AFRSI	TABI	AETB TUFI	CMC
Aluminum	Max TPS	638.7	1387.8	1409.1	1450.7	1512.2
CFRP	temperature [K]	638.7	1387.8	1409.1	1450.7	1512.2
Aluminum	Max structure	321.8	322.4	335.6	389.9	322.6
CFRP	temperature [K]	326.4	326.5	333.6	446.0	327.4

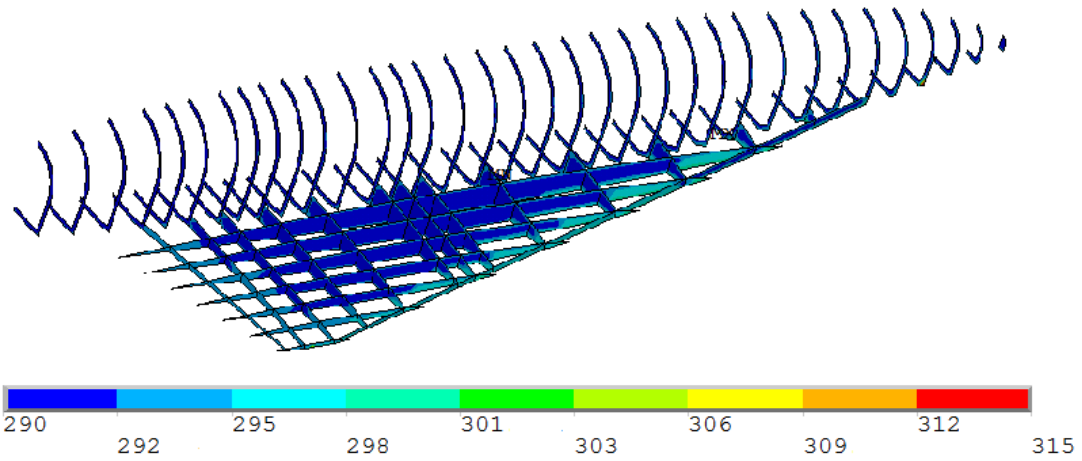

Figure 8.1: Structural member temperature of Aurora at 428.6 s,with an CFRP structure

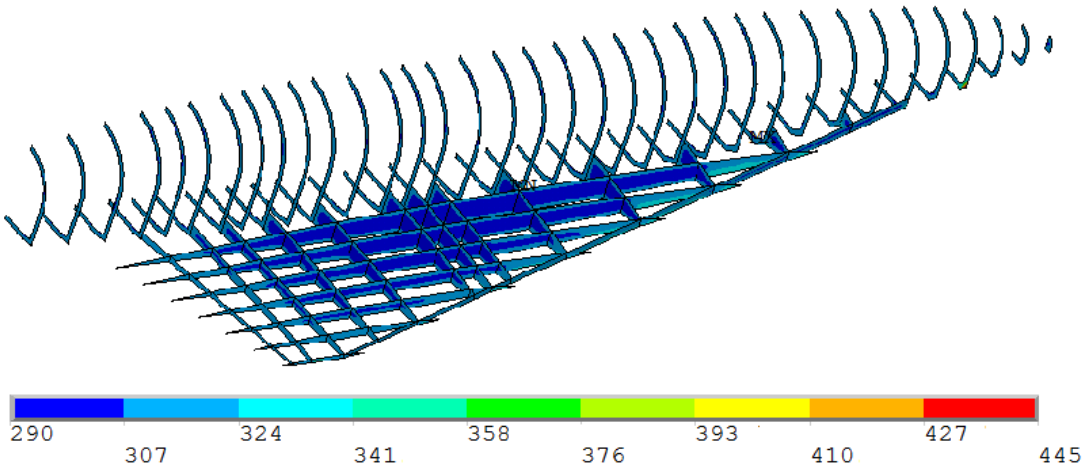

Figure 8.2: Structural member temperature of Aurora at 3000.0 s, with an CFRP structure

8.3. Sensitivity Analysis of the Baseline TPS Design

The sensitivity of the baseline TPS design is investigated by reviewing its performance when subjected to different heat flux profiles. To this purpose trajectories with different starting altitudes were applied. Furthermore the effect of a percentile increase and decrease in the nominal heat flux profile was analyzed.

8.3.1. Reentry Trajectories with Varying Starting Altitudes

To see how the TPS design performs when subjected to different trajectories, DLR provided four additional trajectories; with starting altitudes of 115, 110, 105 and 100 km. The trajectories from the DLR tool are taken, rather than using trajectories from the trajectory simulation tool developed in the thesis work which is described in Appendix C. This is decided because, as described in the appendix, there are still discrepancies between the DLR and developed trajectory simulation. The DLR trajectories are optimized, and are thus thought to be more realistic. When the same trajectory is simulated in the developed trajectory tool, a different trajectory will results which will be less realistic. This will lead to an unrealistic heat flux input for the thermal analyses. The heat flux inputs for the baseline design critical nodes are plotted for all trajectory variations in Figures 8.3 to 8.11. Next to the heat flux figures the maximum experienced temperatures are plotted. Those will be discussed later. It becomes apparent that a decrease in starting altitude results in a significant increase in maximum experienced heat flux. The maxima of the heat fluxes become more extreme. The vehicle has to decelerate over a shorter trajectory, thus more drag is required leading to a larger heat load. The total flight time decreases for the lower starting altitudes. Hence the lower the starting altitude, the larger the gradient in the heat flux becomes. A large gradient is expected to results in high experienced temperatures.

The results of this analysis in terms of maximum experienced temperatures is shown in Table 8.11. It can be seen that for every decrease in starting altitude, the maximum experienced temperature of the vehicles surface increases. This is in line with the heat flux inputs, for which the peaks increase with lower starting altitudes. The largest jump in maximum TPS temperatures over the 5 km differences is between the nominal trajectory starting at 120 km and the trajectory at 115 km, which is around 100 K for almost all TPS areas. It can indeed be seen that the differences in heat flux peak values is largest between these trajectories. The baseline optimized TPS design is not applicable to a large range of trajectories, as for the starting altitude of 115 km the first three TPS significantly exceed their reusable limit temperatures. For the trajectory starting at 105 km also AETB TUFI well exceeds its limit. Only the highest temperature region keeps within its reusable bounds for all tested trajectories. Furthermore it is notable that the maximum experienced temperature by the structure decreases for decreasing starting altitudes. This is expected because the flight time for lower altitude trajectories decreases. The structure heats up slower than the outer surface of the vehicle, thus after a shorter time it is expected that the structure has reached a lower temperature. The temperatures of the top and structural layer of the critical nodes was plotted for the critical nodes of the baseline trajectory in Figures 8.4 to 8.12. Here the top curves represent the TPS top layer temperature and the bottom curves the structural temperature. From this figures it can be seen that the structure indeed heats up almost identical for the dif-

ferent trajectories. Furthermore it is shown that the TPS temperature curves follow the same trends, but with increasing maximum values and steeper curves.

Table 8.11: Results thermal analysis with varying starting altitudes, with the baseline optimized TPS design applied

Starting altitude	Variable	FRSI	AFRSI	TABI	AETB TUFI	CMC
120 km	Max TPS	638.7	1387.8	1409.1	1450.7	1512.2
115 km	temperature [K]	693.7	1479.6	1512.6	1555.1	1615.1
110 km		743.7	1535.7	1563.5	1605.5	1668.6
105 km		764.7	1556.2	1592.8	1640.9	1710.8
100 km		783.9	1590.1	1620.5	1666.9	1737.6
120 km	Max structure	321.8	322.4	335.6	389.9	322.6
115 km	temperature [K]	319.5	320.2	333.4	388.6	320.2
110 km		317.5	318.2	331.8	389.0	318.1
105 km		315.8	316.5	331.1	391.8	316.3
100 km		314.3	315.1	330.8	394.0	314.8

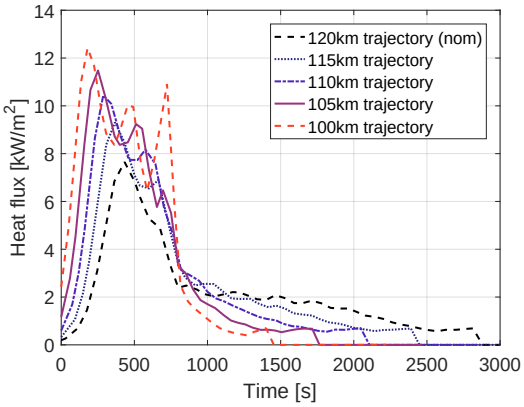

Figure 8.3: Heat flux inputs to the critical node of FRSI for all trajectory variations

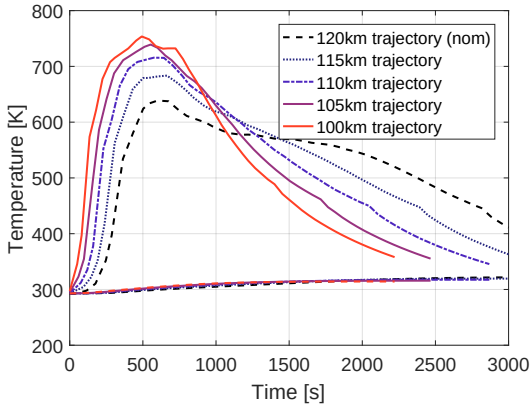

Figure 8.4: Maximum experienced temperature of the TPS top layer and structure of the critical node of FRSI for all trajectory variations

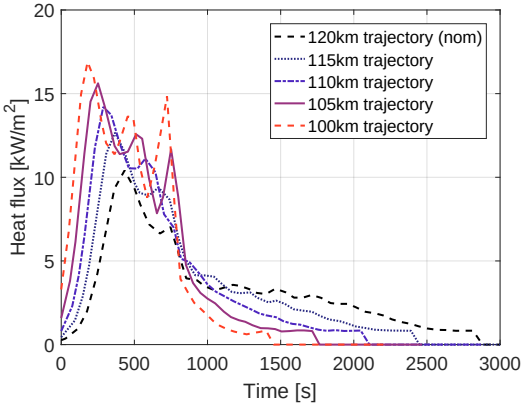

Figure 8.5: Heat flux inputs to the critical node of AFRSI for all trajectory variations

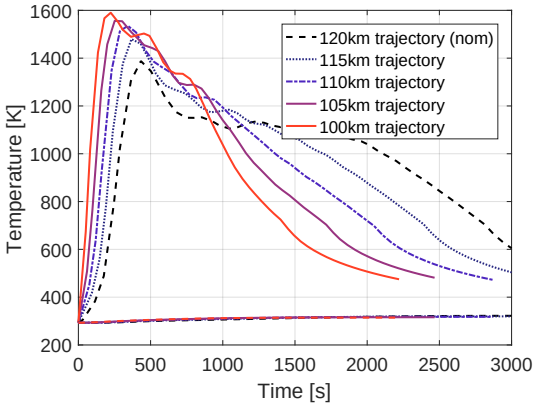

Figure 8.6: Maximum experienced temperature of the TPS top layer and structure of the critical node of AFRSI for all trajectory variations

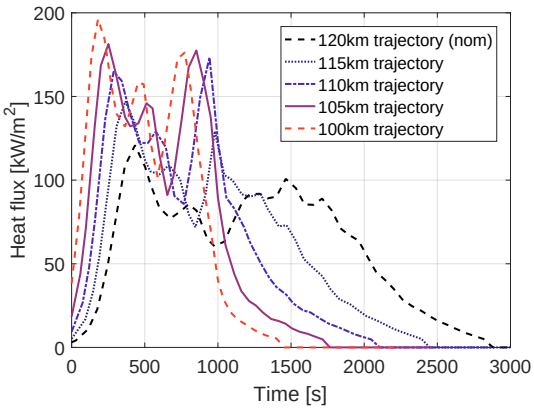

Figure 8.7: Heat flux inputs to the critical node of TABI for all trajectory variations

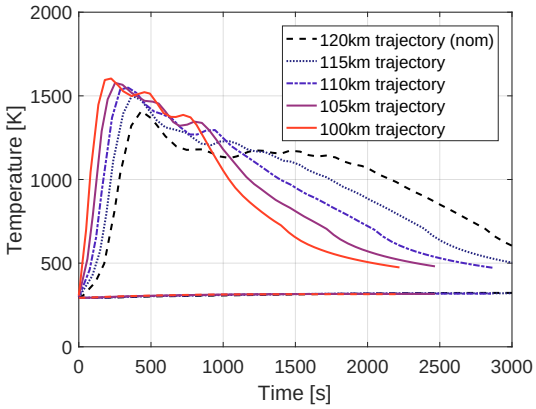

Figure 8.8: Maximum experienced temperature of the TPS top layer and structure of the critical node of TABI for all trajectory variations

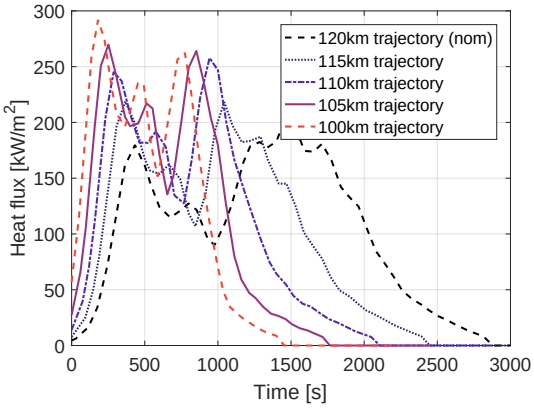

Figure 8.9: Heat flux inputs to the critical node of AETB TUFI for all trajectory variations

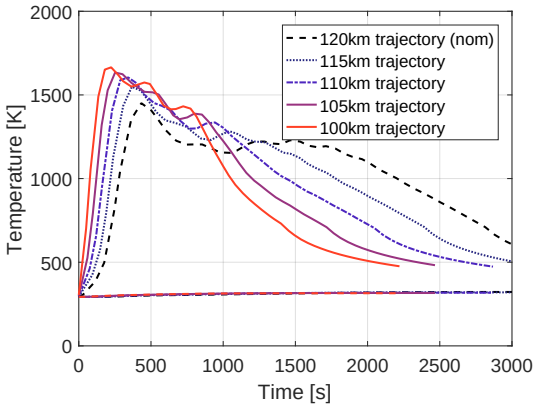

Figure 8.10: Maximum experienced temperature of the TPS top layer and structure of the critical node of AETB TUFI for all trajectory variations

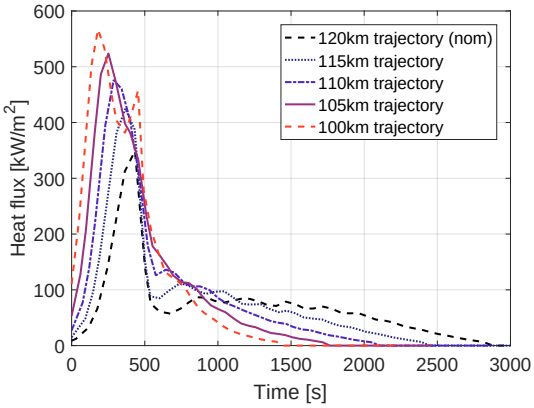

Figure 8.11: Heat flux inputs to the critical node of CMC for all trajectory variations

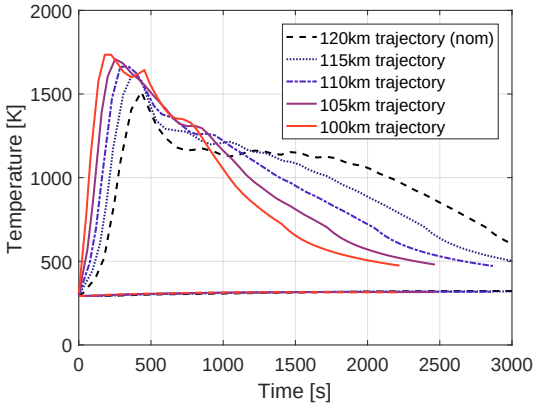

Figure 8.12: Maximum experienced temperature of the TPS top layer and structure of the critical node of CMC for all trajectory variations

Table 8.12: Results thermal analysis with a percentile increase or decrease in the input heat flux profile, with the baseline optimized TPS design applied

Increase [%]	Variable	FRSI	AFRSI	TABI	AETB TUFI	CMC
10	Max TPS	659.1	1414.3	1440.1	1476.8	1528.5
0	temperature [K]	638.7	1387.8	1409.1	1450.7	1512.2
-10		620.6	1342.1	1364.3	1395.8	1439.9
10	Max structure	323.0	323.6	337.6	395.4	323.9
0	temperature [K]	321.8	322.4	335.6	389.9	322.6
-10		320.4	321.0	333.3	384.0	321.2

8.3.2. Percentage-wise Increased and Decreased Heat Flux Profiles

Besides the alternative trajectories also a small study was performed to investigate the sensitivity of the baseline optimized TPS design to small percentile changes in the nominal heat flux input. Here for the nominal heat flux was given an increase and decrease of 10 %. The resulting maximum experienced temperatures are displayed Table 8.12. As is expected a percentile increase in heat flux results in a higher experienced temperature, both for the TPS top layer as for the structure. For the TPS the increases are roughly around the 2-4 %. For the structure the increases are a lot lower, which is as to be expected, as less of the thermal load will have an impact on the structure, due to the working of the TPS. In Figures 8.13 and 8.14 the temperatures over time are given for the variations, for the critical node of AETB TUFI and CMC respectively. The variations of the other TPS areas critical nodes look the same.

8.4. Conclusion

From the performed sensitivity analyses several conclusions can be drawn. From the investigations in the insulation thickness optimization it was found that the thermal analysis produces unstable results for different thickness values. Because of these unstable results, the optimization procedure produces ambiguous results. Further studies must be performed to identify the exact source of the issues. However, when valid results are obtained from the thermal analyses the optimization process works as intended, as was found in the optimization with one TPS applied over the five defined temperature regions. The issues described in Subsection 7.3.2 remain.

A substantiated suspicion is that there is an error in the second baseline defined temperature region. This was found from the sensitivity analysis of the nominal trajectory and the results of the optimized baseline design. The maximum experienced TPS temperature of the second region highly exceeds its limit temperature, also for the variation in TPS division on the vehicle with a lower division factor. This implies an instability in the lower temperature range of the second region. The maximum experienced temperature found from

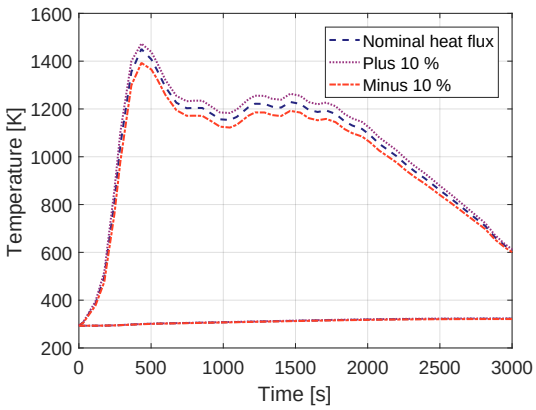

Figure 8.13: Maximum experienced temperature of the TPS top layer and structure of the critical node of AETB TUFI for percentile heat flux increases

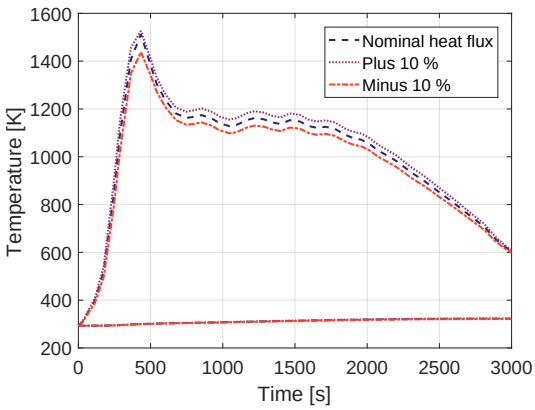

Figure 8.14: Maximum experienced temperature of the TPS top layer and structure of the critical node of CMC for percentile heat flux increases

the thermal analysis that is used to divide the TPS areas over the vehicle is a lot lower compared to the one when the AFRSI material is applied to the region. The material inputs of AFRSI were thoroughly checked and found to be correct. Furthermore a small study was performed by applying TABI to the same region, which also resulted in very high temperatures in the second region. Thus the problem was found not to emanate from faulty material inputs.

Furthermore it can be concluded that changes need to be made to the TPS division scheme. In general it can be said that small changes in the insulation thicknesses have minor impact on the performance of the TPS areas. The performance of the TPS areas is highly dependent on the insulation layer thickness of their neighboring TPS, as was found in the thickness variations. The maximum temperature of the second temperature region was brought below the AFRSI limit temperature by largely increasing the insulation thickness of AETB TUFI and CMC. The dependability is caused by heat conduction in 3D. A TPS design was found for which all TPS areas stayed below their limit temperatures. However, this was not a realistic design, as the insulation layer thicknesses exceeded reasonable limits. A change in structural material will only have an impact on the temperature of said structure, as was discovered by varying this material. It was found that CFRP functions well in terms of temperature for the baseline case. Higher temperatures are reached, but its limit is also higher than aluminum (500 K and 450 K respectively).

Reentry trajectories starting at a lower altitude will result in higher heat fluxes, over a shorter amount of time. Thus the gradient of the fluxes increases with a decreasing altitude. As is to be expected, these lower altitudes will result in higher experienced temperatures by the TPS areas of the vehicle. This was found to have a significant effect. Therefore, a TPS design that is optimized to a certain reentry trajectory heat load will not be applicable when a lower altitude reentry is performed. When a more robust TPS design is desired, a high safety factor should be applied. However, this will cause an increase in the vehicles mass that might be unnecessary. The temperature differences found in the percentage wise variation of the heat flux were less extreme than the different trajectories, for percentages of 10 and -10 %. The behavior of the TPS to these variations is as expected. From the sensitivity analyses performed for the nominal trajectory and nominal TPS design it can be concluded that the issues found in the optimization and thermal analysis procedure are rooted in the TPS design input. As changes in the TPS design are found to cause unstable results whereas changes in the heat flux input lead to an expected result.

9

Conclusion and Recommendations

The research question aimed to be answered by this thesis is:

How robust is a thermal protection system design for a spaceplane wing-body configuration to variations with respect to the design parameters or trajectory taking into account heat transfer through radiation and conduction in three dimensions?

To answer this question a tool was developed which aims to provide simple wing-body spacelaunchers with a TPS design and optimize the thickness of the insulation layers of this design. Four main tasks can be identified in the thesis work;

1. Development of a trajectory simulator
2. Development of a TPS design tool
3. Computation of the baseline TPS design for the reference case
4. Sensitivity analysis of the baseline design

In Section 9.1 an elaboration will be given of the conclusions of all these tasks. Furthermore, an answer to the research question of the thesis is provided. In Section 9.2 recommendations will be presented, both for improvement of the developed tool as for further research.

9.1. Conclusion

The reference model used for the tool development and testing was the Aurora, an SSTO launcher concept currently in development at DLR. More precisely, the Aurora-R was considered, which is equipped with a rocket-powered propulsion system. Therefore, it is assumed that the reentry trajectory is the critical phase of its flight. The critical phase is simulated by the trajectory simulator, based on its angle of attack profile, which was provided by DLR. An unpowered reentry is performed, thus the forces and moments acting on the vehicle are the gravitational and aerodynamic force. It is assumed that the vehicle is only subjected to a pitch moment. Furthermore the vehicle has to maintain a trimmed condition, to be achieved by the deflection of its body flaps. The working of the simulator was tested by verification of sub-functions and validation with the trajectory data resulting from the DLR simulator. It was found that the results agree for the first part of the trajectory. However, a discrepancy occurs that grows over time. The difference in the results of both simulators lies in the different atmospheric model used. The DLR simulator uses a polynomial atmosphere approximation, whereas the developed simulator uses the US76 atmosphere. The precision of the US76 atmospheric model is higher, whereas the polynomial approaches the values of the US76 model. These different atmospheric models cause a difference in resulting temperature, and thus speed of sound and Mach number. The difference grows over time. The developed simulator is considered validated. The trajectory resulting from the developed simulator is even more accurate than the DLR trajectory, as the US76 atmosphere is more precise than the polynomial approximation. However, for the computation of the heat flux inputs the DLR trajectory is used. As the DLR trajectory is optimized, it is thought to give a more realistic trajectory. Even though the developed tool provides a better trajectory for the given input values, the complete trajectory of DLR is more realistic for the reference case.

With the trajectory specifics known the heat flux input over the vehicles surface over time was generated, using the HOTSOSE tool provided by DLR. The heat flux forms the input load for the thermal analysis, which was to be performed. A FEM was made of Aurora, consisting of the skin of the vehicle, the ribs and spars of the wing and the frames of the fuselage. A transient thermal analysis was selected, because the temperature over the total flight time of the reentry trajectory is desired to be analyzed. In this analysis heat transfer by radiation and conduction is considered in three directions. For the radiation two kinds are assumed; radiation to outer space where the temperature is about 4 K, and radiation to the internal subsystems of the vehicle that are expected to all function around room temperature (293 K). The first thermal analysis is performed with an arbitrary TPS assigned to the vehicles skin. Based on the maximum temperatures reached by each skin element the final TPS for this element is selected by its limit reusable temperature. A database is computed of different TPS areas which can be applied to the vehicle, five in total. The leeward side of the vehicle is mostly covered with the lowest temperature TPS, FRSI. The leading edges reach the highest temperature and are therefore covered with CMC, the highest temperature TPS. The largest area of the windward side, excluding the leading edges, is covered with TABI.

With the baseline TPS design generated the thicknesses of the insulation layers were optimized, for all TPS areas. In this optimization the insulation layer thickness was aimed to be designed as thin as possible, in order to reduce the TPS mass, with two boundary conditions taken into account;

- The reusable limit temperature of the TPS will not be exceeded by the highest temperature reached by the TPS top layer
- The functional limit temperature of the structure will not be exceed by the highest temperature reached by the structural layer

To this extent the critical nodes were identified for all applied TPS areas. The critical node is defined as the node which experiences the highest temperature over the entire trajectory. The optimization was performed using the golden section search method. This method was selected as it is known to have a fast convergence time, with an acceptable accuracy. The insulation layer thickness range was defined to be between 1 and 18 cm, based on values found in literature. Thermal analyses were performed for different thickness combinations, until an optimum value was found for all TPS areas. The final thicknesses were 17.89 cm for the lowest temperature TPS areas, 11.39 cm for the middle temperature TPS, and 1.00 cm for the highest temperature TPS areas. The thicknesses of the insulation layers of the lower temperature areas are larger than expected, whereas the higher temperature area insulation thicknesses are relatively small. This implies that the TPS area division is not optimal. It was found that for three of the five TPS areas the reusable limit temperature was exceeded for the optimum thickness combination. In two of these cases they were only exceeded by a small amount, this was deemed acceptable. However, for AFRSI the temperature was largely exceeded, meaning the baseline optimized TPS design does not meet its boundary conditions. Furthermore, the maximum temperatures achieved by the structure stayed well below their functional limit.

With the baseline optimized TPS design and the nominal trajectory some sensitivity analyses were performed. Firstly the optimization procedure was investigated. It was found that the thermal analysis produces unstable results. The optimization procedure functions as intended, however changes can be made to increase its accuracy. A substantiated suspicion exists that there is an error in the second temperature region, where the baseline design well exceeds the limit reusable temperature. More investigations to this error must be performed. In the next part of the sensitivity analysis it was investigated what effect changes in the baseline TPS design would have on its performance, when the nominal trajectory was followed. Here a large dependency was discovered between the performance of one TPS and the insulation layer thicknesses of other TPS areas. Thickness values were found for which none of the TPS areas exceeds their reusable limit, however these thicknesses are not considered realistic as they are very high. Finally a study was performed to the performance of the baseline optimized TPS design when changes to the trajectory and input heat flux were made. Lowering the starting altitude of the reentry trajectory has a large effect on the heat flux profile, increasing the maxima values and the gradients of the heat flux. The resulting temperatures experienced by the TPS as a result also increase significantly. The safety margin of 10 K taken in the optimization is by far not enough to account for this. A percentage wise increase and decrease of the heat flux was also investigated. As expected an increase in the heat flux causes an increase in the experiences temperature and vice versa. These differences are less extreme than for the varying starting altitudes. However, for an increase of 10%, the safety margin of 10 K still would not suffice.

Finally the main research question of the thesis can be answered: *How robust is a thermal protection system design for a spaceplane wing-body configuration to variations with respect to the design parameters or trajectory taking into account heat transfer through radiation and conduction in three dimensions?* The tool developed in the thesis work proves that a TPS design can be developed for a simple wing-body configuration, with the specified conditions taken into account. However, it was found that the resulting baseline design did not lead to a completely functional TPS design, as one of the TPS areas well exceeded its limit temperature. Multiple reasons were found for this error. It is expected that there is an error or unstable point present in the defined second temperature region, were the exceeding temperature is experienced. Furthermore in the application of the golden section search method the assumption made to save time that only a new thermal analysis needs to be performed for newly generated thickness values, in stead of all new thickness combinations, leads to an error. It is expected that solving the above mentioned issues will lead to an acceptable and functioning TPS design. However, to be certain, more research must be performed. An elaboration on the proposed improvements to the developed tool and research are given in the next section.

9.2. Recommendations

Recommendations can be made for future work, following from the thesis. First recommendations will be given for tool improvement. Hereafter suggestions for further research will be given.

Apply usage of the developed trajectory simulation tool
At the moment the trajectory inputs of DLR are used, in stead of those of the developed tool. This is decided upon as the trajectory is optimized for the reference mission in the DLR tool, and there is a discrepancy between the DLR tool and the developed trajectory optimization. It is recommended to further analyze the differences between the two tools, so that the developed trajectory tool can be taken into use.

Add ascent phase to trajectory simulation
Currently only the reentry phase is considered in the trajectory simulation tool. To improve functionality it is suggested to also add the ascent phase. This will be helpful when in future usage of the tool also vehicles with air-breathing propulsion systems will be considered (such as Aurora-AB), for which the ascent is the critical phase.

Enlarge considered flight time
At the moment the trajectory time take into account for the reentry is until the vehicle is about 40 km above the ground. However, in some cases it is possible that the maximum temperature is experienced by the structure later, as the structure can still receive heat transfer by conduction from hotter higher layers. The maximum structural temperature might even occur after touch down. Heat is stored in the TPS and occasionally it can be transferred to the structure when the vehicle is already on the ground. Therefore it can be favorable to consider a slightly longer time in the optimization of the TPS than the nominal flight time for the reentry trajectory. It is recommended to add this to the tool to enhance precision.

Add heat loads due to aerodynamic pressure
In the thesis work it is assumed that the vehicle only heats up due to loads from the heat flux. In reality, also the pressure on the vehicle will result in an increase in temperature. For more precision and more reliable results it is recommended to also take heat due to pressure into account, for the thermal analysis.

Improvements heat flux input
The heat flux output from the hypersonic aerodynamic tool HOTSOSE is questionable for the combination of high Mach number, high angle of attack and high altitude at the fuselage. In the analysis this was not deemed a significant problem as this combination only happens at the beginning of the reentry trajectory, where the heat flux is not at its critical point yet. However, for future usage the output of such combinations of HOTSOSE should be checked to increase accuracy of the tool. Furthermore, HOTSOSE is only capable of generating reliable results for high Mach numbers. In the tool therefore it is assumed that the heat flux is equal to zero when the velocity is lower than 4.5 M. As this is not actually the case, it is recommended to add heat flux inputs for lower Mach numbers, to increase precision.

Add thermal expansion
The expansion of the different TPS areas and their materials under a heat load was not considered in the thesis work. However, this could be a troublesome behavior as expansion could lead to stress, and shrinkage could result in gaps in the TPS. As the different TPS areas applied to the vehicle will have different results it is recommended to take this into account in future work. Furthermore the behavior of the different material layers within one TPS might also show different behavior.

Expand the TPS database
For the thesis work the TPS database from which TPS areas were selected consisted of five different TPS areas. It is recommended to expand this database with other TPS material combinations that are applicable for reusable spaceplane missions. Especially the addition of metallic TPS areas is thought to be a useful addition that will increase the performance of the TPS design resulting from the tool.

TPS division by areas
The division of TPS areas over the vehicle is now done on an element basis. For future work it is recommended to change this to an area basis. This will result in a more realistic TPS design as TPS areas are always applied over larger areas of the vehicle.

TPS mass estimation
A mass estimation can be added to the TPS optimization. With an added mass estimation easily sanity checks can be performed on the outcome design. Momentarily the density of the TPS areas is known, dependent on the insulation layer thickness. A functionality can be added to calculate the total TPS mass based on the TPS area division and insulation thickness. Furthermore, the mass of the structure can be calculated.

Improvement TPS division scheme
The TPS division scheme can be improved upon. At the moment it is based on the maximum experienced temperature of the TPS when an arbitrary TPS is applied, with a division factor. However, in the resulting design it is found that for some TPS areas the optimum thickness is not within the predefined thickness range. When the insulation thickness can be lower than the predefined minimum, a lower temperature TPS would also be applicable. An investigation must be performed in a better applicable TPS division scheme. Another solution would be to adapt the TPS division over the vehicle at every optimization iteration step. However, this is thought to increase the computation time significantly.

Improvements optimization scheme
To improve the optimization scheme it is recommended to perform the thermal analysis for every new insulation thickness combination, instead of only for newly computed thickness values, as was done in the thesis work. A longer computation time will be required, however a significant improvement in the design accuracy is expected.

Research thermal analysis
In the thesis work it was found that the thermal analysis shows unstable behavior for different thickness combinations. A substantiated suspicion exists that there is a troublesome point in the second defined temperature region of Aurora. A more elaborate research will need to be performed to find the root of the problem and correct for it.

Research optimization scheme
It was found that there are improvements to be made to the optimization scheme. Research needs to be done to investigate the results of several changes to the procedure. Suggestions for improvement include the adaption of the temperature regions at every new iteration and definition of more temperature regions. Furthermore it is recommended to perform a study to find if their are optimization methods besides the golden section search methods that can be applied to the tool.

Validation TPS design
To ensure the validity of the outcome TPS designs of the tool, it is recommended to perform validations by comparing the outcomes with TPS designs of existing space missions. From such a validation conclusion can be drawn with respect to the applicability of the outcome TPS designs of the optimization tool. When a mass

estimation is added at that time, the TPS mass and mass ratio between the TPS and structure should also be compared to existing missions.

Bibliography

[1] ANSYS, I., *ANSYS Mechanical APDL Thermal Analysis Guide*, ANSYS, Inc., Canonsburg, 15th ed., November 2013.

[2] ANSYS, I., "ANSYS Help Viewer 17.1," Help viewer software, 2016, Release 17.1 Downloaded on 6-9-2016.

[3] Asada, S., Miyake, S., Kouchiyama, J., Akimoto, T., and Shirouzu, M., "Lessons Learned From HOPE System Design," *AIAA*, , No. AIAA-2001-1881, April 2001.

[4] Bai, Y., Vallée, T., and Keller, T., "Modeling of Thermal Responses for FRP Composites Under Elevated and High Temperatures," *ScienceDirect*, Vol. 68, No. 1, Jan 2008, pp. 47–56.

[5] Behrens, B. and Müller, M., "Technologies for Thermal Protection Systems Applied on Re-usable Launcher," *Acta Astronautica*, Vol. 55, 2004, pp. 529–536.

[6] Blosser, M., "Fundamental Modeling and Thermal Performance Issues for Metallic Thermal Protection System Concept," *Journal of Spacecraft and Rockets*, Vol. 41, No. 2, March 2004, pp. 195–206.

[7] Bond, A., Varvill, R., Scott-Scott, J., and Martin, T., "SKYLON - a Realistic Singe Stage Spaceplane," *Spaceflight*, Vol. 45, April 2003, pp. 158–161.

[8] Butcher, J., *Numerical Methods for Ordinary Differential Equations*, No. ISBN 978-0-470-72335-7, Wiley, 2nd ed., 2008.

[9] Buursink, J., *On the Development of a Cooled Metalic Thermal Protection System for Spacecraft*, Ph.D. thesis, TU Delft, 2005.

[10] Cengel, Y. and Ghajar, A., *Heat and Mass Transfer: Fundamentals & Applications*, McGraw-Hill, 4th ed., 2011.

[11] Chapman, D., "An Analysis of the Corridor and Guidance Requirements for Supercircular Entry intro Plantery Atmospheres," *GPO*, Vol. 55, 1960.

[12] Churchward, R., "Examples of thermal protection systems for reentry vehicles," Handout of presentation at Workshop on Thermal Technology for the Brazilian Reentry, November 2000.

[13] Clay, C., Croop, H., and Camden, M., "TPS and Hot Structures for RLV," *Proceedings of the 4th European workshop on TPS for Space Vehicles Palermo, nov 2002*, No. ESA SP-521, ESA, Noordwijk, November 2003.

[14] Curry, D., "Space Shuttle Orbiter Thermal Protection System Design and Flight Experience," Tech. rep., NASA, 1993.

[15] Czaplak, C., "Tragedy and Standard Development Columbia Space Shuttle," Catholic University of America.

[16] Dorsey, J., Poteet, C., Wurster, K., and Chen, R., "Metallic Thermal Protection System Requirements, Environments, and Integrated Concepts," *Journal of Spacecraft and Rockets*, Vol. 41, No. 2, March 2004, pp. 162–172.

[17] Eggers, T., Dittrich, R., and Varvill, R., "Numerical Analysis of the SKYLON Spaceplane in Hypersonic Flow," *AIAA*, , No. AIAA 2011-2298, April 2011, 17th AIAA International Space Planes and Hypersonic Systems and Technologies Conference.

[18] Garbers, N., "Thermal protection system Optimization Program Version 2 (TOP2)," Tech. Rep. SART TN-09/2014, DLR, 28359 Bremen, 2014.

[19] Gilmore, D., *Spacecraft Thermal Control Handbook*, No. ISBN 1-884989-11-X, The Aerospace Corporation Press, 2nd ed., 2002.

[20] Glass, D., "Ceramic Matrix Composite Thermal Protection Systems and Hot Structures for Hypersonic Vehicles," *AIAA*, , No. AIAA 2008-2682, April-May 2008, 15th AIAA International Space Planes and Hypesonic Systems and Technologies Conference.

[21] Greulich, D., "Thermal Protection Systems for FSS-15 C/Sic-Shingle-Concept," Tech. rep., ESA, 1999.

[22] Hammond, W., *Design Methodologies for Space Transportation Systems*, No. ISBN 1-56347-472-7, AIAA, 2001.

[23] Hempsell, M., *SKYLON Users's Manual*, Reaction Engines Limited, Culham Science Centre, Adingdon, Oxon, OX14 3DB, UK, May 2014.

[24] Infed, F., Handrick, K., Lange, H., Steinacher, A., Weiland, S., and Wegmann, C., "Development of Thermal Protective Seal for Hot Structure Constrol Surface Actuator Rod," *Acta Astronautica*, Vol. 70, January-February 2012, pp. 22–138.

[25] Kopp, A., "Hypersonic Launcher Concept Aurora Configuration Aurora-R1 Preliminary System Design Summary," Tech. Rep. SART TN-004/2016, DLR, 2016.

[26] Kuczera, H., Sacher, P., and Dujarric, C., "FESTIP system study - An overview," *International Space Planes and Hypersonic Systems and Technologies Conference*, 1996.

[27] Ledoux, H. and Gold, C., *Developlements in Spatial Data Handling*, chap. An Efficient Natural Neighbour Interpolation Algorithm afor Geoscientific Modelling, No. ISBN 3-540-22610-9, Springer, 2005, pp. 97–108, Department of Land Surveying and Geo-Informatics, The Hong Kong Polytechnic University.

[28] Mital, S., Gyenkenyesi, J., Arnold, S., Sullivan, R., Manderscheid, J., and Murthy, P., "Review of Current State of the Art and Key Design Issues With Potential Solutions for Liquid Hydrogen Cryogenic Storage Tank Structures for Aircraft Applications," Tech. Rep. NASA/TM-2006-214346, NASA, October 2006.

[29] Moaveni, S., *Finite Element Analysis, Theory and Application with ANSYS*, No. ISBN 0-13-785098-0, Prentice-Hall, 1999.

[30] Mooij, E., "Re-entry Systems," Draft Lecture Notes AE4870B TU Delft.

[31] Morris, C. J., "National Aero-Space Plane Achievements and U.S. Space-Launch Goals," *AIAA*, , No. AIAA-95-6052, April 1995, 6th International Aerospace Planes and Hypersonic Technologies Conference.

[32] Mouritz, A., *Introduction to Aerospace Materials*, No. ISBN-978-1-85573-946-8, Woodhead Publishing Limited, 2012.

[33] Mulder, J., van Staveren, W., van der Vaart, J., de Weerdt, E., in 't Veld, A., and Mooij, E., "Flight Dynamics," Lecture Notes, March 2013, AE3202.

[34] Myers, D., Martin, C., and M.L.Blosser, "Parametric Weight Comparison of Advanced Metallic, Ceramic Tile, and Ceramis Blanker Thermal Protection Systems," Tech. Rep. TM-2000-210289, NASA Langley Research Center, Hampton, Virginia, June 2000.

[35] NOAA, NASA, and USAF, *U.S. Standard Atmosphere, 1976*, U.S. Govt. Print. Off., 1st ed., October 1976.

[36] Noomen, R., "Space Mission Design: Basics," Lecture Notes AE 4878 TU Delft, September 2014.

[37] Palmer, G., Kontinos, D., and Sherman, B., "Surface Heating Effects of X-33 Vehicle Thermal-Protection-System Panel Bowing," *Journal of Spacecraft and Rockets*, Vol. 36, No. 6, November-December 1999, pp. 836–842.

[38] Papp, Z., *Mission Planner for Heating-Optimal Re-Entry Trajectories with Extended Range Capability*, Master's thesis, TU Delft, December 2014.

[39] Plansee, M., "Dispersion Strengthened High-temperature Materials," brochure, 2005.

[40] Press, W., Teukolsky, S., Vetterling, W., and Flannery, B., *Numerical Recipes in C: the Art of Scientific Computing*, No. ISBN 0-521-43108-5, Cambridge University Press, 1992.

[41] Pulci, G., Tirillo, J., Marra, F., Fossati, F., Bartuli, C., and Valente, T., "Carbon-phenon ablative materials for re-entry space vehiles: Manufacturing and properties," *Elsevier*, June 2010.

[42] Scotti, S., Clay, C., and Rezin, M., "Structures and material technologies for extreme environments applied to reusable launch vehicles," *AIAA*, , No. AIAA 2003-2697, 2003.

[43] Sippel, M. and Schwanekamp, T., "The SpaceLiner Hypersonic System - Aerothermodynamic Requirements and Design Process," 8th European Symposium on Aerothermodynamics for Space Vehicles.

[44] Tamma, K. and Thornton, E., "Re-Entry Thermal/Structural Finite-Elment Modeling/Analysis of Shuttle Wing Configurations," *Journal of Spacecraft and Rockets*, Vol. 24, No. 2, March-April 1987, pp. 101– 108.

[45] Thornton, E., *Thermal Structures for Aerospace Applications*, No. ISBN 978-1-60086-254-0, AIAA, January 1996.

[46] Varvilland, R. and Bond, A., "The Skylon Spaceplane: Progress to Realisation," *JBIS*, Vol. 61, April 2008, pp. 412–418, presented at British Interplanetary Society's " Next Steps for Space Infrastructure Symposium".

[47] Weihs, H., Turner, J., Longo, J., and Gülhan, A., "Key Experiments within the SHEFEX II Mission," Tech. Rep. IAC-08-D2.6.4, DLR, 2008.

[48] Wiliams, S. and Curry, D., "Thermal Protection Materials," NASA Reference Publication 1289, NASA, December 1992.

A

Transformations

Standard frame transformations
The basic frame transformations will be presented [33]. They can be used for the later derivation of the equations of translational motion.

Rotating planetocentric to intertial planetocentric frame
For this transformation only a rotation over the Z-axis is needed. The R-frame rotates with the same speed as the central body, ω_{cb}, as it is attached to it. The transformation matrix then becomes:

$$\mathbb{T}_{I,R} = \mathbb{T}_Z(-\omega_{cb}t) = \begin{bmatrix} \cos\omega_{cb}t & \sin\omega_{cb}t & 0 \\ -\sin\omega_{cb}t & \cos\omega_{cb}t & 0 \\ 0 & 0 & 1 \end{bmatrix} \tag{A.1}$$

Vertical to rotating planetocentric frame
For this transformation a rotation about the Y-axis of the planetocentric latitude, δ, plus $\pi/2$ is needed, as well as a Z-axis rotation of the planetocentric longitude, τ:

$$\mathbb{T}_{R,V} = \mathbb{T}_Z(-\tau)\mathbb{T}_Y(\frac{\pi}{2}+\delta) = \begin{bmatrix} \cos\tau\sin\delta & -\sin\delta & -\cos\tau\cos\delta \\ -\sin\tau\sin\delta & \cos\tau & -\sin\tau\cos\delta \\ \cos\delta & 0 & \sin\delta \end{bmatrix} \tag{A.2}$$

Trajectory to vertical frame The transformation from the trajectory to the vertical frame includes the flight-path angle for airspeed, γ, and the heading angle for airspeed, χ. The transformation matrix is given by:

$$\mathbb{T}_{V,T} = \mathbb{T}_Z(-\chi)\mathbb{T}_Y(-\gamma) = \begin{bmatrix} \cos\chi\cos\gamma & -\sin\chi & \cos\chi\sin\gamma \\ \sin\chi\cos\gamma & \cos\chi & \sin\chi\sin\gamma \\ -\sin\gamma & 0 & \cos\gamma \end{bmatrix} \tag{A.3}$$

Aerodynamic to trajectory frame
The transformation matrix of the aerodynamic to trajectory frame is relatively easy, as only a rotation about the X-axis is needed of the bank angle (σ):

$$\mathbb{T}_{T,A} = \mathbb{T}_X(\sigma) = \begin{bmatrix} 1 & 0 & 0 \\ 0 & \cos\sigma & \sin\sigma \\ 0 & -\sin\sigma & \cos\sigma \end{bmatrix} \tag{A.4}$$

Note that in the trajectory simulation, described in Appendix C, the bank angle σ is assumed to have a value of 0°. Thus the $cos\sigma$ in the matrix will have a value of 1, and the $sin\sigma$ a value of 0.

Aerodynamic to vertical frame
The transformation matrix can be computed from the transformation matrices in Equations (A.3) and (A.4). The resulting matrix is:

$$\mathbb{T}_{V,A} = \mathbb{T}_{V,T}\mathbb{T}_{T,A} = \mathbb{T}_Z(-\chi)\mathbb{T}_Y(-\gamma)\mathbb{T}_X(\sigma) = \begin{bmatrix} \cos\chi\cos\gamma & -\sin\chi\cos\sigma - \sin\gamma\sin\sigma & -\sin\chi\sin\sigma + \cos\chi\sin\gamma\cos\sigma \\ \sin\chi\cos\gamma & \cos\chi\cos\sigma - \sin\chi\sin\gamma\sin\sigma & \cos\chi\sin\sigma + \sin\chi\sin\gamma\cos\sigma \\ -\sin\gamma & -\cos\gamma\sin\sigma & \cos\gamma\cos\sigma \end{bmatrix} \tag{A.5}$$

Note that in the trajectory simulation, described in Appendix C, the bank angle σ is assumed to have a value of 0°. Thus the $cos\sigma$ in the matrix will have a value of 1, and the $sin\sigma$ a value of 0.

Body to aerodynamic frame
This transformation is dictated by the angle of attack (α) and the angle of sideslip (β). They rotate respectively about the Y- and Z-axes:

$$\mathbb{T}_{A,B} = \mathbb{T}_Z(-\beta)\mathbb{T}_Y(-\alpha) = \begin{bmatrix} \cos\alpha\cos\beta & \sin\beta & \sin\alpha\cos\beta \\ -\cos\alpha\sin\beta & \cos\beta & -\sin\alpha\sin\beta \\ -\sin\alpha & 0 & \cos\alpha \end{bmatrix} \tag{A.6}$$

Note that in the trajectory simulation, described in Appendix C, the sideslip angle β is assumed to have a value of 0°. Thus the $cos\beta$ in the matrix will have a value of 1, and the $sin\beta$ a value of 0.

Combined transformation matrices
From the matrices introduced in the previous section, some basic combined transformations can be derived.

Vertical to inertial planetocentric frame
The transformation matrix is a combination of the rotating to intertial planetocentric frame, and vertical to rotating planetocentric frame. In the transformational matrix the celestial longitude, $\tilde{\tau}$, is defined as $\tilde{\tau} = \tau + \omega_{cb}t$.

$$\mathbb{T}_{I,V} = \mathbb{T}_{I,R}\mathbb{T}_{R,V} = \Big|_I \mathbb{T}_Z(-\omega_{cbt})\Big|_R \mathbb{T}_Z(-\tau)\mathbb{T}_Y(\frac{\pi}{2}+\delta)\Big|_V = \begin{bmatrix} -\cos\tilde{\tau}\sin\delta & -\sin\tilde{\tau} & -\cos\tilde{\tau}\cos\delta \\ -\sin\tilde{\tau}\sin\delta & \cos\tilde{\tau} & \sin\tilde{\tau}\cos\delta \\ \cos\delta & 0 & -\sin\delta \end{bmatrix} \tag{A.7}$$

Aerodynamic to rotating planetocentric frame
For this transformation the connection of both frames with the vertical frame is used:

$$\mathbb{T}_{R,A} = \mathbb{T}_{R,V}\mathbb{T}_{V,A} = \Big|_R \mathbb{T}_Z(-\tau)\mathbb{T}_Y(\frac{\pi}{2}+\delta)\Big|_V \mathbb{T}_Z(-\chi)\mathbb{T}_Y(-\gamma)\mathbb{T}_X(\sigma)\Big|_A \tag{A.8}$$

Body to rotating planetocentric frame
The transformation of body to rotating planetocentric frame goes through the vertical and aerodynamic frame:

$$\mathbb{T}_{R,B} = \mathbb{T}_{R,V}\mathbb{T}_{V,A}\mathbb{T}_{A,B} = \Big|_R \mathbb{T}_Z(-\tau)\mathbb{T}_Y(\frac{\pi}{2}+\delta)\Big|_V \mathbb{T}_Z(-\chi)\mathbb{T}_Y(-\gamma)\mathbb{T}_X(\sigma)\Big|_A \mathbb{T}_Z(\beta)\mathbb{T}_Y(-\alpha)\Big|_B \tag{A.9}$$

Bibliography

Mulder, J., van Staveren, W., van der Vaart, J., de Weerdt, E., in 't Veld, A. and Mooij, E., "Flight Dynamics," Lecture Notes, March 2013, AE3202.

B

Aerodynamic Data Aurora

In this appendix the tabulated aerodynamic coefficients of the reference vehicle Aurora are given, which are provided by DLR [1]. First the coefficients are given for the clean vehicle configuration as a function of the angle of attack α and Mach number M. These drag coefficients C_{D_0} are provided in Table B.1, the lift coefficients C_{L_0} in Table B.2 and the moment coefficients C_{m_0} in Table B.3. Thereafter the increments in the moment coefficients ΔC_{m_b} due to wing flap deflection are given for a deflection angle of -45°, -30°, -15°, 15°, 30° and 45 ° in Tables B.4 to B.9.

[1] Private communication, Alexander Kopp, DLR, 2/1/2017

Table B.1: Drag coefficient for the clean configuration Aurora C_{D_0}

M(-), α(°)	0	5	10	15	20	25	30	35	40	45	50	55	60	65	70
4	0.0169	0.0211	0.0398	0.0788	0.1440	0.2392	0.3677	0.5288	0.7195	0.9346	1.1666	1.4064	1.6434	1.8666	2.0656
6	0.0155	0.0181	0.0345	0.0709	0.1335	0.2265	0.3523	0.5108	0.6990	0.9115	1.1409	1.3777	1.6117	1.8315	2.0270
8	0.0148	0.0169	0.0331	0.0696	0.1323	0.2255	0.3513	0.5091	0.6959	0.9061	1.1322	1.3649	1.5942	1.8088	1.9983
10	0.0147	0.0169	0.0340	0.0717	0.1353	0.2287	0.3539	0.5105	0.6960	0.9051	1.1304	1.3620	1.5899	1.8024	1.9897
12	0.0141	0.0170	0.0350	0.0733	0.1371	0.2307	0.3562	0.5137	0.7003	0.9101	1.1354	1.3665	1.5937	1.8052	1.9916
14	0.0141	0.0170	0.0359	0.0756	0.1411	0.2369	0.3653	0.5254	0.7142	0.9252	1.1507	1.3809	1.6060	1.8136	1.9964
16	0.0150	0.0181	0.0385	0.0801	0.1480	0.2464	0.3770	0.5389	0.7284	0.9390	1.1628	1.3893	1.6113	1.8165	1.9969
18	0.0163	0.0198	0.0420	0.0858	0.1560	0.2568	0.3895	0.5530	0.7431	0.9528	1.1746	1.4005	1.6209	1.8233	2.0008
20	0.0179	0.0221	0.0468	0.0936	0.1673	0.2714	0.4071	0.5727	0.7637	0.9732	1.1952	1.4195	1.6376	1.8369	2.0111
22	0.0198	0.0251	0.0531	0.1043	0.1828	0.2916	0.4314	0.5999	0.7920	1.0027	1.2241	1.4471	1.6634	1.8595	2.0292
24	0.0218	0.0287	0.0609	0.1178	0.2022	0.3168	0.4614	0.6327	0.8273	1.0399	1.2625	1.4850	1.6992	1.8904	2.0540
26	0.0262	0.0361	0.0771	0.1454	0.2422	0.3688	0.5232	0.7033	0.9071	1.1264	1.3508	1.5712	1.7797	1.9601	2.1108
28	0.0255	0.0390	0.0865	0.1631	0.2683	0.4039	0.5684	0.7600	0.9721	1.1947	1.4203	1.6387	1.8415	2.0127	2.1513
30	0.0182	0.0309	0.0745	0.1591	0.2691	0.4056	0.5710	0.7611	0.9554	1.1788	1.4078	1.6305	1.8370	2.0116	2.1517

Table B.2: Lift coefficient for the clean configuration Aurora C_{L_0}

M(-), α(°)	0	5	10	15	20	25	30	35	40	45	50	55	60	65	70
4	-0.0047	0.0625	0.1400	0.2365	0.3509	0.4755	0.6046	0.7272	0.8330	0.9133	0.9606	0.9690	0.9355	0.8592	0.7423
6	-0.0070	0.0440	0.1120	0.2032	0.3147	0.4394	0.5683	0.6916	0.7992	0.8818	0.9316	0.9429	0.9124	0.8394	0.7260
8	-0.0078	0.0361	0.1006	0.1903	0.3013	0.4260	0.5550	0.6780	0.7852	0.8672	0.9166	0.9278	0.8976	0.8255	0.7135
10	-0.0080	0.0329	0.0946	0.1831	0.2931	0.4161	0.5431	0.6644	0.7708	0.8532	0.9038	0.9165	0.8879	0.8175	0.7072
12	-0.0077	0.0294	0.0895	0.1757	0.2832	0.4045	0.5309	0.6527	0.7606	0.8441	0.8959	0.9099	0.8826	0.8135	0.7045
14	-0.0077	0.0266	0.0852	0.1707	0.2782	0.4005	0.5286	0.6517	0.7605	0.8445	0.8964	0.9101	0.8823	0.8125	0.7033
16	-0.0079	0.0251	0.0836	0.1697	0.2779	0.4012	0.5297	0.6528	0.7610	0.8441	0.8947	0.9069	0.8788	0.8096	0.7011
18	-0.0079	0.0242	0.0828	0.1691	0.2776	0.4011	0.5296	0.6522	0.7596	0.8413	0.8910	0.9040	0.8765	0.8076	0.6993
20	-0.0079	0.0236	0.0822	0.1685	0.2772	0.4006	0.5287	0.6507	0.7571	0.8382	0.8888	0.9022	0.8748	0.8062	0.6983
22	-0.0079	0.0231	0.0817	0.1680	0.2767	0.4000	0.5278	0.6491	0.7545	0.8365	0.8874	0.9009	0.8737	0.8053	0.6977
24	-0.0078	0.0228	0.0812	0.1675	0.2761	0.3992	0.5265	0.6465	0.7526	0.8349	0.8859	0.8995	0.8727	0.8046	0.6972
26	-0.0078	0.0225	0.0807	0.1670	0.2756	0.3982	0.5245	0.6444	0.7510	0.8335	0.8845	0.8983	0.8716	0.8037	0.6968
28	-0.0078	0.0222	0.0804	0.1667	0.2750	0.3970	0.5222	0.6427	0.7495	0.8317	0.8826	0.8966	0.8700	0.8023	0.6958
30	-0.0078	0.0219	0.0802	0.1664	0.2745	0.3955	0.5212	0.6418	0.7486	0.8304	0.8814	0.8954	0.8689	0.8015	0.6954

Table B.3: Pitch moment coefficient for the clean configuration Aurora C_{m_0}

M(-), α(°)	0	5	10	15	20	25	30	35	40	45	50	55	60	65	70
4	-0.0058	-0.0053	-0.0022	0.0003	0.0022	0.0032	0.0036	0.0034	0.0024	0.0008	-0.0014	-0.0039	-0.0068	-0.0099	-0.0132
6	-0.0055	-0.0029	0.0004	0.0029	0.0045	0.0051	0.0051	0.0043	0.0029	0.0009	-0.0015	-0.0044	-0.0075	-0.0108	-0.0141
8	-0.0053	-0.0019	0.0015	0.0038	0.0052	0.0056	0.0052	0.0040	0.0022	-0.0002	-0.0031	-0.0064	-0.0100	-0.0137	-0.0176
10	-0.0051	-0.0012	0.0020	0.0041	0.0051	0.0051	0.0043	0.0027	0.0005	-0.0022	-0.0053	-0.0087	-0.0124	-0.0162	-0.0201
12	-0.0047	-0.0008	0.0020	0.0037	0.0045	0.0043	0.0033	0.0016	-0.0006	-0.0034	-0.0065	-0.0099	-0.0136	-0.0173	-0.0209
14	-0.0045	-0.0007	0.0020	0.0037	0.0044	0.0042	0.0033	0.0015	-0.0006	-0.0034	-0.0064	-0.0098	-0.0134	-0.0170	-0.0207
16	-0.0046	-0.0006	0.0022	0.0038	0.0045	0.0043	0.0033	0.0014	-0.0008	-0.0037	-0.0068	-0.0102	-0.0139	-0.0176	-0.0213
18	-0.0045	-0.0005	0.0023	0.0039	0.0045	0.0042	0.0031	0.0012	-0.0012	-0.0041	-0.0073	-0.0108	-0.0145	-0.0183	-0.0220
20	-0.0045	-0.0004	0.0023	0.0039	0.0044	0.0040	0.0028	0.0008	-0.0015	-0.0045	-0.0078	-0.0113	-0.0151	-0.0189	-0.0227
22	-0.0044	-0.0003	0.0023	0.0038	0.0043	0.0039	0.0026	0.0006	-0.0019	-0.0049	-0.0082	-0.0118	-0.0156	-0.0195	-0.0233
24	-0.0044	-0.0003	0.0023	0.0038	0.0042	0.0037	0.0024	0.0003	-0.0022	-0.0053	-0.0087	-0.0123	-0.0161	-0.0200	-0.0237
26	-0.0043	-0.0002	0.0023	0.0037	0.0040	0.0035	0.0021	-0.0001	-0.0026	-0.0057	-0.0091	-0.0128	-0.0167	-0.0205	-0.0242
28	-0.0043	-0.0002	0.0023	0.0036	0.0039	0.0033	0.0019	-0.0003	-0.0028	-0.0060	-0.0093	-0.0131	-0.0169	-0.0207	-0.0243
30	-0.0043	-0.0002	0.0023	0.0036	0.0039	0.0033	0.0019	-0.0004	-0.0029	-0.0060	-0.0094	-0.0131	-0.0169	-0.0206	-0.0241

Table B.4: Pitch moment coefficient increment ΔC_{m_b} for a body flap deflection angle of −45°

M(-), α(°)	0	5	10	15	20	25	30	35	40	45	50	55	60	65	70
4	0.0251	0.0229	0.0209	0.0199	0.0201	0.0216	0.0243	0.0282	0.0322	0.0377	0.0432	0.0480	0.0522	0.0554	0.0574
6	0.0241	0.0210	0.0184	0.0171	0.0172	0.0187	0.0216	0.0258	0.0307	0.0365	0.0423	0.0476	0.0521	0.0555	0.0576
8	0.0239	0.0204	0.0176	0.0162	0.0163	0.0178	0.0208	0.0251	0.0305	0.0364	0.0424	0.0480	0.0526	0.0560	0.0581
10	0.0239	0.0202	0.0173	0.0158	0.0159	0.0174	0.0205	0.0248	0.0304	0.0365	0.0427	0.0484	0.0531	0.0565	0.0587
12	0.0239	0.0200	0.0171	0.0156	0.0157	0.0172	0.0203	0.0247	0.0303	0.0365	0.0428	0.0485	0.0532	0.0567	0.0588
14	0.0238	0.0198	0.0169	0.0154	0.0155	0.0170	0.0201	0.0245	0.0301	0.0364	0.0427	0.0485	0.0531	0.0566	0.0587
16	0.0238	0.0198	0.0168	0.0154	0.0154	0.0170	0.0200	0.0244	0.0301	0.0364	0.0428	0.0486	0.0532	0.0567	0.0588
18	0.0238	0.0198	0.0168	0.0153	0.0154	0.0170	0.0200	0.0244	0.0301	0.0365	0.0430	0.0487	0.0534	0.0568	0.0590
20	0.0239	0.0198	0.0168	0.0153	0.0154	0.0169	0.0200	0.0244	0.0301	0.0366	0.0431	0.0488	0.0535	0.0570	0.0592
22	0.0239	0.0198	0.0168	0.0153	0.0154	0.0170	0.0200	0.0245	0.0302	0.0367	0.0432	0.0490	0.0537	0.0572	0.0594
24	0.0240	0.0198	0.0168	0.0153	0.0154	0.0170	0.0200	0.0245	0.0302	0.0368	0.0433	0.0491	0.0538	0.0573	0.0595
26	0.0240	0.0198	0.0168	0.0153	0.0154	0.0170	0.0201	0.0245	0.0303	0.0368	0.0434	0.0492	0.0540	0.0575	0.0597
28	0.0240	0.0198	0.0168	0.0153	0.0154	0.0170	0.0201	0.0245	0.0303	0.0369	0.0434	0.0492	0.0540	0.0575	0.0596
30	0.0240	0.0198	0.0168	0.0153	0.0154	0.0170	0.0200	0.0245	0.0302	0.0368	0.0434	0.0492	0.0539	0.0574	0.0596

Table B.5: Pitch moment coefficient increment ΔC_{m_b} for a body flap deflection angle of −30°

M(-), α(°)	0	5	10	15	20	25	30	35	40	45	50	55	60	65	70
4	0.0162	0.0140	0.0125	0.0124	0.0137	0.0158	0.0197	0.0242	0.0281	0.0323	0.0358	0.0386	0.0405	0.0414	0.0413
6	0.0147	0.0117	0.0098	0.0095	0.0109	0.0138	0.0180	0.0229	0.0277	0.0321	0.0359	0.0388	0.0408	0.0417	0.0416
8	0.0143	0.0109	0.0087	0.0084	0.0099	0.0132	0.0176	0.0227	0.0279	0.0325	0.0363	0.0393	0.0412	0.0422	0.0421
10	0.0141	0.0105	0.0082	0.0079	0.0094	0.0129	0.0175	0.0229	0.0281	0.0328	0.0367	0.0397	0.0416	0.0426	0.0425
12	0.0140	0.0103	0.0079	0.0076	0.0092	0.0126	0.0174	0.0229	0.0282	0.0329	0.0368	0.0398	0.0418	0.0427	0.0426
14	0.0139	0.0101	0.0077	0.0074	0.0090	0.0125	0.0173	0.0228	0.0282	0.0328	0.0367	0.0397	0.0417	0.0426	0.0425
16	0.0139	0.0100	0.0076	0.0073	0.0089	0.0124	0.0173	0.0229	0.0282	0.0329	0.0368	0.0398	0.0418	0.0427	0.0426
18	0.0139	0.0099	0.0076	0.0072	0.0088	0.0123	0.0173	0.0230	0.0283	0.0330	0.0369	0.0399	0.0419	0.0428	0.0427
20	0.0139	0.0099	0.0075	0.0071	0.0088	0.0123	0.0174	0.0230	0.0284	0.0331	0.0370	0.0400	0.0420	0.0430	0.0428
22	0.0139	0.0099	0.0075	0.0071	0.0087	0.0123	0.0174	0.0231	0.0285	0.0332	0.0371	0.0401	0.0422	0.0431	0.0430
24	0.0139	0.0099	0.0075	0.0071	0.0087	0.0123	0.0174	0.0231	0.0286	0.0333	0.0372	0.0403	0.0423	0.0432	0.0431
26	0.0140	0.0099	0.0075	0.0071	0.0087	0.0123	0.0174	0.0232	0.0286	0.0334	0.0373	0.0404	0.0424	0.0433	0.0432
28	0.0140	0.0099	0.0075	0.0071	0.0087	0.0123	0.0175	0.0232	0.0286	0.0334	0.0373	0.0404	0.0424	0.0433	0.0432
30	0.0140	0.0098	0.0074	0.0071	0.0087	0.0123	0.0174	0.0232	0.0286	0.0334	0.0373	0.0403	0.0423	0.0433	0.0431

Table B.6: Pitch moment coefficient increment ΔC_{m_b} for a body flap deflection angle of −15°

M(-), α(°)	0	5	10	15	20	25	30	35	40	45	50	55	60	65	70
4	0.0063	0.0058	0.0059	0.0067	0.0086	0.0108	0.0133	0.0157	0.0178	0.0194	0.0206	0.0212	0.0213	0.0208	0.0198
6	0.0048	0.0038	0.0039	0.0052	0.0075	0.0103	0.0131	0.0157	0.0179	0.0196	0.0208	0.0214	0.0215	0.0210	0.0200
8	0.0041	0.0029	0.0031	0.0046	0.0072	0.0103	0.0133	0.0159	0.0181	0.0198	0.0211	0.0217	0.0218	0.0213	0.0202
10	0.0039	0.0024	0.0026	0.0044	0.0072	0.0104	0.0134	0.0161	0.0183	0.0201	0.0213	0.0219	0.0220	0.0215	0.0204
12	0.0037	0.0021	0.0023	0.0042	0.0072	0.0104	0.0134	0.0161	0.0184	0.0201	0.0213	0.0220	0.0221	0.0215	0.0204
14	0.0036	0.0019	0.0021	0.0041	0.0072	0.0104	0.0134	0.0161	0.0183	0.0201	0.0213	0.0220	0.0220	0.0215	0.0204
16	0.0035	0.0018	0.0020	0.0041	0.0072	0.0105	0.0135	0.0161	0.0184	0.0201	0.0214	0.0220	0.0221	0.0215	0.0204
18	0.0035	0.0017	0.0019	0.0040	0.0072	0.0105	0.0135	0.0162	0.0184	0.0202	0.0214	0.0221	0.0221	0.0216	0.0205
20	0.0034	0.0016	0.0018	0.0040	0.0072	0.0105	0.0135	0.0162	0.0185	0.0203	0.0215	0.0221	0.0222	0.0217	0.0206
22	0.0034	0.0016	0.0018	0.0040	0.0072	0.0105	0.0136	0.0163	0.0185	0.0203	0.0216	0.0222	0.0223	0.0217	0.0206
24	0.0034	0.0015	0.0018	0.0040	0.0073	0.0106	0.0136	0.0163	0.0186	0.0204	0.0216	0.0223	0.0223	0.0218	0.0207
26	0.0034	0.0015	0.0017	0.0040	0.0073	0.0106	0.0137	0.0164	0.0186	0.0204	0.0217	0.0223	0.0224	0.0218	0.0207
28	0.0034	0.0015	0.0017	0.0040	0.0073	0.0106	0.0137	0.0164	0.0186	0.0204	0.0217	0.0223	0.0224	0.0218	0.0207
30	0.0034	0.0015	0.0017	0.0040	0.0073	0.0106	0.0137	0.0164	0.0186	0.0204	0.0216	0.0223	0.0224	0.0218	0.0207

Table B.7: Pitch moment coefficient increment ΔC_{m_b} for a body flap deflection angle of 15°

M(-), α(°)	0	5	10	15	20	25	30	35	40	45	50	55	60	65	70
4	-0.0068	-0.0084	-0.0107	-0.0131	-0.0153	-0.0172	-0.0185	-0.0194	-0.0197	-0.0194	-0.0185	-0.0171	-0.0151	-0.0127	-0.0100
6	-0.0053	-0.0075	-0.0103	-0.0130	-0.0154	-0.0174	-0.0188	-0.0197	-0.0200	-0.0197	-0.0188	-0.0173	-0.0153	-0.0129	-0.0101
8	-0.0047	-0.0073	-0.0104	-0.0132	-0.0157	-0.0177	-0.0191	-0.0200	-0.0203	-0.0200	-0.0190	-0.0175	-0.0155	-0.0131	-0.0102
10	-0.0044	-0.0073	-0.0105	-0.0134	-0.0158	-0.0179	-0.0193	-0.0202	-0.0205	-0.0202	-0.0192	-0.0177	-0.0157	-0.0132	-0.0103
12	-0.0043	-0.0073	-0.0105	-0.0134	-0.0159	-0.0179	-0.0194	-0.0203	-0.0206	-0.0202	-0.0193	-0.0178	-0.0157	-0.0132	-0.0103
14	-0.0042	-0.0073	-0.0105	-0.0134	-0.0159	-0.0179	-0.0194	-0.0203	-0.0205	-0.0202	-0.0193	-0.0177	-0.0157	-0.0132	-0.0103
16	-0.0041	-0.0073	-0.0105	-0.0134	-0.0159	-0.0180	-0.0194	-0.0203	-0.0206	-0.0202	-0.0193	-0.0178	-0.0157	-0.0132	-0.0104
18	-0.0041	-0.0073	-0.0106	-0.0135	-0.0160	-0.0180	-0.0195	-0.0204	-0.0206	-0.0203	-0.0194	-0.0178	-0.0158	-0.0133	-0.0104
20	-0.0041	-0.0073	-0.0106	-0.0135	-0.0160	-0.0181	-0.0195	-0.0204	-0.0207	-0.0204	-0.0194	-0.0179	-0.0158	-0.0133	-0.0104
22	-0.0041	-0.0073	-0.0106	-0.0136	-0.0161	-0.0181	-0.0196	-0.0205	-0.0208	-0.0204	-0.0195	-0.0180	-0.0159	-0.0134	-0.0105
24	-0.0041	-0.0074	-0.0107	-0.0136	-0.0161	-0.0182	-0.0197	-0.0206	-0.0208	-0.0205	-0.0195	-0.0180	-0.0159	-0.0134	-0.0105
26	-0.0041	-0.0074	-0.0107	-0.0136	-0.0162	-0.0182	-0.0197	-0.0206	-0.0209	-0.0205	-0.0196	-0.0181	-0.0160	-0.0134	-0.0105
28	-0.0041	-0.0074	-0.0107	-0.0137	-0.0162	-0.0182	-0.0197	-0.0206	-0.0209	-0.0205	-0.0196	-0.0180	-0.0160	-0.0134	-0.0105
30	-0.0041	-0.0074	-0.0107	-0.0137	-0.0162	-0.0182	-0.0197	-0.0206	-0.0209	-0.0205	-0.0196	-0.0180	-0.0160	-0.0134	-0.0105

Table B.8: Pitch moment coefficient increment ΔC_{m_b} for a body flap deflection angle of 30°

M(-), α(°)	0	5	10	15	20	25	30	35	40	45	50	55	60	65	70
4	-0.0190	-0.0225	-0.0263	-0.0297	-0.0323	-0.0341	-0.0347	-0.0344	-0.0329	-0.0303	-0.0268	-0.0225	-0.0173	-0.0116	-0.0055
6	-0.0175	-0.0218	-0.0262	-0.0300	-0.0328	-0.0347	-0.0354	-0.0350	-0.0335	-0.0309	-0.0274	-0.0229	-0.0177	-0.0119	-0.0057
8	-0.0171	-0.0218	-0.0265	-0.0304	-0.0334	-0.0352	-0.0360	-0.0356	-0.0340	-0.0314	-0.0277	-0.0232	-0.0180	-0.0121	-0.0058
10	-0.0170	-0.0220	-0.0268	-0.0308	-0.0338	-0.0356	-0.0364	-0.0359	-0.0344	-0.0317	-0.0280	-0.0235	-0.0181	-0.0122	-0.0059
12	-0.0169	-0.0221	-0.0270	-0.0309	-0.0339	-0.0358	-0.0365	-0.0361	-0.0345	-0.0318	-0.0281	-0.0235	-0.0182	-0.0123	-0.0059
14	-0.0168	-0.0221	-0.0269	-0.0309	-0.0339	-0.0357	-0.0365	-0.0360	-0.0344	-0.0318	-0.0281	-0.0235	-0.0182	-0.0122	-0.0059
16	-0.0168	-0.0221	-0.0270	-0.0310	-0.0340	-0.0358	-0.0366	-0.0361	-0.0345	-0.0318	-0.0282	-0.0236	-0.0182	-0.0123	-0.0059
18	-0.0168	-0.0222	-0.0271	-0.0311	-0.0341	-0.0359	-0.0367	-0.0362	-0.0346	-0.0319	-0.0282	-0.0236	-0.0183	-0.0123	-0.0059
20	-0.0169	-0.0223	-0.0272	-0.0312	-0.0342	-0.0361	-0.0368	-0.0363	-0.0347	-0.0321	-0.0283	-0.0237	-0.0183	-0.0123	-0.0059
22	-0.0169	-0.0223	-0.0273	-0.0313	-0.0343	-0.0362	-0.0369	-0.0365	-0.0349	-0.0322	-0.0284	-0.0238	-0.0184	-0.0124	-0.0060
24	-0.0169	-0.0224	-0.0274	-0.0314	-0.0344	-0.0363	-0.0370	-0.0366	-0.0350	-0.0322	-0.0285	-0.0239	-0.0185	-0.0124	-0.0060
26	-0.0170	-0.0225	-0.0274	-0.0315	-0.0345	-0.0364	-0.0371	-0.0367	-0.0350	-0.0323	-0.0286	-0.0239	-0.0185	-0.0125	-0.0060
28	-0.0170	-0.0225	-0.0274	-0.0315	-0.0345	-0.0364	-0.0371	-0.0366	-0.0350	-0.0323	-0.0286	-0.0239	-0.0185	-0.0124	-0.0060
30	-0.0169	-0.0225	-0.0274	-0.0315	-0.0345	-0.0363	-0.0371	-0.0366	-0.0350	-0.0323	-0.0285	-0.0239	-0.0185	-0.0124	-0.0060

Table B.9: Pitch moment coefficient increment ΔC_{m_b} for a body flap deflection angle of 45°

M(-), α(°)	0	5	10	15	20	25	30	35	40	45	50	55	60	65	70
4	-0.0325	-0.0359	-0.0392	-0.0416	-0.0427	-0.0424	-0.0407	-0.0376	-0.0332	-0.0276	-0.0210	-0.0135	-0.0055	0.0030	0.0115
6	-0.0313	-0.0357	-0.0396	-0.0423	-0.0436	-0.0434	-0.0417	-0.0385	-0.0341	-0.0284	-0.0216	-0.0140	-0.0058	0.0027	0.0114
8	-0.0313	-0.0360	-0.0401	-0.0430	-0.0443	-0.0441	-0.0424	-0.0392	-0.0346	-0.0288	-0.0220	-0.0143	-0.0060	0.0027	0.0114
10	-0.0314	-0.0364	-0.0406	-0.0435	-0.0448	-0.0446	-0.0429	-0.0396	-0.0350	-0.0292	-0.0222	-0.0145	-0.0061	0.0027	0.0115
12	-0.0314	-0.0365	-0.0408	-0.0437	-0.0450	-0.0448	-0.0430	-0.0398	-0.0351	-0.0293	-0.0223	-0.0145	-0.0061	0.0027	0.0115
14	-0.0313	-0.0365	-0.0408	-0.0436	-0.0450	-0.0447	-0.0430	-0.0397	-0.0351	-0.0292	-0.0223	-0.0145	-0.0061	0.0026	0.0115
16	-0.0313	-0.0366	-0.0409	-0.0438	-0.0451	-0.0449	-0.0431	-0.0398	-0.0352	-0.0293	-0.0224	-0.0146	-0.0061	0.0026	0.0115
18	-0.0314	-0.0367	-0.0410	-0.0439	-0.0452	-0.0450	-0.0432	-0.0400	-0.0353	-0.0294	-0.0224	-0.0146	-0.0062	0.0026	0.0116
20	-0.0314	-0.0368	-0.0412	-0.0441	-0.0454	-0.0452	-0.0434	-0.0401	-0.0354	-0.0295	-0.0225	-0.0147	-0.0062	0.0026	0.0116
22	-0.0315	-0.0370	-0.0413	-0.0442	-0.0455	-0.0453	-0.0435	-0.0402	-0.0356	-0.0296	-0.0226	-0.0147	-0.0062	0.0026	0.0116
24	-0.0316	-0.0371	-0.0414	-0.0443	-0.0457	-0.0454	-0.0437	-0.0404	-0.0357	-0.0297	-0.0227	-0.0148	-0.0062	0.0026	0.0117
26	-0.0316	-0.0371	-0.0415	-0.0444	-0.0458	-0.0456	-0.0438	-0.0405	-0.0357	-0.0298	-0.0227	-0.0148	-0.0063	0.0027	0.0117
28	-0.0316	-0.0372	-0.0415	-0.0444	-0.0458	-0.0456	-0.0437	-0.0404	-0.0357	-0.0298	-0.0227	-0.0148	-0.0063	0.0027	0.0117
30	-0.0316	-0.0371	-0.0415	-0.0444	-0.0457	-0.0455	-0.0437	-0.0404	-0.0357	-0.0297	-0.0227	-0.0148	-0.0062	0.0027	0.0117

C

Trajectory Simulation

A simulation of the trajectory of the vehicle is made, for the re-entry phase. The re-entry phase is taken into account as the vehicle configuration of Aurora that is considered is the rocket propulsion based version, Aurora-R. For this propulsion type the heat loads are largest during re-entry. The programming of the model is done in the TUDAT environment, which is C++ based. The main design choices applied to the model are presented in Section C.1.1. Hereafter, in Section C.1 the architectural design of the software is stated. Both for the entire model and the most important sub-modules. Section C.2 describes the implementation of the architectural design on the TUDAT software. Finally the verification of the trajectory simulation is given in Section C.3, in which also the outcome of the nominal trajectory is presented.

The trajectory simulation is made to follow a pre-determined angle of attack profile, that must be provided as an input as a function of time. This angle of attack profile is provided by DLR. The added value of the TUDAT simulation is the possibility to analyze the trajectory in the TU Delft environment, as well to possibly add small variations to the trajectory to discover the effect of these changes on the heat loads and TPS. The creation of a stand-alone simulation was thought to be too time consuming and therefore out of the scope of this thesis.

C.1. Architectural Design Software

For the trajectory simulation an architectural design was made, to map all functions that need to be performed in the simulation and their connections. The complete trajectory simulation is mapped in a flowchart. The separate modules each have their own architectural design, with more detail. Subsections C.1.2 to C.1.6 give elaborations on their respective modules. The complete overview of the trajectory simulation is given in C.1.7.

C.1.1. Main Design Choices

The main design choices made in the development of the trajectory simulator are stated here. The main objective of the thesis is the development of an optimization tool for the TPS of a space plane. With this objective in mind choices were made regarding the extent of the complexity of the model, aiming to take into account all parameters that have a significant effect on the TPS design, whilst not over-complicating the model by adding complexities that do not affect the TPS.

Environment

- The gravitational field is central with an added J_2-term.
- The atmospheric model used is the US76.
- The Earth is modeled as a spheroid.

Flight dynamics

- No third body perturbations are taken into account.
- No wind is taken into account.
- The sideslip angle β and bank angle σ have a constant value of 0°.

- Only translational motion is taken into account, with an application of the trim condition. Rotational motion is neglected.

Vehicle

- The Aurora-R vehicle is used as the nominal reference vehicle.
- The aerodynamic coefficient tables are generated for the reference vehicle and provided by DLR.
- Only the aerodynamic moment coefficients are taken into account to achieve the trim condition, other moments are assumed to be zero.
- Only trim wing flap deflections are taken into account.

C.1.2. Environment Module

The environmental module needs the initial state as an input in spherical components. Therefore the first step is to convert the cartesian components to spherical. The spherical position is used as an input to determine the spherical harmonic gravitational field, including the J_2-term. From the distance to Earth's center the spherical Earth shape can be established. The atmospheric conditions depend solely on the altitude of the vehicle, which is an output of the Earth shape. The Mach number of the vehicle is a function of the atmospheric condition speed of sound, a, and the vehicles velocity V. The dynamic pressure is determined from V and the density of the local atmosphere, ρ.

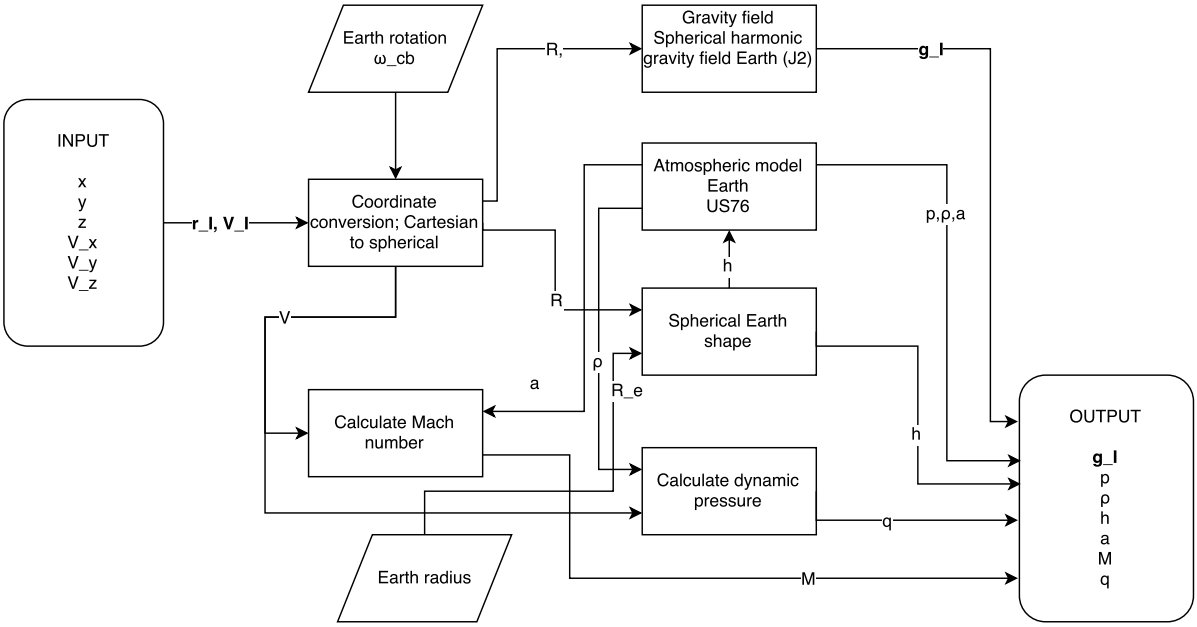

Figure C.1: Architectural design of the environment module

C.1.3. External Forces Module

The two main external forces the vehicle is subjected to in the entry phase are the gravitational force and the aerodynamic force. The first is dependent of the gravitational acceleration $\mathbf{g_v}$, resulting from the environmental module, and the vehicles mass. The latter depends on the vehicles lift and drag coefficient, and the dynamic pressure.

All forces are originally determined in a reference frame other than the inertial frame. Therefore, frame transformations need to be performed to express all forces in the inertial frame. The the aerodynamic force must be converged from the aerodynamic frame, and the thrust force from the propulsion frame. More information on the different frames and their transformations is provided in Section 3.1. The actual transformations are stated in Appendix A. The gravitational force is already given in the inertial frame and thus does not need a transformation.

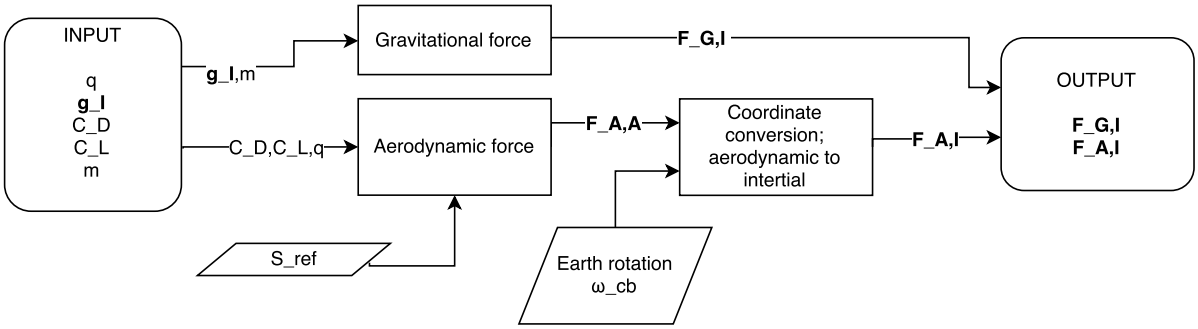

Figure C.2: Architectural design of the external forces module

C.1.4. Vehicle Model Module

In the vehicle model module the aerodynamic coefficients C_D, C_L and C_m of the vehicle are determined for the current α, M and wing flap deflection angle δ_b coming from respectively the environment and guidance module. The module is depicted in Figure C.3. The coefficients for the entire vehicle are provided as a function of α and M by DLR. The increments caused by the wing flap deflection are also a function of δ_b. With both the vehicle coefficients and the bodyflap increments determined, the total coefficients can be calculated. Note that the side force is present in the figure, however, as stated in Section C.1.1, this force is assumed to be zero.

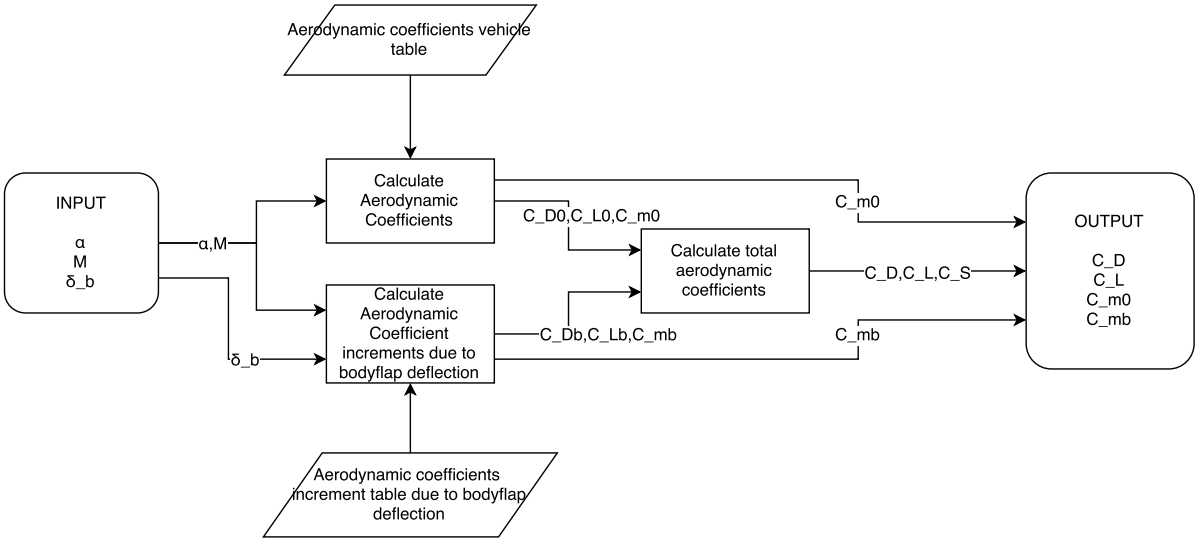

Figure C.3: Architectural design of the vehicle model module

C.1.5. Guidance and Control Module

The guidance and control module has two main functions; to follow a predetermined angle of attack profile (provided by DLR) and to maintain the trimmed condition. For the first task desired α is determined as a function of time. The guidance than sets the commanded angle of attack α_c. The control module enforces the commanded angle to become the actual angle of attack α. Note that even though the sideslip and bank angle are included in the figure, their values are determined to be constant at zero, as was stated in Section C.1.1.

The wing flap deflection is determined by the trim condition. The moment coefficient increment caused by the flap deflection C_{m_b} should be equal to the nominal coefficient C_{m_0}.

C.1.6. Equations of Motion Module

The equations of motion that determine the flight of the vehicle were previously discussed in Section 3.5. Figure C.5 shows the architectural design of the equations of motion. Only translational motion is taken into

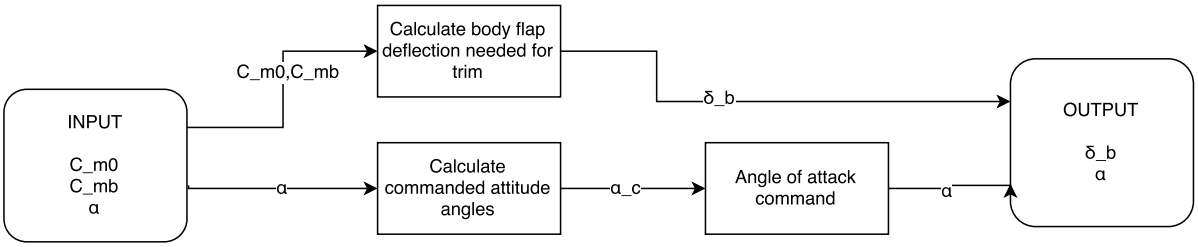

Figure C.4: Architectural design of the guidance and control module

account. They are a function of the previous position of the vehicle, the mass m, the forces acting on the vehicle $\mathbf{F_I}$ and the time t. Integrating the outcomes of the equations of motion $d\mathbf{V}/dt$, $d\mathbf{r}/dt$ and dm/dt provides the new position and velocity vectors $\mathbf{r_I}$ and $\mathbf{V_I}$ and the new mass. For the entry phase obviously the mass remains at a constant value.

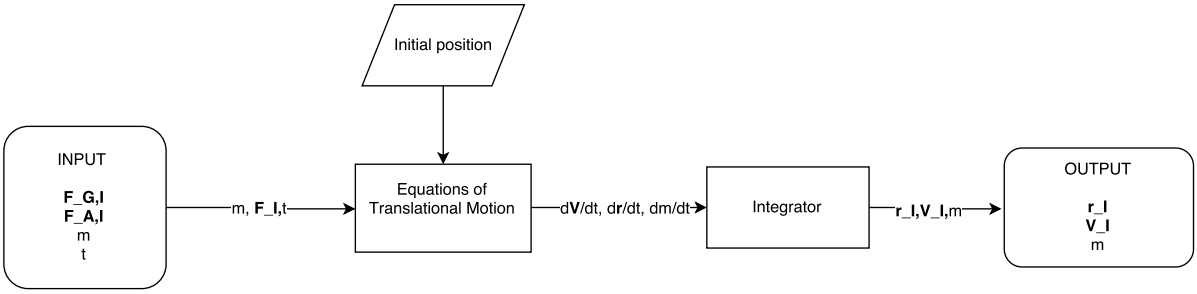

Figure C.5: Architectural design of the equations of motion module

C.1.7. Complete Trajectory Simulation Design

The flowchart showing the complete trajectory simulation scheme is depicted in Figure C.6. The input represented by the initial state consists of the initial position $\mathbf{r_{I_0}}$ ($[x_{I_0}, y_{I_0}, z_{I_0}]$), initial velocity $\mathbf{V_{I_0}}$ ($[\dot{x}_{I_0}, \dot{y}_{I_0}, \dot{z}_{I_0}]$), the initial mass m_0 and initial orientation angles α_0, σ_0 and β_0. With the equations of motion, see Section 3.5, the new state is determined for every propagation step. When ideal control is implemented, the angle of attack is determined by the guidance and control module. Except for the first step, where the attitude comes from the equations of motion, this is the case. The environmental conditions are based on the position and velocity vectors. The environmental outputs form the basis to the different forces the vehicle is subjected to; the gravitational force $\mathbf{F_G}$ and the aerodynamic force $\mathbf{F_A}$. The vehicle aerodynamic coefficients are a function of α, M and the wing flap deflection δ_b.

The complete trajectory architectural design is applicable to both the ascent as the reentry phase. However, one must notice that in the reentry phase the trust force is equal to zero, and the fuel mass flow $\dot{m}_f$ is also zero, hence the vehicle mass is constant.

C.2. TUDAT

The trajectory simulation is modeled within the C++ based TUDAT environment. An elaboration is given on the choices made for the trajectory simulation, within TUDAT. The environment, vehicle, accelerations and propagation settings are discussed.

C.2.1. Environment

As was seen in Subsection C.1.2 the environment modeling consists of a gravity field, atmospheric model and Earth shape. The Earth is assumed to be spherical, with its radius taken as the mean radius of Earth. The atmospheric model used is 1976 US Standard Atmosphere. A central gravity field with an added J_2-term is applied. Furthermore, in TUDAT ephemeris settings are specified. It is chosen to use a constant ephemeris, as this is deemed valid for the relatively short reentry or ascent phase.

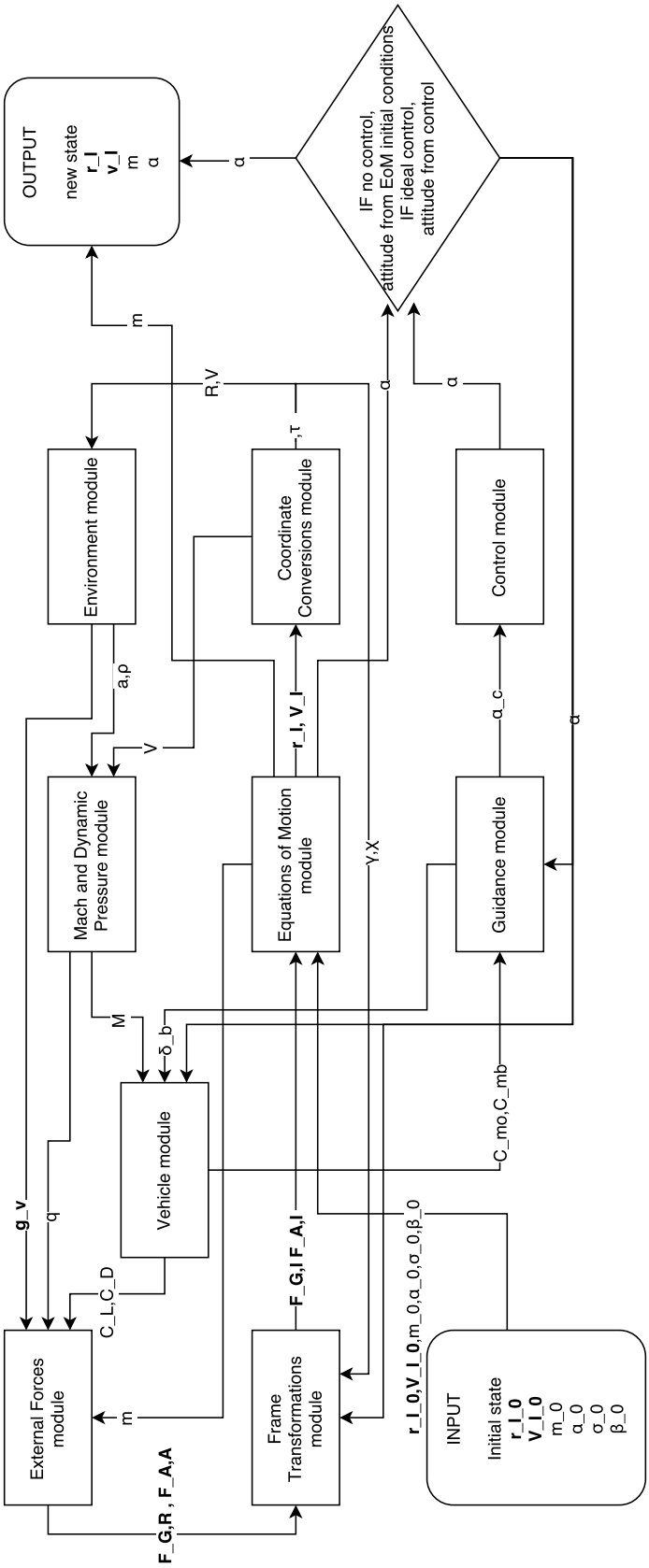

Figure C.6: Architectural design of the complete trajectory simulation

Two bodies are taken into account for the environment; Earth and the vehicle, thus Aurora. Because in reentry and ascent the vehicle is close to Earth, it is assumed that third body accelerations can be neglected.

C.2.2. Accelerations

When the reentry phase is considered, the accelerations, or external forces as defined in Subsection C.1.3, consist of a gravitational and an aerodynamic force. For the gravitational force spherical harmonics are chosen, with a maximum order of 2 and a minimum order of 0. Thus taking into account J_2. The aerodynamic force is determined by five things; the atmosphere the vehicle is in, the shape of the central body, the aerodynamic data of the vehicle (in the case of Aurora provided as aerodynamic coefficient tables dependent on M and α), the mass model of the vehicle (for the reentry phase constant mass is assumed for Aurora), and finally the current state of the vehicle and central body.

C.2.3. Guidance and Trim

As an input for the desired trajectory an angle of attack profile (over time) is provided by DLR. This angle of attack profile is forced upon the trajectory simulation, thus for every time step the angle of attack is determined with interpolation. This angle is enforced on the trajectory through the aerodynamic guidance. As the system has three degrees of freedom, and is trimmed, both the bank angle and the angle of sideslip have a constant value of 0°.

Trim is also regulated within the guidance module. To reach trim the moment coefficient resulting from the wing flaps deflections ΔC_{m_b} has to be equal to the negative moment coefficient of the vehicle without wing flap deflection C_{m_0};

$$\Delta C_{m_b} = -C_{m_0} \tag{C.1}$$

When this condition is reached the total pitch moment of the vehicle is zero and thus the vehicle is trimmed. The moment coefficient resulting from the wing flap deflection is a function of the Mach number, angle of attack and the deflection angle. As input DLR has provided the moment coefficients as a function of Mach number and angle of attack, for a deflection angle of −45°, −30°, −15°, 0°, 15°, 30° and 45°. The coefficient tables are included in Appendix B. By performing two interpolations -the first for the current combination of mach number and angle of attack, the second over the resulting coefficients for the different input deflection angles- the deflection angle is found which will nullify the moment. This way the deflection angle is determined at every time step of the propagation.

C.2.4. Propagation Settings

TUDAT can be used to propagate both the translational dynamics and the mass. As the reentry phase is simulated the mass is constant and thus needs no propagation. Propagation in this is defined as the formulation of differential equations that define the time-evolution of the dynamic[1]. The initial state input must be defined in Cartesian coordinates with respect to the central body in the propagation. The initial state is given in spherical coordinates, which are then transformed into Cartesian coordinates. The parameters that define the initial state are the radius $R_E + 120$ km, latitude 0 deg, longitude 0 deg, velocity 7.41 km/s, flight path angle −0.8079 deg and heading angle 0 deg. In the propagation use is made of the RK4 integrator, which was introduced in Chapter 6. The integrator represents the scheme used to give a numerical solution to the differential equations defined by the propagator. The step size is fixed for the RK4 integrator and is 1 s. The propagation goes from an epoch of 0 to 3000 s. There is one termination condition, at an altitude of 10 km for the reentry phase.

Three settings have to be defined in the propagation. The first is if the orbit is to be propagated immediately upon creation of the object. It is set to yes, as there are no modifications needed before propagation. The second is whether the numerical solution should be deleted after the integration and processing steps. It is set to false. The third setting defines if the ephemeris settings should be reset for the new numerical result. As a constant ephemeris is used in the simulation at hand this is also set to false.

[1] http://tudat.tudelft.nl/projects/tudat, visited on 31/08/2016

C.3. Verification & Validation

The various functions performed within the trajectory simulation must be verified, to ensure that the intended steps are taken. Also the interaction between different trajectory simulation modules needs to be verified. Furthermore the trajectory simulation must be validated, to confirm that the results coming from the simulation are valid. These respective checks will be performed in the following subsections. During the verification and validation process multiple deficiencies came to light which were corrected accordingly.

C.3.1. Module Verification

Many modules and functions are already provided by the TUDAT software, and are therefore considered verified. Acceptance tests were performed to ensure the proper working of the software on the system at hand. In this section the added functions and interfaces will be discussed for the verification process. The verified parts will be discussed per module.

Environmental module
The environmental properties and their application (gravitational model, atmospheric model and spherical Earth shape) are implemented functions in the TUDAT software and as such already verified. A check was performed to ensure that the selected environmental models were justly selected.

External forces module
The computation of the external forces, the gravitational and aerodynamic force, is done by an existing function in TUDAT. This function has already been verified.

Vehicle model module
In the vehicle model module the right aerodynamic coefficients for lift, drag, and moment have to be selected from the input coefficient tables. Furthermore the right aerodynamic coefficient increments resulting from the body flap deflection have to be selected. The reading and selection of the aerodynamic data was verified by manually checking the selected data with the input table data. Furthermore the interpolation between the values was verified by comparing interpolated values with the results from the interpolated values for the same input variables (M and α) created in Matlab.

Guidance and control module
The first added function in the guidance and control module is the reading in and following of a predefined angle of attack profile, as a function of the altitude. It was manually checked that the data was read in from the file correctly. Furthermore the interpolation function was verified, by comparing the results for arbitrary altitudes with results from Matlab interpolation. The resulting α profile was verified by comparing it to the input profile.

The second added function in the trajectory simulation is the trim condition. Firstly the trim tables have to be read in correctly. This was manually checked. Secondly interpolation is performed based on the current M and α. Finally another interpolation is performed between the input pitch angles, based on the desired ΔC_{m_b}. These interpolation procedures were checked with both back-of-the-envelope calculations and interpolations performed in Matlab, and found to match. Lastly it was verified that the correct C_m resulted from the trim condition, by ensuring the moment coefficient was zero.

Equations of motion and frame transformations module
The equations of motions are already present in the TUDAT software, and as such already verified. The same is true for the frame transformations. However, it was checked that the frame transformations were applied at the right points in the trajectory simulation.

C.3.2. Validation Reentry Trajectory

To validate the trajectory simulation the resulting trajectory is compared to a trajectory with the same initial conditions provided by DLR. The reference vehicle Aurora is considered for this trajectory. The aerodynamic coefficient data of Aurora which was an input for both simulations is stated in Appendix B. The same gravitational model is used, as well as the same Earth shape. However, the atmospheric model both simulations use is different. The TUDAT trajectory uses the US76 atmosphere, whereas the TOSCA simulation uses a polyno-

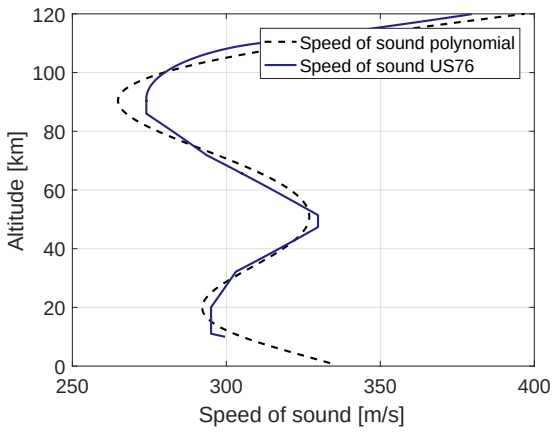

Figure C.7: Speed of sound over altitude profile for the polynomial approximation used by the DLR trajectory simulation and the US76 atmosphere used by the TUDAT trajectory simulation

mial atmosphere approximation. The speed of sound curves resulting from both models are displayed over altitude in Figure C.7. While the polynomial does follow the same curve trend as the US76 atmosphere, it can clearly be seen that there are some discrepancies. These will have an influence on the results of the comparison of the trajectories, as the Mach number M is dependent on the speed of sound (see Equation (3.15)). The aerodynamic coefficients of the vehicle are dependent on the Mach number. The validation reference trajectory is equal to the nominal trajectory that is taken to compute the TPS design in the thesis work. It is the reentry trajectory of Aurora. The starting altitude is equal to 120 km. The time goes from starting time 0 s to 3000 s. The simulated trajectory is set to terminate at an altitude of 10 km. The initial longitude and latitude values are 0.0°, the flightpath angle −0.81° and the heading angle 90.0°.

Figures C.8 to C.17 show the results of the validation. From Figure C.15 it can be seen that the angle of attack profile coincides perfectly with the profile of the reference trajectory. This is logical as this trajectory was an input for the simulated trajectory. From the figures showing the trajectory of Aurora, mainly Figures C.8, C.10, C.16 and C.17 it can be seen that there are some discrepancies with the reference trajectory. The first part of the trajectory coincides well, but after time an error arises which grows over time. It is thought that this error originates in the difference in atmospheric models, which was described earlier in this section. The difference in atmospheric models leads to an error in the resulting Mach number, plotted in Figure C.9. M is dependent on both the speed of sound and relative velocity. The latter is plotted over the altitude in Figure C.14. It is clear that the airspeed almost perfectly coincides with the reference data, only minor discrepancies are visible. The aerodynamic coefficients are a function of Mach number and angle of attack, thus a discrepancy also arises in the coefficients due to M. These are displayed for lift and drag in Figure C.11 and for the moment in Figure C.12. It can be seen that the discrepancies in C_L and C_D are minor. However, small changes will build up in the trajectory, leading to the relatively larger errors towards the end of the trajectory. This can also be seen in the moment coefficient. At first the coefficient coincides with the reference trajectory, but towards the end an increasing error arises. The same behavior is visible for the deflection angle, Figure C.13, which makes sense as the body flap is angles in such a way to achieve a trimmed condition with a total C_m of zero.

The differences between the reference and simulated trajectory simulations can be explained by the difference in atmospheric models. However, it cannot be concluded that the error exclusively originates from this difference. More tests need to be performed to find if their are more errors present. It is thought though that the atmospheric model difference is the main source of the discrepancies, as it is a major known difference between the models. For the first part of the trajectory all parameters coincide sufficiently. Towards the final part of the trajectory discrepancies grow, resulting in a different trajectory.

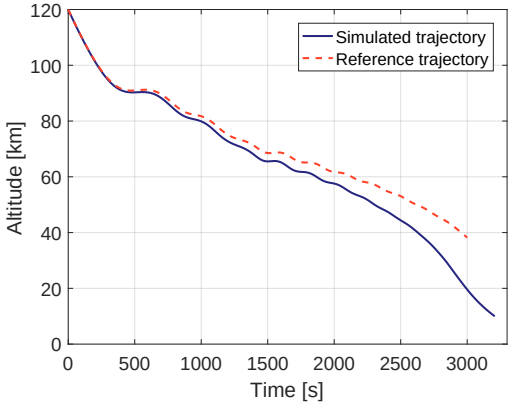

Figure C.8: Altitude over time

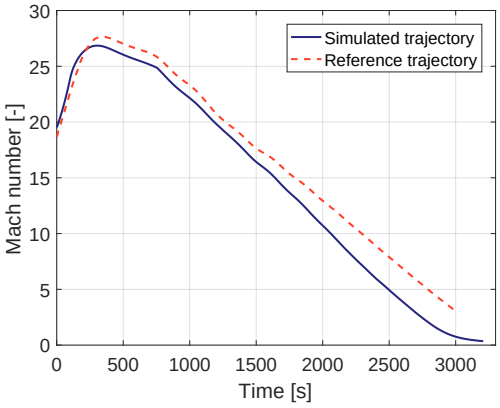

Figure C.9: Mach number over time

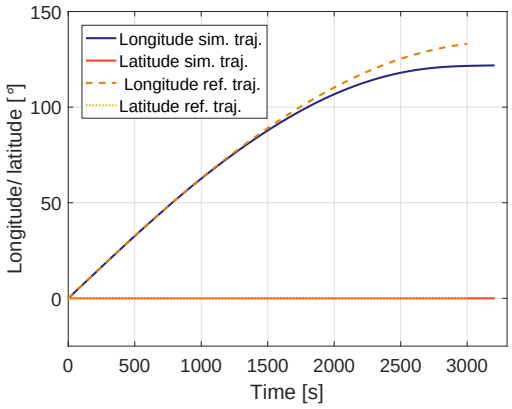

Figure C.10: Longitude and latitude over time

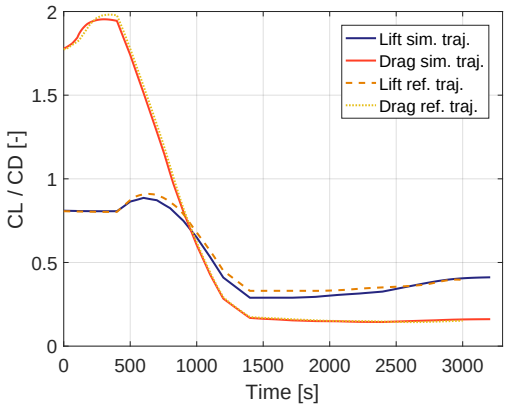

Figure C.11: Lift and drag coefficient over time

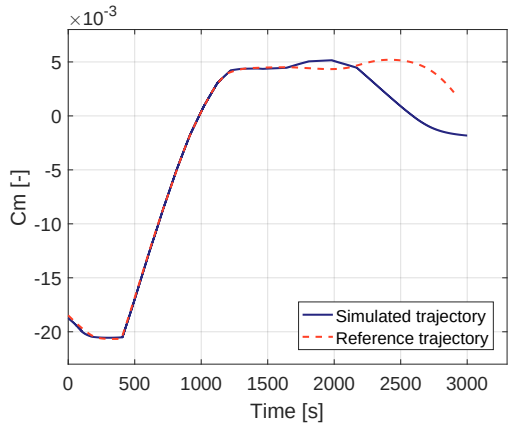

Figure C.12: Moment coefficient over time

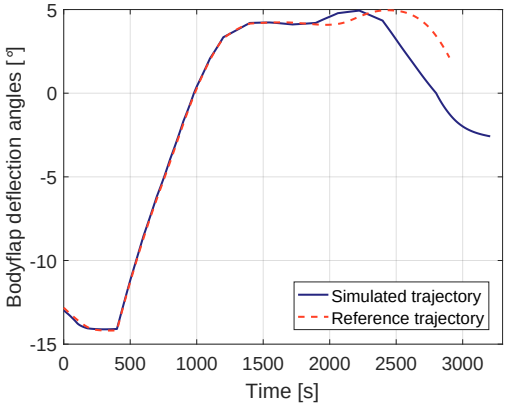

Figure C.13: Bodyflap deflection angle over time

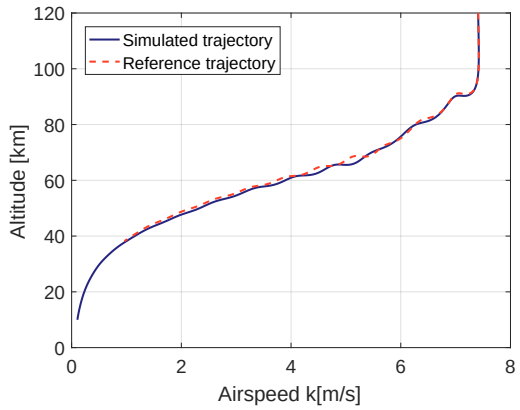

Figure C.14: Velocity over altitude

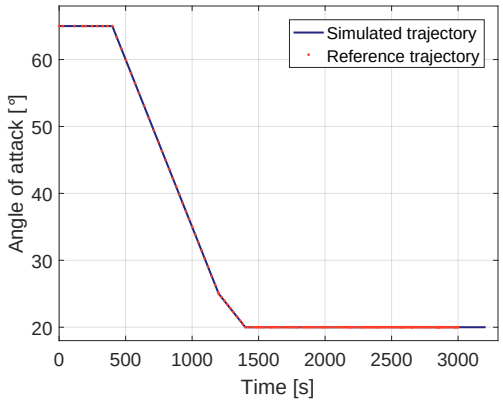

Figure C.15: Angle of attack over time

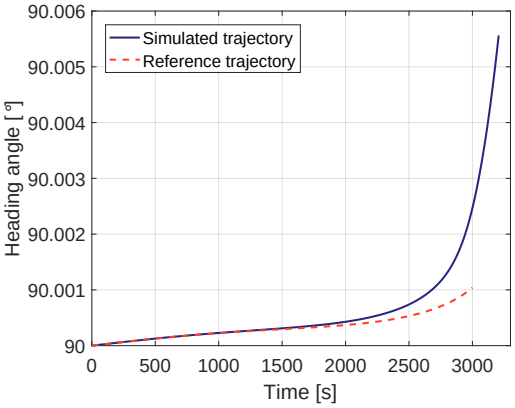

Figure C.16: Heading angle over time

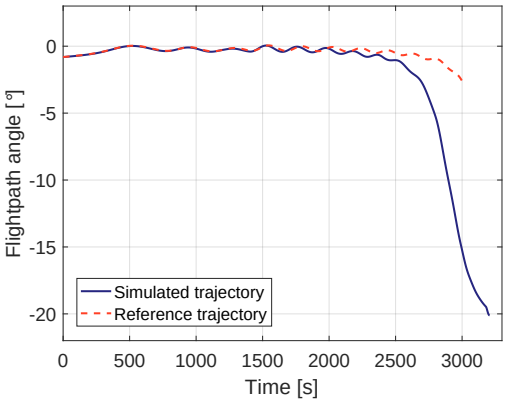

Figure C.17: Flightpath angle over time

D

Finite Element Model Aurora

In this appendix additional views of the FEM of Aurora are provided. One must keep in mind that the FEM of Aurora consists of half the vehicle, as it is symmetrically shaped. The front view of Aurora is provided in Figure D.1, here the front shape of the wing can be clearly seen, as well as the circular shape of the upper half of the fuselage, and the flat bottom. A side view of Aurora is given in Figure D.2. From this figure the curve of the fuselage top is clearly visible. The top view of the vehicle is given in Figure D.3. The wing shape from the top is depicted in this view. The internal structural members of the wing are shown in Figure D.4, consisting of the wing ribs and spars. Figure D.5 depicts the internal structural members of the fuselage, consisting solely of frames.

Figure D.1: FEM front view of Aurora

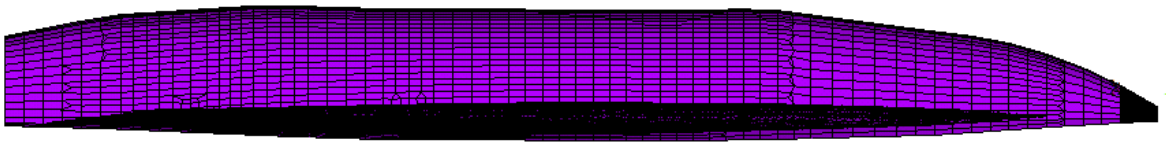

Figure D.2: FEM side view of Aurora

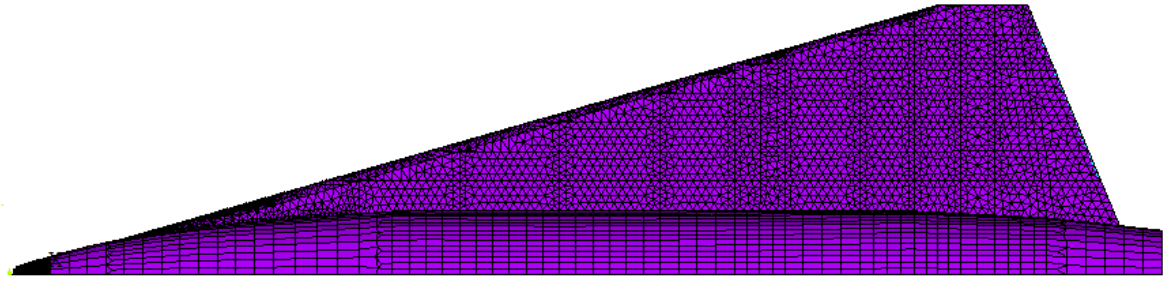

Figure D.3: FEM top view of Aurora

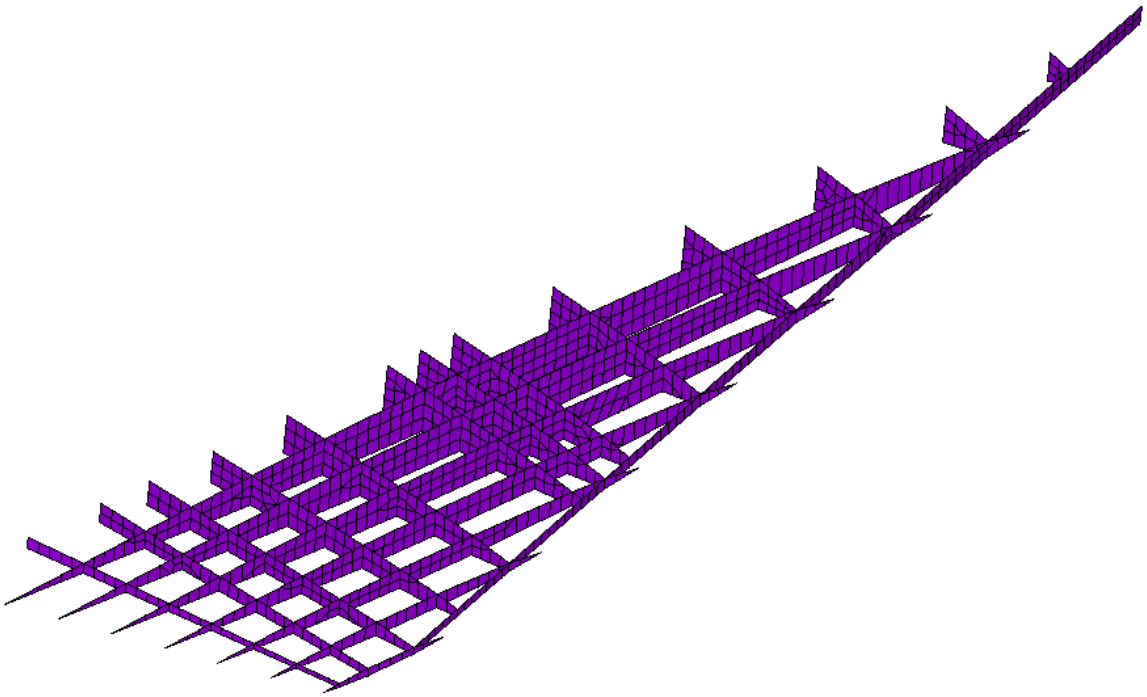

Figure D.4: FEM wing internal structural members of Aurora

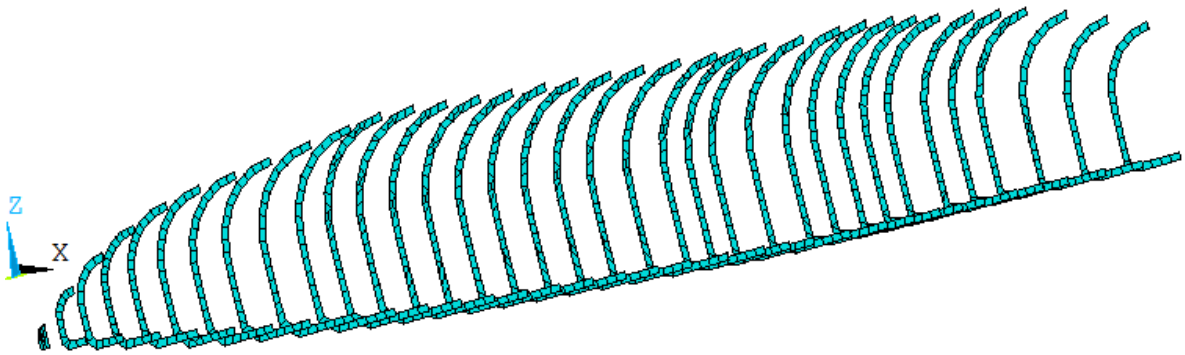

Figure D.5: FEM fuselage internal structural members of Aurora

E

TPS Material Data

In this appendix the specifics are provided of the materials which are used for the different TPS areas of the TPS design [1].

D92 Coating
density: 1553.8 kg/m^3

Table E.1: Conductivity k of D92 Coating

T [K]	0	800	2000
k [W/mK]	$3.1{\cdot}10^{-01}$	$3.1{\cdot}10^{-01}$	$3.1{\cdot}10^{-01}$

Table E.2: Specific heat c_p of D92 Coating

T [K]	0	800	2000
c_p [J/K]	$7.41{\cdot}10^{+02}$	$7.41{\cdot}10^{+02}$	$7.41{\cdot}10^{+02}$

[48]
C9 Coating
density: 2002.3 kg/m^3

Table E.3: Conductivity k of C9 Coating

T [K]	0	533.3	588.9	700	811.1
k [W/mK]	$6.23{\cdot}10^{-02}$	$7.62{\cdot}10^{-02}$	$9.17{\cdot}10^{-02}$	$1.07{\cdot}10^{-01}$	$1.21{\cdot}10^{-01}$
T [K]	922.2	1033.3	1144.4	1255.6	1366.7
k [W/mK]	$1.44{\cdot}10^{-02}$	$1.68{\cdot}10^{-01}$	$1.97{\cdot}10^{-01}$	$2.34{\cdot}10^{-01}$	$2.73{\cdot}10^{-01}$

Table E.4: Specific heat c_p of C9 Coating

T [K]	0	394.4	533.3	672.2	811.1	950.0	1088.9	1172.2	1366.7
c_p [J/K]	$7.41{\cdot}10^{+02}$	$8.22{\cdot}10^{+02}$	$1.02{\cdot}10^{+03}$	1130.4	1159.7	1126.2	1180.7	1235.1	1285.3

[1] Private communication, Alexander Kopp, DLR, 27/7/2016

TUFI Coating
density: 800.9 kg/m^3

Table E.5: Conductivity k of TUFI Coating

T [K]	0	477.8	588.9	700	922.2
k [W/mK]	$6.73{\cdot}10^{-01}$	$6.14{\cdot}10^{-01}$	$5.85{\cdot}10^{-01}$	$5.74{\cdot}10^{-01}$	$5.85{\cdot}10^{-01}$
T [K]	1033.3	1144.4	1255.6	1366.7	1600
k [W/mK]	$6.06{\cdot}10^{-01}$	$6.36{\cdot}10^{-01}$	$6.73{\cdot}10^{-01}$	$7.17{\cdot}10^{-01}$	$9.10{\cdot}10^{-01}$

Table E.6: Specific heat c_p of TUFI Coating

T [K]	0	477.8	588.9	700	922.2
c_p [J/K]	$9.59{\cdot}10^{+02}$	$9.84{\cdot}10^{+02}$	$1.01{\cdot}10^{+03}$	$1.02{\cdot}10^{+03}$	$1.06{\cdot}10^{+03}$
T [K]	1033.3	1144.4	1255.6	1366.7	1600
c_p [J/K]	$1.08{\cdot}10^{+03}$	$1.11{\cdot}10^{+03}$	$1.13{\cdot}10^{+03}$	$1.26{\cdot}10^{+03}$	$1.22\cdot10^{+03}$

CMC
density: 1900.0 kg/m^3

Table E.7: Conductivity k of CMC

T [K]	0	373.15	673.15	1900
k [W/mK]	9.6	9.2	8.8	7.2

Table E.8: Specific heat c_p of CMC

T [K]	0	373.15	973.15	1900
c_p [J/K]	9.0^{+02}	$9.0{\cdot}10^{+02}$	$1.41{\cdot}10^{+03}$	$1.55{\cdot}10^{+03}$

AB 312
density: 985.135 kg/m^3

Table E.9: Conductivity k of AB 312

T [K]	0	477.8	588.9	700	811.1
k [W/mK]	$6.23{\cdot}10^{-02}$	$7.62{\cdot}10^{-02}$	$9.17{\cdot}10^{-02}$	$1.07{\cdot}10^{-01}$	$1.23{\cdot}10^{-01}$
T [K]	922.2	1033.3	1144.4	1255.6	1366.7
k [W/mK]	$1.44{\cdot}10^{-01}$	$1.68{\cdot}10^{-01}$	$1.97{\cdot}10^{-01}$	$2.34{\cdot}10^{-01}$	$2.73{\cdot}10^{-01}$

Table E.10: Specific heat c_p of AB 312

T [K]	0	533.3	588.9	644.5	811.1	922.2	1033.3	1144.4	1255.6	1366.7
c_p [J/K]	845.73	895.98	933.66	962.96	1021.58	1050.89	1071.82	1092.75	1113.69	1130.44

FRSI
density: 96.1108 kg/m^3

Table E.11: Conductivity k of FRSI

T [K]	0	255.6	311.1	366.7	422.2
k [W/mK]	$1.77{\cdot}10^{-02}$	$3.43{\cdot}10^{-02}$	$4.12{\cdot}10^{-02}$	$4.76{\cdot}10^{-02}$	$5.57{\cdot}10^{-02}$
T [K]	477.8	588.9	700	1366.7	
k [W/mK]	$6.40{\cdot}10^{-02}$	$8.22{\cdot}10^{-02}$	$1.05{\cdot}10^{-01}$	$1.34{\cdot}10^{-01}$	

Table E.12: Specific heat c_p of FRSI

T [K]	0	255.6	366.7	477.8	588.9	700	811.1
c_p [J/K]	$1.26{\cdot}10^{+03}$	1.31^{+03}	1.34^{+03}	1.40^{+03}	1.44^{+03}	1.51^{+03}	1.59^{+03}

AFRSI
density: 96.1108 kg/m^3

Table E.13: Conductivity k of AFRSI

T [K]	0	394.4	533.3	672.2	811.1	950	1088.9	1227.8
k [W/mK]	$6.92{\cdot}10^{-03}$	$1.21{\cdot}10^{-02}$	$1.73{\cdot}10^{-02}$	$2.60{\cdot}10^{-02}$	$3.63{\cdot}10^{-02}$	$5.19{\cdot}10^{-02}$	$6.92{\cdot}10^{-02}$	$9.35{\cdot}10^{-02}$

Table E.14: Specific heat c_p of AFRSI

T [K]	0	394.4	533.3	672.2	811.1	950	1088.9	1227.8	1366.7
c_p [J/K]	741	888	1020	1130	1159.7	1126.2	1180.7	1235.1	1285.3

Q-fiber Felt Insulation
density: 96.1108 kg/m^3

Table E.15: Conductivity k of Q-fiber felt insulation

T [K]	0	311.1	422.2	533.3	644.4
k [W/mK]	$8.972{\cdot}10^{-03}$	$1.14{\cdot}10^{-02}$	$1.64{\cdot}10^{-02}$	$2.29{\cdot}10^{-02}$	$3.13{\cdot}10^{-02}$
T [K]	755.6	894.4	977.8	1088.9	1455.6
k [W/mK]	$4.42{\cdot}10^{-02}$	$5.96{\cdot}10^{-02}$	$7.16{\cdot}10^{-02}$	$9.22{\cdot}10^{-02}$	$1.31{\cdot}10^{-01}$

Table E.16: Specific heat c_p of Q-fiber felt insulation

T [K]	0	255.6	394.4	533.3	672.2
c_p [J/K]	$4.40{\cdot}10^{+02}$	$6.28{\cdot}10^{+02}$	$8.79{\cdot}10^{+02}$	$1.06{\cdot}10^{+03}$	$1.15{\cdot}10^{+03}$
T [K]	811.1	950	1088.9	1200	1455.6
c_p [J/K]	$1.21{\cdot}10^{+03}$	$1.24{\cdot}10^{+03}$	$1.26{\cdot}10^{+03}$	$1.26{\cdot}10^{+03}$	$1.27{\cdot}10^{+03}$

AETB-8
density: 128.15 kg/m^3

Table E.17: Conductivity k of AETB-8

T [K]	0	672.2	811.1	950	1088.9
k [W/mK]	$2.60{\cdot}10^{-02}$	$3.81{\cdot}10^{-02}$	$5.36{\cdot}10^{-02}$	$7.10{\cdot}10^{-02}$	$9.35{\cdot}10^{-02}$
T [K]	1277.8	1366.7	1505.6	1644.4	1783.3
k [W/mK]	$1.31{\cdot}10^{-01}$	$1.40{\cdot}10^{-01}$	$1.66{\cdot}10^{-01}$	$1.91{\cdot}10^{-01}$	$1.98{\cdot}10^{-01}$

Table E.18: Specific heat c_p of AETB-8

T [K]	0	394.4	533.3	672.2	811.1
c_p [J/K]	$6.28{\cdot}10^{+02}$	$8.79{\cdot}10^{+02}$	$1.06{\cdot}10^{+03}$	$1.15{\cdot}10^{+03}$	$1.21{\cdot}10^{+03}$
T [K]	950	1088.9	1227.8	1783.3	
c_p [J/K]	$1.24{\cdot}10^{+03}$	$1.26{\cdot}10^{+03}$	$1.27{\cdot}10^{+03}$	$1.27{\cdot}10^{+03}$	

ZIRCAR Alumina
density: 35 kg/m^3

Table E.19: Conductivity k of ZIRCAR Alumina

T [K]	0	588	813.2	1800
k [W/mK]	$7.00{\cdot}10^{-02}$	$7.00{\cdot}10^{-02}$	$9.00{\cdot}10^{-02}$	$9.00{\cdot}10^{-02}$

Table E.20: Specific heat c_p of ZIRCAR Alumina

T [K]	0	500	1800
c_p [J/K]	$1.05{\cdot}10^{+03}$	$1.05{\cdot}10^{+03}$	$1.05{\cdot}10^{+03}$

RTV Adhesive
density: 1409.6 kg/m^3

Table E.21: Conductivity k of RTV adhesive

T [K]	0	200	255.6	366.7
k [W/mK]	$4.03{\cdot}10^{-01}$	,$4.32{\cdot}10^{-01}$	,$4.24{\cdot}10^{-01}$	$3.46{\cdot}10^{-01}$
T [K]	477.8	533.3	1000	1600
k [W/mK]	$2.82{\cdot}10^{-01}$	$2.53{\cdot}10^{-01}$	,$2.00{\cdot}10^{-01}$	$1.80{\cdot}10^{-01}$

Table E.22: Specific heat c_p of RTV adhesive

T [K]	0	200	227.8	255.6	311.1
c_p [J/K]	$1.14{\cdot}10^{+03}$	$1.13{\cdot}10^{+03}$	$1.09{\cdot}10^{+03}$	$1.11{\cdot}10^{+03}$	$1.19{\cdot}10^{+03}$
T [K]	366.7	477.8	555.6	1000	1800
c_p [J/K]	$1.26{\cdot}10^{+03}$	$1.42{\cdot}10^{+03}$	$1.42{\cdot}10^{+03}$	$1.43{\cdot}10^{+03}$	$1.43{\cdot}10^{+03}$

Nomex Felt
density: 196.5 kg/m^3

Table E.23: Conductivity k of Nomex felt

T [K]	0	477.8	588.9	1372.2	1800
k [W/mK]	$3.27{\cdot}10^{-2}$	$4.64{\cdot}10^{-02}$	$6.60{\cdot}10^{-02}$	$1.32{\cdot}10^{-01}$	$1.05{\cdot}10^{-01}$

Table E.24: Specific heat c_p of Nomex felt

T [K]	0	1800
c_p [J/K]	1214.2	1214.2

Aluminum
density: 2803.2 kg/m^3

Table E.25: Conductivity k of aluminum

T [K]	0	144.4	255.6	366.7	422.2	477.8	588.9
k [W/mK]	105.9	120.5	145.4	164.4	171.4	177.4	180.9

Table E.26: Specific heat c_p of aluminum

T [K]	0	33.3	88.9	144.4	255.6	366.7	422.2	477.8	588.9
c_p [J/K]	343.3	368.4	741.1	615.5	816.4	904.3	937.8	975.5	1046.7

F

Sensitivity Analysis

In the sensitivity analysis different configurations of the thicknesses of the TPS areas were tested. In this appendix all variation outcomes are displayed. In table F.1 the resulting maximum temperatures of the TPS and structure of all TPS areas are given, when the insulation thicknesses of the AETB TUFI and CMC areas are varied. In Table F.2 the same is done, only in these variations the insulation thicknesses of all TPS areas are increased individually by the percentage indicated in the table.

Table F.1: Results insulation thickness variations of AETB TUFI and CMC

	Insulation thickness AETB TUFI and CMC [cm]	FRSI	AFRSI	TABI	AETB TUFI	CMC
Max TPS temperature [K]	5	640.2	1311.2	1344.1	1371.5	1439.8
	10	639.3	1151.0	1207.5	1248.6	1428.8
	15	637.2	1137.0	1201.2	1242.1	1422.9
	20	631.3	1066.8	1192.5	1146.0	1303.8
Max structure temperature [K]	5	300.4	300.5	303.3	314.3	300.7
	10	297.4	297.5	298.5	302.5	297.6
	15	296.2	296.3	296.6	297.9	296.3
	20	295.5	295.5	295.6	295.7	295.6

Table F.2: Results insulation thickness variations for all TPSs simultaneously by different factors

	Insulation thickness increase %	FRSI	AFRSI	TABI	AETB TUFI	CMC
Thickness [cm]	50 50 50	26.83	26.83	17.09	20.00	20.00
Max TPS T [K]	1900 1900	623.6	1065.8	1189.5	1142.9	1301.2
Max structure T [K]		294.8	294.8	294.9	295.2	294.9
Thickness [cm]	100 100 100	35.78	35.78	22.79	20.00	20.00
Max TPS T [K]	1900 1900	612.3	1065.5	1185.8	1140.9	1299.5
Max structure T [K]		294.4	294.5	294.6	295.1	294.5
Thickness [cm]	150 150 150	44.47	44.72	28.49	20.00	20.00
Max TPS T [K]	1900 1900	598.9	1065.1	1181.5	1138.9	1297.7
Max structure T [K]		294.2	294.3	294.4	295.1	294.3
Thickness [cm]	100 100 100	35.78	35.78	22.79	25.00	25.00
Max TPS T [K]	2400 2400	593.5	899.6	1195.7	957.5	1131.6
Max structure T [K]		294.0	294.0	294.1	294.1	294.1
Thickness [cm]	80 100 80	32.20	35.78	20.51	24.00	24.00
Max TPS T [K]	2300 2300	596.3	927.8	1195.8	987.7	1157.8
Max structure T [K]		294.2	294.2	294.3	294.3	294.3
Thickness [cm]	100 100 100	35.78	35.78	22.79	24.00	24.00
Max TPS T [K]	2300 2300	593.5	927.4	1194.2	987.2	1157.4
Max structure T [K]		294.1	294.1	294.2	294.2	294.2